

AD-A243 994



2

RL-TR-91-272
Final Technical Report
October 1991



THE FABRICATION, MICROSTRUCTURAL CHARACTERIZATION, AND INTERNAL PHOTORESPONSE OF PLATINUM SILICIDE/P-TYPE SILICON AND IRIDIUM SILICIDE/P-TYPE SILICON SCHOTTKY BARRIER PHOTODETECTORS FOR INFRARED FOCAL PLANE ARRAYS

Stanford University

Sponsored by
Defense Advanced Research Projects Agency
DARPA Order No. AR20

APPROVED FOR PUBLIC RELEASE; DISTRIBUTION UNLIMITED.

The views and conclusions contained in this document are those of the authors and should not be interpreted as necessarily representing the official policies, either expressed or implied, of the Defense Advanced Research Projects Agency or the U.S. Government.


91-18757

Rome Laboratory
Air Force Systems Command
Griffiss Air Force Base, NY 13441-5700

This report has been reviewed by the Rome Laboratory Public Affairs Office (PA) and is releasable to the National Technical Information Service (NTIS). At NTIS it will be releasable to the general public, including foreign nations.

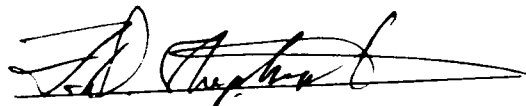
RL-TR-91-272 has been reviewed and is approved for publication.

APPROVED:



PAUL W. PELLEGRINI
Project Engineer

FOR THE COMMANDER:



FREEMAN D. SHEPHERD, Chief
Electronic Device Technology Division
Solid State Sciences Directorate

If your address has changed or if you wish to be removed from the Rome Laboratory mailing list, or if the addressee is no longer employed by your organization, please notify RL(ERED) Hanscom AFB MA 01731-5000. This will assist us in maintaining a current mailing list.

Do not return copies of this report unless contractual obligations or notices on a specific document require that it be returned.

THE FABRICATION, MICROSTRUCTURAL CHARACTERIZATION, AND INTERNAL
PHOTORESPONSE OF PLATINUM SILICIDE/P-TYPE SILICON AND
IRIDIUM SILICIDE/P-TYPE SILICON SCHOTTKY
BARRIER PHOTODETECTORS FOR INFRA-
RED FOCAL PLANE ARRAYS

Douglas Edward Mercer

Contractor: Stanford University
Contract Number: F19628-86-K-0023
Effective Date of Contract: 6 May 86
Contract Expiration Date: 30 Oct 89
Short Title of Work: Platinum Silicide/Silicon Interface
Studies
Period of Work Covered: May 86 - Oct 89

Principal Investigator: Prof. C. Robert Helms
Phone: (415) 723-0406

Project Engineer: Paul W. Pellegrini
Phone: (617) 377-3699

Approved for public release; distribution unlimited.

This research was supported by the Defense Advanced
Research Projects Agency of the Department of Defense
and was monitored by Paul W. Pellegrini RL (ERED),
Hanscom AFB MA 01731-5000, under Contract F19628-
86-K-0023.

Approved for public release; distribution unlimited.
This document contains technical information which is not to be disseminated
outside the Department of Defense or its contractors without the prior
written approval of the appropriate military or civilian agency.
1
H-1

REPORT DOCUMENTATION PAGE

Form Approved
OMB No. 0704-0188

Public reporting burden for the collection of information is estimated to average 1 hour per response, including the time for reviewing instructions, searching existing data sources, gathering and maintaining the data needed, and completing and reviewing the collection of information. Send comments regarding this burden estimate or any other aspect of this collection of information, including suggestions for reducing the burden, to Washington Headquarters Service, Directorate for Information Operations and Reports, 1215 Jefferson Davis Highway, Suite 1204, Arlington, VA 22202-4302, and to the Office of Management and Budget, Paperwork Reduction Project (0704-0188), Washington, DC 20503

1. AGENCY USE ONLY (Leave Blank)		2. REPORT DATE October 1991		3. REPORT TYPE AND DATES COVERED Final May 86 - Oct 89	
4. TITLE AND SUBTITLE THE FABRICATION, MICROSTRUCTURAL CHARACTERIZATION, AND INTERNAL PHOTO RESPONSE OF PLATINUM SILICIDE/P-TYPE SILICON AND IRIIDIUM SILICIDE/P-TYPE SILICON SCHOTTKY BARRIER PHOTODETECTORS FOR INFRARED FOCAL PLANE ARRAYS				5. FUNDING NUMBERS C - F19628-86-K-0023 PE - 61101E PR - E697 TA - AR WU - 20	
6. AUTHOR(S) Douglas Edward Mercer				7. PERFORMING ORGANIZATION NAME(S) AND ADDRESS(ES) Stanford University Stanford Electronics Laboratories Department of Electrical Engineering Stanford CA 94305-4055	
8. PERFORMING ORGANIZATION REPORT NUMBER J-309-1				9. SPONSORING/MONITORING AGENCY NAME(S) AND ADDRESS(ES) Defense Advanced Research Projects Agency 1400 Wilson Blvd Arlington VA 22209 Rome Laboratory (ERED) Hanscom AFB MA 01731-5000	
10. SPONSORING/MONITORING AGENCY REPORT NUMBER RL-TR-91-272				11. SUPPLEMENTARY NOTES Rome Laboratory Project Engineer: Paul W. Pellegrini/ERED/(617) 377-3699	
12a. DISTRIBUTION/AVAILABILITY STATEMENT Approved for public release; distribution unlimited.				12b. DISTRIBUTION CODE	
13. ABSTRACT (Maximum 200 words) A simple analytical model has been developed which predicts the photo response of platinum silicide (PtSi) Schottky barrier diodes on p-type silicon substrates. The model is dependent upon photon energy and PtSi layer thickness. The essential feature of this theory is its ability to describe the basic physics of the photoresponse process in a simple manner. Additional work has been performed on the variation of PtSi parameters with metal deposition temperature and layer thickness, particularly as it effects the infrared response. While no improvement of the infrared response was noted in these experiments, certain previously reported phenomena were explained.					
14. SUBJECT TERMS Schottky Barriers, Photo Diodes, Platinum Silicide, Micro-structure, Infrared Photo Response				15. NUMBER OF PAGES 176	
				16. PRICE CODE	
17. SECURITY CLASSIFICATION OF REPORT UNCLASSIFIED		18. SECURITY CLASSIFICATION OF THIS PAGE UNCLASSIFIED		19. SECURITY CLASSIFICATION OF ABSTRACT UNCLASSIFIED	
				20. LIMITATION OF ABSTRACT UL	

Abstract

Two-dimensional staring arrays of PtSi/*p*-Si Schottky barrier photodiodes have proven their effectiveness in high-resolution infrared imaging applications over the past decade. The ease with which highly uniform arrays can be fabricated using standard silicon planar processing techniques provides a definite advantage over competing technologies. However, the maximum quantum efficiency which these detectors have achieved is at best a few per cent in the spectral region of interest. This fact has motivated studies of both the fundamental limitations governing Schottky detector performance and the potential for increasing the quantum efficiency through process optimization. In this dissertation, the basic concepts, merits, and problems associated with the use of Schottky photodetectors for infrared imaging are outlined. The mechanisms which determine the photoresponse of an array element are discussed with the aid of a model developed during the course of this work. The model resembles that used to describe thermal diffusion yet incorporates the effects of energy losses due to phonon emission and the energy dependence of both the barrier transmission function and the scattering parameters. The dominant factors limiting the photoresponse are shown to be the short hot carrier lifetime, subthreshold excitations, the low barrier transmission probability, and the incompatibility of the optimum silicide film thicknesses which maximize the optical absorption and the hot carrier transport efficiency. In addition to the theoretical efforts, the results of a detailed analysis of the PtSi/*p*-Si system are presented which demonstrate the impact of substrate surface preparation, annealing sequence, and deposited metal thickness on the silicide film microstructure and the device photoresponse. Finally, the patterning difficulties that have contributed to the limited development of the long wavelength IrSi/*p*-Si detector arrays are revealed to stem from an unexpected reaction between the thin iridium films and the SiO₂ masking layers that are commonly employed when the arrays are annealed during silicide

formation. The magnitude of the problem can be greatly reduced through the selective introduction of platinum into the deposited iridium, a technique which is evaluated in some depth.

Contents

1. Introduction	
1.1. Basics of Photodetection Using Schottky Diodes	
1.2. Modeling the Photoresponse.....	
1.3. Impact of Processing Conditions on PtSi/p-Si Detector Microstructure and Photoresponse	
1.4. Extending the Long Wavelength Response with Iridium.....	
2. The Diffusion Model	
2.1. Arguments Against a Quantum Well Model.....	
2.2. The Diffusion Model.....	
2.2.1. Mathematics of the Diffusion Model.....	
2.2.2. Evaluation of Model Parameters	
2.2.3. Comparison with Previous Models.....	
2.2.4. Determination of Quantum Efficiency	
3. Extensions to the Diffusion Model	
3.1. Incorporation of Energy Dependent Transport Parameters.....	
3.2. Phonon Energy Losses	
3.3. Carrier Multiplication at Higher Photon Energies	
4. Characterization of PtSi/p-Si Schottky Barrier Diodes	
4.1. Experimental Considerations.....	
4.2. Room Temperature Interaction Between Pt and Si	
4.3. Effect of Process Variables on the Microstructure.....	
4.4. Effect of Process Variables on the Photoresponse	
5. Kinetics of the Ir/SiO₂ and Pt-Ir/SiO₂ Systems and Implications for the Patterning of IrSi/p-Si Diode Arrays	

5.1. Characterization of the Ir/SiO₂ System
5.2. The Effect of the Presence of Platinum on the Ir/SiO₂ Reaction.....
6. Conclusions and Suggestions for Further Work.....
6.1. Conclusions of the Present Study
6.2. Specific Contributions of This Work
6.3. Novel Device Concepts.....
 6.3.1. The Active Optical Cavity.....
 6.3.2. The Heterostructure Schottky Diode.....
Appendix A. Radiation Absorption in Schottky Photodiodes

Tables

- Table 2.1. Summary of the experimental data collected by Mooney on the photoyield per absorbed photon of PtSi/p-Si Schottky barrier diodes.
- Table 2.2. Optimum optical cavity and PtSi layer thicknesses and corresponding quantum efficiencies for incident light at various wavelengths.....
- Table A.1. The maximum absorption and corresponding PtSi thickness for each of the curves plotted in Fig. A.2.

Illustrations

- Fig. 1.1. An ideal Schottky barrier diode along with its associated electron energy band diagram.....
- Fig. 1.2. Schottky photodiode featuring an anti-reflection coated substrate and a resonant optical cavity to improve the radiation absorption of the silicide layer.....
- Fig. 2.1. Band diagram for an ideal ultra-thin film Schottky barrier diode.
- Fig. 2.2. HRXTEM micrograph of a 20Å (nominal) PtSi/p-Si Schottky photodiode produced at the Rome Air Development Center.....
- Fig. 2.3. The one-dimensional PtSi/p-Si Schottky barrier diode, shown with the optical cavity structure and an anti-reflection coating to enhance the optical absorption.....
- Fig. 2.4. The "escape cone" for excited holes in k-space.....
- Fig. 2.5. The variation of the yield per absorbed photon with the parameter C/D.
- Fig. 2.6. The optimum fit of the diffusion model to the experimental data of Mooney taken at incident photon energies of (a) 3.07µm and (b) 4.25µm.
- Fig. 2.7. The values of $C\tau_r$ as a function of energy obtained by fitting the diffusion model to Mooney's data, together with an optimized linear fit.
- Fig. 2.8. Fowler plots comparing the results of the diffusion model to Mooney's experimental data for diodes with (a) 10Å, (b) 20Å, (c) 40Å, and (d) 100Å PtSi layers.....
- Fig. 2.9. Comparison of various models shown with the experimental data (designated by triangles) taken at a photon energy of 3.07µm.....

- Fig. 2.10. The photoyield per incident photon for PtSi/p-Si diodes at wavelengths of (a) $3.07\mu\text{m}$, (b) $4.07\mu\text{m}$, and (c) $5.01\mu\text{m}$
- Fig. 3.1. A comparison of the numerical results produced by Eqs. (2.23) (solid line) and (3.4) (dashed line) for a 20\AA PtSi/p-Si diode.
- Fig. 3.2. Quantum mechanical step barrier shown from the hole perspective.
- Fig. 3.3. A comparison of the basic diffusion model (solid line) with the model incorporating both a quantum mechanical barrier transmission function and an inverse squared inelastic scattering length (dashed line) along with Mooney's data for a 20\AA PtSi/p-Si diode.....
- Fig. 3.4. The effect of various levels of optical phonon scattering on the photoyield.
- Fig. 3.5. A comparison of the photoyield predicted by the diffusion model incorporating hot carrier multiplication (solid line) with the data obtained by Mooney (triangles) for (a) 10\AA and (b) 20\AA PtSi/p-Si Schottky photodiodes.
- Fig. 3.6. A comparison of the predictions of the diffusion model incorporating multiplication (dashed line) with those of the basic model of Chapter 2 (solid line) for a 5\AA PtSi/p-Si diode.....
- Fig. 4.1. Auger sputter profiles of two 300\AA platinum films evaporated onto silicon substrates at room temperature.
- Fig. 4.2. TEM micrographs of two 20\AA (nominal) PtSi/n-Si diodes formed via the deposition of platinum onto wafers at (a) a room temperature and (b) 350°C that were cleaned using the RRCA' procedure followed by a dilute HF dip.....
- Fig. 4.3. TEM micrograph of the structure formed when 10\AA platinum was deposited onto a room temperature wafer cleaned using the RRCA' method, which leaves a thin residual oxide layer.

Fig. 4.4.	Auger sputter profiles of two 60Å PtSi films on n-Si formed via platinum evaporation onto (a) an RRCA' cleaned substrate at room temperature and (b) a substrate at 350°C which had received an RRCA' clean followed by a dilute HF dip.	96
Fig. 4.5.	TEM micrograph of a 600Å (nominal) PtSi film grown on an n-type silicon substrate cleaned using the RRCA' method and held at room temperature during the platinum evaporation.....	98
Fig. 4.6.	Auger sputter profiles of two 600Å (nominal) PtSi films grown on n-Si through the evaporation of platinum onto (a) an RRCA' cleaned substrate at at 350°C and (b) a substrate at room temperature which had received an RRCA' clean with a subsequent dilute HF dip.....	100
Fig. 4.7.	Fowler plots of the relative internal voltage photoyield of 80Å PtSi/p-Si Schottky photodiodes which show the effects of variations in substrate temperature during metal deposition for a given substrate cleaning procedure.....	106
Fig. 5.1.	Auger sputter profile of a 60Å platinum film deposited onto a gate oxide layer at 350°C and annealed for one hour.	114
Fig. 5.2.	Auger sputter profiles of 60Å iridium films deposited onto gate oxide layers (a) at room temperature with no subsequent anneal, (b) 500°C with a one hour anneal, and (c) 750°C with a one hour anneal.	115
Fig. 5.3.	Auger sputter profiles of (a) 60Å Ir / 60Å Pt / SiO ₂ and (b) 60Å Pt / 60Å Ir / SiO ₂ structures annealed one hour at 500°C.	120
Fig. 5.4.	Auger sputter profiles of (a) 90Å Ir / 30Å Pt / SiO ₂ and (b) 30Å Pt / 90Å Ir / SiO ₂ structures annealed one hour at 500°C.	123
Fig. 5.5.	Auger sputter profile of a multilayer silicide Schottky diode.	126
Fig. 6.1.	Two alternative designs for a Schottky photodetector utilizing an active optical cavity.	135

- Fig. 6.2. The energy band diagram of the heterostructure Schottky detector.....
- Fig. A.1. The ideal one-dimensional PtSi/p-Si Schottky photodiode both with
and without an anti-reflection coating and a resonant optical cavity.....
- Fig. A.2. A comparison of the predicted optical absorption of back-illuminated
PtSi/p-Si diodes with various combinations of absorption enhancing
design features, plotted as a function of silicide thickness for radiation
incident at a wavelength of $4\mu\text{m}$
- Fig. A.3. A comparison of the predicted absorption curves for two PtSi/p-Si
photodiodes optimized for maximum optical absorption and maximum
quantum efficiency, respectively, at $4\mu\text{m}$

Chapter 1

Introduction

The ability to see in the dark is a faculty long sought after. Not until the discovery of the infrared portion of the radiation spectrum by Herschel in 1800, however, was a physical basis for this capability established. The years following this achievement have seen the development of a wide variety of devices to sense this radiation, including both single element detectors and, more recently, infrared imaging systems as well. Over the past decade, two-dimensional silicide-silicon Schottky barrier infrared staring arrays have emerged as one of the leading technologies available for real time, high resolution imaging in the middle to far infrared spectral regimes.¹⁻¹⁵ While this technology has attained a certain level of maturity, several questions still remain concerning the operation of the individual detector elements, the potential for further enhancements in the photoresponse performance, and the fabrication difficulties encountered when particular silicides are employed. This dissertation details a number of theoretical and experimental analyses of the photodiodes which compose a silicide-silicon Schottky infrared focal plane array. The results of these studies contribute significantly to the understanding of the basic physical mechanisms governing the photoresponse of these devices, the effect of various processing techniques on the detector microstructure and performance, and the material interactions which can interfere with the patterning of silicide arrays. Although the current performance of Schottky focal planes is quite good, the findings presented here suggest that further improvements are indeed possible.

The emission of infrared or thermal radiation characterizes all known objects at finite temperatures.^{16,17,18} The ability to properly sense these emissions allows the detection of objects not only through darkness, but also fog, smoke, the upper atmosphere, walls, human tissue, and other otherwise opaque media. Wavelengths longer than $3\mu\text{m}$ are of particular interest in light of the detailed emission properties of bodies at relatively low temperatures and the transmission of the atmosphere. The blackbody emission profile for objects near ambient temperature peaks at about $10\mu\text{m}$, and the maximum shifts to longer wavelengths as the temperature falls. Moreover, the atmosphere, which exhibits a number of absorption lines in the infrared, is relatively transparent from 3 to $5\mu\text{m}$ and 8 to $14\mu\text{m}$. Most of the recent effort in infrared imaging has been devoted to systems which operate in one or both of these two windows.

While a number of devices which simply determine the presence or absence of infrared radiation were developed soon after its discovery, the first true imaging technology did not appear until much later. The evapograph, whose operation depended on the spatially varying rate of oil evaporation from a blackened membrane illuminated with the desired image, was a fairly crude invention which suffered from low resolution and an extremely long time constant. This design was clearly impractical for most purposes, however, as the only means available for imaging at the time it did enjoy a certain amount of use. The next evolutionary stage involved the combination of a scanned optical system and a fixed detector element, which could be any of several types. The total field of view was divided into a fine grid of subfields, the light from each would be focussed in turn onto the actual detector by the optical system as it swept the image. With high precision mechanical scanning units and tight focussing control, excellent resolution can be obtained using this method. Unfortunately, optimum resolution and noise performance correspond to extremely long scan times, which prevents the use of this technique for real time imaging. In addition, the dependence on carefully controlled moving parts limits the reliability and durability of such a system. Nevertheless, this

technique is still utilized in some space applications and other low shock environments in which long imaging times are available.

Probably the first practical device for long wavelength infrared imaging in real time was the pyroelectric vidicon tube. This device, which resembles a standard television camera tube in many respects, offers moderate resolution and sensitivity without requiring the sensing component to be cooled. The retina in the vidicon tube originally consisted of a single large area pyroelectric capacitor; however, more recent designs incorporate a reticulated array which offers an improvement in the spatial resolution that can be achieved by limiting the thermal spread of the signal. The vidicon is relatively inexpensive, and still sees extensive use in commercial applications.

In contrast to the pyroelectric vidicon, which is often designated a "thermal" detector system, imaging units based on solid-state "photon" detector technologies offer higher resolution and sensitivity at the expense of detector cooling. Scanned linear arrays of compound semiconductor photoconductive and photovoltaic devices have been employed in satellites and strategic systems for several years. The most important compound materials for imaging applications have been InSb, which operates in the 3–5 μ m wavelength window; and Hg_{1-x}Cd_xTe (MCT), which can operate in the longer wavelength window as well given suitable control of the x value governing the width of the semiconducting band gap. The high quantum efficiencies and low time constants associated with these detectors allow fairly low image acquisition times even with the inherent scan time inefficiency; however, the presence of the scanning subsystem still limits the durability of the overall imaging unit.

The drawbacks of scanning systems have fueled a recent trend toward two-dimensional staring arrays. Both monolithic and hybrid arrays have been explored in several materials, the two terms signifying whether the actual detectors are fabricated on the chip containing the readout circuitry or are bonded to a processing chip manufactured separately. In addition to the compound semiconductor devices mentioned above,

extrinsic silicon detectors have been produced in array form for extremely long wavelength applications. Most of these situations arise in space, where the normally prohibitive cooling requirements of extrinsic detectors are less problematic. Terrestrial situations tend to favor the compound materials over extrinsic silicon. However, a number of problems arise in connection with the manufacture and use of compound semiconductor arrays. These materials are typically difficult to process, exhibiting both instability at relatively moderate temperatures and mechanical fragility. Many fabrication steps which can often be taken for granted when dealing with silicon, such as doping, insulator growth or deposition, surface passivation, and metallization, can create substantial problems in these less common material systems. In addition, the uniformity of the individual detector elements across the array is quite poor, especially in the case of MCT. Array noise arising from non-uniformities significantly complicates the image processing requirements for the overall system. These and other shortcomings have seriously limited the development of compound semiconductor staring arrays.

Two-dimensional silicide-silicon Schottky photodiode arrays, originally proposed by Shepherd and Yang in 1973,¹⁹ arose as an alternative to the compound semiconductor arrays. The Schottky focal planes avoid many of the pitfalls that plague competing detector arrays. They are relatively easy to manufacture, since they can take advantage of the extremely mature silicon processing technology. Excellent array uniformity is obtained, which relaxes the associated image processing specifications. Palladium, platinum, and iridium silicide arrays have all been produced, although the relatively high cutoff of palladium (3.6 μm) renders it ineffective in most long wavelength applications. Platinum silicide on *p*-type silicon (PtSi/*p*-Si) Schottky diodes can detect radiation to beyond 5 μm , while IrSi/*p*-Si diodes reach out to 10 μm . The last ten years have seen the evolution of silicide array sizes from a relatively crude level of 25x50 pixel elements to some as large as 512x512¹⁵ or 480x600²⁰, by far the largest focal planes available in any material. The main shortcoming which limits the performance of these devices is their

relatively low quantum efficiency. A PtSi/*p*-Si detector operating at 4 μ m typically exhibits a quantum efficiency of only about 1%, in comparison to a value of 70% available from an MCT device. In many instances, the superior response uniformity across the entire focal plane compensates for the decidedly inferior efficiency. However, the low efficiency does place a lower limit on the image acquisition time, restricting the use of these arrays in high speed situations. In addition, the sensitivity to thermal noise necessitates the cooling of IrSi arrays to approximately 40K, far below the liquid nitrogen operating temperature of MCT arrays at 8–10 μ m. Yet, despite these obstacles, silicide Schottky focal planes currently compete favorably with other technologies. Nevertheless, the improvement of the quantum efficiency remains a top priority of research efforts in this field and has provided the impetus for this work. For further information on the various types of infrared detectors mentioned above along with many others, references 16–18 listed at the end of this chapter together provide an excellent summary of past and current technology.

1.1. Basics of Photodetection Using Schottky Diodes

In order to improve the performance of silicide-silicon Schottky photodiodes, it is first necessary to understand how they operate. An idealized picture of a typical Schottky infrared photodiode is shown in Fig. 1.1 along with the electron energy band diagram which characterizes the structure at equilibrium when no external fields are applied. Detailed derivations of the Schottky barrier band diagram are given in many texts,²¹ so no such calculation will be repeated here. The device is extremely simple, consisting only of a layer of metal or metal silicide in intimate contact with a semiconductor substrate. Silicide layers are usually formed by depositing the metallic component onto a silicon wafer and annealing the devices at temperatures ranging from 300 to 600°C for times on the order of an hour. The low barriers needed for long wavelength detectors are produced only when *p*-type silicon is employed, which implies that the photocurrent will be carried primarily by vacant valence band electron states or “holes.” Since the diodes are normally

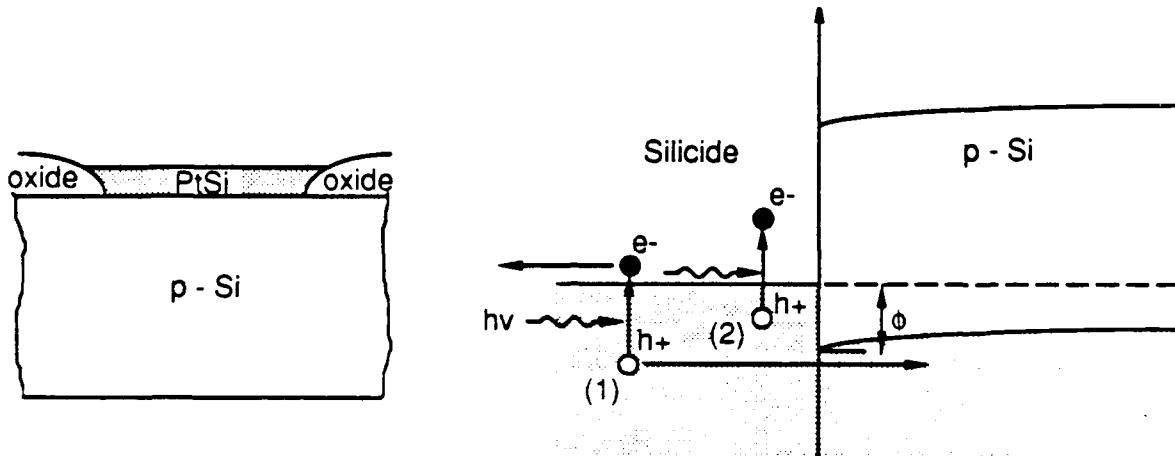


Fig. 1.1. An ideal Schottky barrier diode along with its associated electron energy band diagram. *P*-type silicon wafers are always employed for infrared photodiodes. The diagrams are not drawn to scale.

illuminated from the back, i.e. substrate, side to take advantage of the refractive index matching properties of the silicon and improve the overall optical absorption of the detector, lightly doped silicon wafers on the order of 10^{15} cm^{-3} boron concentration are normally employed to prevent the excessive free carrier absorption in the silicon which would otherwise ensue. With this doping level and the low barriers involved, the depletion region in the silicon adjacent to the material interface inside which any significant band bending occurs is approximately 4500\AA in width. The barrier lowering due to the image force is less than 10mV and can generally be neglected.

The photodetection process in a Schottky diode can be broken into three separate parts similar to those employed in the three step model originally developed by Spicer to describe external photoemission from material surfaces in vacuum.²² In the first step, radiation incident on the detector is absorbed in the silicide layer, giving rise to electron-

hole pair excitations. In the second phase, hot carriers are transported from the point of their creation to the Schottky potential barrier formed at the interface between the silicide and the substrate. Finally, when *p*-type silicon serves as the substrate, hot holes which reach the barrier with a total energy of excitation that exceeds the barrier height (hole energy increases in the downward direction in Fig. 1.1) have a finite probability to be transmitted over the barrier into the semiconductor, where they can be collected and read out as detected events. The detector cutoff wavelength or, equivalently, the cutoff energy is thus determined by the height of the Schottky barrier. Estimates of the PtSi/*p*-Si barrier height range from 0.19 to 0.24 eV depending on the particular measurement technique utilized and the diode fabrication environment. Electrical measurements, i.e. I-V and C-V, yield systematically lower barrier heights when compared with internal photoemission; the discrepancy has been attributed to the influence of phonon scattering on the photoemission results.²³ A typical device will yield an optical barrier height of about 0.22 eV, corresponding to a detector cutoff wavelength of 5.6 μ m. Similar measurements on IrSi/*p*-Si diodes suggest barrier heights anywhere from 0.12 to 0.15 eV, and cutoff wavelengths out to 10 μ m have been obtained.²⁴ It has been demonstrated in the case of PtSi that the barrier can be further reduced through the implantation of dopant atoms into the substrate immediately adjacent to the silicide-silicon interface.²⁵ The pileup of ionized acceptors creates an additional electric field at the interface, which when superimposed on that which would exist without the implant produces an effective lowering of the Schottky barrier. PtSi/*p*-Si barriers as low as 6.5 μ m have been measured in this manner.¹⁰ This particular barrier modification technique will not be examined further in the present study.

Although the photodetection process in Schottky barrier diodes seems reasonably straightforward, there are a number of obstacles which limit the accomplishment of each of the subprocesses mentioned above. The optical absorption phase exhibits two major shortcomings. First of all, the silicide film thickness needed to maximize the overall quantum efficiency, i.e. the fraction of detected holes per photon incident on the device,

always turns out to be much thinner than the thickness that would maximize the radiation absorption when hot carrier transport issues are considered. At most 20% of the incident photons are ever absorbed within an PtSi film of optimum width at a wavelength of $4\mu\text{m}$. The vast majority of photons available are simply lost for want of absorbing material. Moreover, of those photons that are actually absorbed, many produce excitations of insufficient energy to ever surmount the Schottky barrier. In Fig. 1.1, two distinct absorption events labeled (1) and (2) were illustrated. Since allowed hole states exist in the silicide at energies between the Fermi level and the barrier maximum as well as in excess of the barrier maximum, photon absorption by electrons initially residing in these states, such as the event labeled (2), will be just as probable as the more desirable process (1) if the density of states near the Fermi level is fairly constant. For incident photon energies which approach the detector cutoff, these subthreshold excitations will account for most of the absorption events. In a PtSi/*p*-Si diode operating at $4\mu\text{m}$, for example, approximately 2/3 of the excitations will occur below threshold. Because quantum mechanical tunnelling is essentially absent due to the low and extremely wide barrier produced with the lightly doped substrates that are used, holes excited to energies below the height of the Schottky barrier have virtually no chance of ever escaping the silicide film and, thus, are wasted. Between the suboptimal absorption geometry and the subthreshold excitation inefficiency, the number of potentially detectable photons is over an order of magnitude lower than the total number available from the scene of interest.

If a hole is actually created at an energy sufficient to permit escape, further difficulties arise in the transport and transmission stages. In a normal metal or metallic film such as a silicide, the lifetime of an excited carrier is extremely short due primarily to the high probability of suffering a collision with any one of the high concentration of cold carriers, an event which robs the hot carrier of a significant fraction of its energy. Sub-picosecond lifetimes are the main reason that the concept of an electron-hole pair excitation is not generally associated with a metal. Therefore, once excited, a hot hole has little time

to reach the barrier before it is thermalized to an energy inadequate for emission. Furthermore, it turns out that a potentially detectable hole incident on the barrier from the silicide has a fairly small chance of transmission, particularly at energies near cutoff. If conservation of the parallel component of hole momentum is assumed, then a transmission probability below 1% is calculated for photon energies up to 1 eV as a result of the poor match which exists between the perpendicular momentum components in the two materials.²⁶ Relaxation of the conservation condition in accordance with the assumption of at least partially diffusive rather than fully specular scattering at the interface will increase estimates of the transmission probability; however, relatively small values are still obtained, especially at the energies of most interest. Thus, not only does a photoexcited hole have a mediocre chance of reaching the Schottky barrier itself from any significant distance, but its chances of escape once there are poor. When coupled with the absorption characteristics of the device, this suggests why the quantum efficiency is as low as it is in Schottky detectors.

Although the preceding discussion paints a fairly bleak picture of the Schottky photodiode, several techniques exist for minimizing the impact of the various obstacles that have been pointed out. A number of enhancements are commonly added to the basic diode structure in order to improve the radiation absorption in the silicide layer, and Fig. 1.2 displays a detector design which incorporates these features. It was mentioned earlier that the diodes are generally illuminated from the back side of the detector through the substrate rather than from the silicide side. The silicon wafer acts as a refractive index matching layer, which reduces the amount of reflection from the metallic silicide film. In addition, as the figure indicates, an anti-reflection coating is often added to the polished back surface of the wafer to further boost the radiation coupling. Furthermore, a resonant dielectric cavity can be built on top of the silicide layer which essentially traps incident radiation in the form of a standing wave. The optical cavity concept originated at Hewlett-Packard,²⁷ but was first used extensively by RCA.²⁸ A dielectric material, usually SiO_2

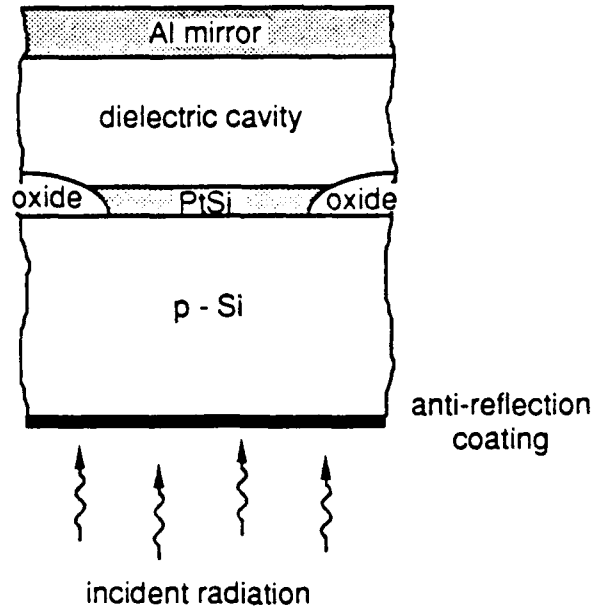


Fig. 1.2. Schottky photodiode featuring an anti-reflection coated substrate and a resonant optical cavity to improve the radiation absorption of the silicide layer.

or SiO₂, is deposited on top of the silicide at a relatively low temperature and capped with an aluminum mirror. The dielectric thickness is selected to peak the silicide absorption at a particular wavelength, and the cavity is said to be “tuned” to that wavelength. The theory and operation of the optical cavity are discussed in more detail in Appendix A. When all of the enhancements that have been described are employed, the absorption of the silicide layer can increase by a factor of two to three over its value when a bare, front illuminated diode is used.

Like the absorption difficulties, the transport and transmission problems can be countered to a certain degree. Since the barrier transmission appears to be quite small, it would seem advantageous to allow the hot holes numerous attempts to escape. In view of the exceptionally short excitation lifetime, however, the hot holes would have to be confined to the area immediately adjacent to the silicide-silicon interface in order for this to

be possible. The confinement can be easily accomplished through the use of extremely thin silicide layers, so that no point in the film is ever very far from the Schottky barrier. The increase in Schottky diode quantum efficiency with decreasing metal layer thickness was first observed experimentally in the late 1960's,²⁷ and current focal plane arrays typically employ diodes with silicide layers as thin as 20 to 40Å. Films of these dimensions can provide a dramatic, i.e. over an order of magnitude, increase in the response level over those even just a few hundred angstroms thick despite the relative inefficiency in the radiation absorption process that was mentioned earlier. The ability to accurately predict the enhanced performance, however, has proven to be somewhat elusive; a fact which indicates that many of the models that have been developed do not take into account all of the relevant physics of the problem. The rectification of this situation was one of the primary goals of this work. In order to address the problem properly, however, it is first necessary to summarize the various modeling efforts that have been presented over time.

1.2. Modeling the Photoresponse

The first attempts to explain the variation of the internal photoresponse of a Schottky diode with incident photon energy involved the application of a model developed by Fowler in 1930 to describe external photoemission of electrons into vacuum from clean metal surfaces.²⁹ The surface potential employed by Fowler was simply replaced with the apparent Schottky barrier height. The Fowler model was founded on three basic postulates. In part because the temperature variation of the response was a concern, the Fermi-Dirac statistical nature of the free electron distribution was explicitly incorporated. Secondly, it was assumed that the absorption of incident photons by electrons adjacent to the metal surface augmented the energy associated with the component of momentum normal to the surface, creating a uniform distortion of the distribution. Finally, those carriers whose "energy perpendicular to the surface" exceeded the surface potential were

assumed to be emitted with a probability of one, an essentially classical description of barrier transmission. While the Fowler model worked very well, the assumption of highly anisotropic optical absorption seemed unfounded. It was later demonstrated that not only this assumption but also the explicit consideration of Fermi-Dirac statistics could be relaxed if the temperature variation was of no concern. Stuart and Wooten showed that the same functional form resulted if the density of states near the Fermi level in the metal could be presumed constant and if it was assumed that the absorption of incident photons simply induced a uniform upward shift in the carrier distribution within a photon energy of the Fermi level by an amount equal to the photon energy.³⁰ As in the Fowler analysis, those electrons in the "spherical shell of excitation" whose momentum normal to the barrier reflected a kinetic energy that exceeded the barrier height were assumed to escape into the semiconductor. In the presence of isotropic absorption, the emitting states lie in a small sector of the shell of excited states, the so-called "escape cap" or "escape cone" mentioned in later summaries of the theory.

The work of Cohen et. al. in the late 1960's represented the first application of the modified Fowler model to the analysis of Schottky diode photoresponse data.²⁷ Several other significant theoretical contributions appeared at about the same time. Kane in 1966 employed a clever recursive solution method to study the influence of photoelectron-phonon scattering on the photoyield by tracing various possible kinetic histories of each photoexcited carrier.³¹ This work indicated that the ability of isotropic phonon scattering to redirect the momentum of hot carriers headed away from the barrier into the escape cone could have a decidedly positive impact on the response level observed. More important advances followed in 1971, when two different models were published in order to explain the apparent rise in the quantum efficiency with decreasing metal film thickness that had been observed experimentally in the Cohen study. Dalal basically just extended the Kane analysis to allow for the presence of boundary scattering in very thin films.³² The Vickers model was also of the kinetic type; however, the method and some of the assumptions

used were quite different from those utilized in the Kane formulation.³³ Both models predicted dramatic increases in the efficiency for thin metal layers, although neither was intended to be applied for thickness approaching zero. The Vickers model, in particular, predicts an infinite response in this limit. However, until interest arose in the exploitation of ultra-thin Schottky diodes for infrared focal plane arrays, the Dalal and Vickers models proved entirely adequate to explain Schottky photoresponse data.

After the work of Vickers and Dalal, little theoretical activity of significance was reported until 1985, when Mooney and Silverman created an extended version of the Vickers derivation to describe the photoyield of thin film PtSi/p-Si diodes.^{23,34} The earlier models were not particularly effective at explaining the observed diode response when PtSi films less than 50Å thick were employed. Since this thickness range seemed to produce the optimum level of response, a more accurate model was called for. Two major changes were made in the framework established by Vickers. The implicit assumption of a small capture ratio was eliminated. In addition, energy losses resulting from the emission of optical phonons by hot carriers were included. Several less critical aspects were modified as well, such as the incorporation of a scattering length for lossless impurity and defect collisions and the ability to insert a constant transmission factor other than one; however, these elements had little impact on the results. The study showed that when the possibility of significant capture ratios are taken into account, the photoyield approaches the fraction of excited holes whose energies exceed the barrier height in the zero thickness limit, an eminently sensible result. The addition of phonon losses, moreover, brought the curvature of the predicted yield more in line with the experimental data, and also provided an explanation of the systematically higher apparent Schottky barrier height values extracted from internal photoresponse data in comparison to those obtained from current-voltage and capacitance voltage measurements as mentioned previously. When the various parameters were fully optimized, the Mooney model did an exceptional job of describing much of the observed photoyield data. Nevertheless, this

method had several shortcomings. The formulation employed numerous adjustable parameters, and was sufficiently complex that a computer solution was required. The quantity of adjustable values was such that the physical content of the data fit was somewhat questionable. Moreover, the relative importance of the various physical mechanisms which together determine the yield was not terribly obvious given the somewhat obscure numerical form of the result. In addition, some of the more "anomalous" response measurements that had been reported in connection with PtSi/p-Si diodes remained unexplained. In particular, the lack of a noticeable drop in the observed yield in certain detectors at higher photon energies as the silicide film thickness fell below the predicted optimum value was still a mystery.³⁵ These factors together provided motivation for the development of a relatively simple analytical model of the performance of ultra-thin film Schottky photodiodes that could provide a good description of the experimental data while elucidating the key mechanisms governing the photoyield. Such an effort constituted a significant fraction of the research activity described here, and its derivation forms the subject of Chapters 2 and 3.

1.3. Impact of Processing Conditions on PtSi/p-Si Detector Microstructure and Photoresponse

The modelling work clearly identifies the device parameters which limit Schottky photodiode performance. However, the task of subsequently effecting a positive impact on those variables that are implicated is definitely non-trivial. Aside from changes in the design and operating conditions of the diodes, the only avenue available for modifying these parameters is the alteration of the processing methods used in fabrication. Device parameters can generally be related either quantitatively or qualitatively to observable chemical and structural characteristics, which are often determined in part by the various fabrication procedures experienced. The strong influence of different silicon wafer cleaning techniques and annealing treatments on the microstructure of thick, i.e. 1000-

3000Å, PtSi films has been reported in the open literature.^{36,37} Despite this fact, no detailed study of the relationship between the processing methods employed and the resulting microstructure and infrared photoresponse of thin film PtSi/p-Si diodes has ever been published. In an effort to remedy this situation, Chapter 4 describes the results of an analysis of this type. The effects of assorted wafer cleaning procedures, different wafer temperatures during platinum deposition, and varying amounts of platinum are discussed along with the implications for array production. The results show that significant variations in both microstructure and response can be induced, although the changes observed were not generally preferable.

1.4. Extending the Long Wavelength Response with Iridium

As mentioned earlier, the replacement of PtSi by IrSi in a silicide-silicon Schottky photodiode leads to a lower Schottky barrier height and, therefore, an extension of the long wavelength photoresponse. Unfortunately, this highly advantageous development is accompanied by a few rather onerous complications. One of these problems stems from the presence of the low barrier itself. In any photodiode at a finite temperature, the photoresponse process operates in parallel with thermal emission derived from the statistical distribution of electrons and holes. In a Schottky diode, an exponentially decreasing concentration of holes always exists in the metallic layer at energies exceeding the barrier height due to thermal excitation. This population generates a dark current proportional to $\exp(-\phi/kT)$ (ϕ represents the Schottky barrier height)²¹ that flows even when photoexcited carriers are absent and creates a background which must be subtracted from the total signal level. In a low barrier device, the barrier maximum is close enough to the Fermi level that the thermal population is quite substantial at ambient temperature. Cooling the detector reduces the concentration of thermal carriers at each energy exceeding the Fermi level, which reduces the dark current to a level at which its contribution to the total output is easily subtracted. A PtSi/p-Si diode exhibits an acceptable dark current

when cooled to about 80K, a condition which can easily be produced with the compact refrigeration units that are currently available.¹¹ However, to achieve the same dark current in an IrSi/*p*-Si diode with its much lower barrier, the temperature must be lowered to approximately 40K, an operating point beyond the capabilities of any present cooler that could be considered to be compact. This limits the types of systems into which IrSi arrays can now be integrated. Any material that produced a Schottky barrier of a similar magnitude would be expected to suffer from this problem.

In addition to the sort of fundamental obstacle just discussed, IrSi arrays have been beset by other difficulties peculiar to the presence of iridium itself. Contaminants both in the deposited metal and on the surface of the silicon substrate prior to deposition affect the performance and reproducibility of the resulting photodiodes to a much greater extent when iridium is substituted for platinum as a consequence of differences in the growth kinetics between PtSi and IrSi.^{24,38} Silicide formation will be discussed in more detail in Chapters 4 and 5. Iridium lithography has also caused a certain amount of grief. In contrast, the ease with which platinum can be patterned has always been one of its more pleasant features. Platinum readily dissolves in hot aqua regia (HCl : HNO₃), yet the solution leaves PtSi essentially unaffected. Moreover, platinum does not react with SiO₂ at temperatures anywhere near as low as those employed in diode fabrication. These two points allow PtSi arrays to be delineated using an oxide masking layer that is compatible with vacuum annealing. The unreacted platinum lying atop the oxide can later be removed in an aqua regia bath without ruining the diodes. Unfortunately, iridium patterning cannot be accomplished quite this easily. Part of the problem derives from the fact that bulk iridium is insoluble in aqua regia; however, even dry etching techniques have trouble removing the extraneous metal.³⁹ The potential for damaging the extremely thin silicide films when dry methods are utilized only exacerbates the dilemma. Given this situation, Chapter 5 describes a spectroscopic analysis of the iridium-SiO₂ system that provides some indication of the causes behind the patterning difficulties that have been experienced.

In addition, evidence of a possible solution to the problem involving the selective introduction of platinum into the iridium film will be presented. This discovery could find immediate application in the fabrication of IrSi/p-Si focal plane arrays. Chapter 6 contains some of the conclusions of this work, and discusses some ideas generated during the course of the study for some novel detector structures and future research endeavors.

References for Chapter 1

1. B. Capone, L. Skolnik, R. Taylor, F. Shepherd, S. Roosild, W. Ewing, W. Kosonocky, E. Kohn, "Evaluation of a Schottky Infrared Charge-Coupled Device (IRCCD) Staring Mosaic Focal Plane," *Opt. Eng.* 18, 535 (1979).
2. R. Taylor, L. Skolnik, B. Capone, W. Ewing, F. Shepherd, S. Roosild, B. Cochrun, M. Cantella, J. Klein, W. Kosonocky, "Improved Platinum Silicide IRCCD Focal Plane," *Proc. SPIE* 217, 103 (1980).
3. M. Kimata, M. Denda, T. Fukumoto, N. Tsubouchi, S. Uematsu, H. Shibata, T. Higuchi, T. Saheki, R. Tsunoda, T. Kanno, "Platinum Silicide Schottky-Barrier IR-CCD Image Sensors," *Jap. J. Appl. Phys.* 21, supplement 21-1, 231 (1981).
4. B.R. Capone, R.W. Taylor, W.F. Kosonocky, "Design and Characterization of a Schottky Infrared Charge Coupled Device (IRCCD) Focal Plane Array," *Opt. Eng.* 21, 945 (1982).
5. W.R. Kosonocky, H. Elabd, H.G. Erhardt, F.V. Shallcross, G.M. Meray, T.S. Villani, J.V. Groppe, R. Miller, V.L. Frantz, M.J. Cantella, J. Klein, N. Roberts, "Design and Performance of 64x128 Element PtSi Schottky-Barrier Infrared Charge-Coupled Device (IRCCD) Focal Plane Array," *Proc. SPIE* 344, 66 (1982).
6. K. Tanikawa, Y. Ito, A. Shimohashi, "A PtSi Schottky-Barrier Area Imager with Meander-Channel CCD Readout Registers," *IEEE Electron Device Lett.* EDL-4, 66 (1983).
7. W.S. Ewing, F.D. Shepherd, R.W. Capps, E.L. Dereniak, "Applications of an Infrared Charge-Coupled Device Schottky Diode Array in Astronomical Instrumentation," *Opt. Eng.* 22, 334 (1983).
8. W.R. Kosonocky, H. Elabd, "Schottky-Barrier Infrared Charge-Coupled Device Focal Plane Arrays," *Proc. SPIE* 443, 167 (1983).
9. M. Kimata, M. Denda, S. Iwade, N. Yutani, N. Tsubouchi, "A Wide Spectral Band Photodetector with PtSi/p-Si Schottky-Barrier," *Int. J. Infr. Mil. Wav.* 9, 1031 (1985).

10. W.R. Kosonocky, F.V. Shallcross, T.S. Villani, J.V. Groppe, "160x244 Element PtSi Schottky-Barrier IR-CCD Image Sensor," *IEEE Trans. Electron Dev.* ED-32, 1564 (1985).
11. M. Kimata, M. Denda, N. Yutani, S. Iwade, N. Tsubouchi, M. Daido, H. Furukawa, R. Tsunoda, T. Kanno, "256x256 Element Platinum Silicide Schottky-Barrier Infrared Charge-Coupled Device Image Sensor," *Opt. Eng.* 26, 209 (1987).
12. N. Yutani, M. Kimata, M. Denda, S. Iwade, N. Tsubouchi, "IrSi Schottky-Barrier Infrared Image Sensor," *IEDM Tech. Dig.* 124 (1987).
13. R.H. Dyck, J.S. Kim, Y. Abedini, H. Elabd, W.G. Petro, K.K. Shah, H.A. Lehan, J. Chiu, J. Wong, H.L. Balopole, J.C. Holland, T.A. Pletcher, "A 244x190 Element PtSi Imager Built with Mature CCD Production Technology," *Proc. SPIE* 924 (1988).
14. F.D. Shepherd, "Silicide Infrared Staring Sensors," *Proc. SPIE* 930, 1 (1988).
15. M. Kimata, M. Denda, N. Yutani, S. Iwade, N. Tsubouchi, "High Density Schottky-Barrier Infrared Image Sensor," *Proc. SPIE* 930, 11 (1988).
16. P.N.J. Dennis, Photodetectors (Plenum, New York, 1986).
17. E.L. Dereniak, D.G. Crowe, Optical Radiation Detectors (Wiley, New York, 1984).
18. R.W. Boyd, Radiometry and the Detection of Optical Radiation (Wiley, New York, 1983).
19. F.D. Shepherd, A.C. Yang, "Silicon Schottky Retinas for Infrared Imaging," *IEDM Tech. Dig.* 310 (1973).
20. Hughes Microelectronic Center, private communication.
21. e.g. S.M. Sze, Physics of Semiconductor Devices, 2nd ed. (Wiley, New York, 1981).
22. W.E. Spicer, "Photoemissive, Photoconductive, and Optical Absorption Studies of Alkali-Antimony Compounds," *Phys. Rev.* 112, 114 (1958).
23. J.M. Mooney, Ph. D. thesis, University of Arizona, 1986.
24. B.-Y. Tsaun, M.M. Weeks, R. Trubiano, P.W. Pellegrini, T.-R. Yew, "IrSi Schottky-Barrier Infrared Detectors with 10- μ m Cutoff Wavelength," *IEEE Electron Device Lett.* 9, 650 (1988).
25. P. Pellegrini, M. Weeks, C. Ludington, "New 6.5 μ m Photodiodes for Schottky Barrier Array Applications," *Proc. SPIE* 311, 24 (1981).
26. D.E. Mercer, C.R. Helms, "A Diffusion Model for the Internal Photoresponse of PtSi/p-Si Schottky Barrier Diodes," *J. Appl. Phys.* 65, 5035 (1989).

27. J. Cohen, J. Vilms, R.J. Archer, Hewlett-Packard Labs, Palo Alto, CA, Report Nos. AFCRL-68-0651 (1968) and AFCRL-69-0287 (1969).
28. H. Elabd, W.F. Kosonocky, "Theory and Measurements of Photoresponse for Thin film Pd_2Si and $PtSi$ Infrared Schottky-Barrier Detectors with Optical Cavity," *RCA Rev.* 43, 569 (1982).
29. R.H. Fowler, "The Analysis of Photoelectric Sensitivity Curves for Clean Metals at Various Temperatures," *Phys. Rev.* 38, 45 (1931).
30. F. Wooten, R.N. Stuart, "Fowler's Hypothesis and the Determination of Photoemission Thresholds," *Phys. Rev.* 186, 592 (1969).
31. E.O. Kane, "Simple Model for Collision Effects in Photoemission," *Phys. Rev.* 147, 335 (1966).
32. V.L. Dalal, "Simple Model for Internal Photoemission," *J. Appl. Phys.* 42, 2274 (1971).
33. V.E. Vickers, "Model of Schottky Barrier Hot-Electron-Mode Photodetection," *Appl. Opt.* 10, 2190 (1971).
34. J.M. Mooney, J. Silverman, "The Theory of Hot Electron Photoemission in Schottky-Barrier IR Detectors," *IEEE Trans. Electron. Dev.* ED-32, 33 (1985).
35. J. Silverman, P. Pellegrini, J. Comer, A. Golvbovic, M. Weeks, J. Mooney, J. Fitzgerald, "Characterization of Thin $PtSi/p-Si$ Schottky Diodes," *Mat. Res. Soc. Symp. Proc.* 54, 515 (1986).
36. H. Foll, P.S. Ho, "Transmission Electron Microscopy Investigation of Silicide Formation on Slightly Oxidized Silicon Substrates," *J. Appl. Phys.* 52, 5510 (1981).
37. C.A. Crider, J.M. Poate, J.E. Rowe, T.T. Sheng, "Platinum Silicide Formation Under Ultrahigh Vacuum and Controlled Impurity Ambients," *J. Appl. Phys.* 52, 2860 (1981).
38. B.-Y. Tsaur, M.M. Weeks, P.W. Pellegrini, "Pt-Ir Silicide Schottky-Barrier IR Detectors," *IEEE Electron Device Lett.* 9, 100 (1988).
39. J.M. Mooney, private communication.

Chapter 2

The Diffusion Model

Amid the background information introduced in Chapter 1 was a synopsis of the basic principles underlying Schottky barrier photodiode operation. Both the contributions and the shortcomings of previous attempts to model the photoresponse were summarized, and motivation was provided for a new approach to answer the questions remaining in this area. The present chapter begins an analysis of one such approach based on a diffusive description of hot carrier transport. Following a brief discussion of the inapplicability of a “quantum well” representation, the essential formulation of the diffusion model will be presented along with its physical implications. The results of the diffusion analysis will be compared and contrasted with those of earlier models, and optimum diode design will be considered. The study will continue in Chapter 3, which will examine some of the features of the model in greater detail and explore a number of enhancements to the basic formulation.

2.1. Arguments Against a Quantum Well Model

Of the various models that might be invoked to describe the photoresponse of ultra-thin PtSi/*p*-Si Schottky barrier photodiodes and, hopefully, explain some of the unusual results reported, the most obvious candidate would have to be a “quantum well” analog. However, despite the obvious structural similarities to the GaAs quantum devices, there are a number of factors which argue against a quantum well description of silicide Schottky diodes. The band diagram for the ideal Schottky diode is quite different from

that of a typical quantum well device. As Fig. 2.1 indicates, the effective well depth, measured from the bottom of the conduction band in the silicide to the bottom of the conduction band in the silicon, may be assumed to lie between 5 and 10eV. Although the carriers of interest in these diodes are holes, the energy level structure of the well is still determined from the electron picture, so the potential well does rise all the way up to the silicon conduction band edge rather than the top of the valence band. In contrast, a typical

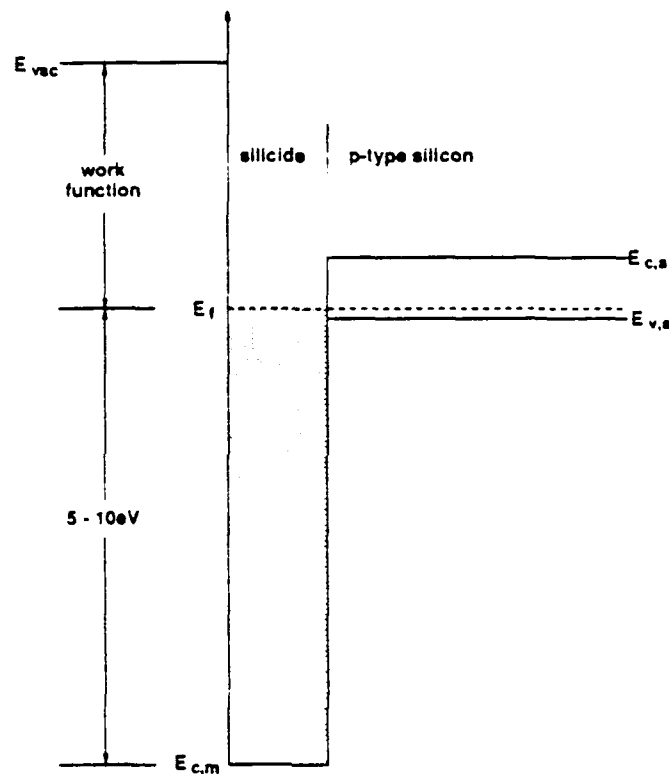


Fig. 2.1. Band diagram for an ideal ultra-thin film Schottky barrier diode.

quantum well device has a well depth on the order of 100meV, approximately two orders of magnitude less than that of the Schottky diode. Finding the energy levels for the "one-dimensional semi-infinite well" of Fig. 2.1 is a fairly basic problem in quantum mechanics and is covered in a number of texts.¹ However, if the effective mass approximation is employed, as it will be throughout this work, the probability current between the silicide and the silicon will not be conserved due to the effective mass discontinuity that exists at

the silicide/silicon interface. There is an effective probability current sink produced for carrier flow into the substrate. This factor presents no major difficulties as long as it is recognized, and details of the calculation will not be presented here. The eigenstates of the well are readily determined; however, more important than the energy levels themselves is the extremely strong dependence observed between the energies and the width of the well. For a silicide film 10 to 20Å thick, a 1Å change in thickness produces a shift in the highest bound states of approximately 1eV. Even an atomically smooth silicide film would be expected to display thickness variations of at least 1Å, which implies that the eigenstates in any physically realizable device would be broadened into bands more than a photon energy wide. This simply illustrates the general principle that in the consideration of quantum mechanical problems concerning either barrier transmission or bound states in potential wells it is the area or volume of the barrier/well that matters, not the width or height/depth alone. Although the ultra-thin Schottky diode is as thin or thinner than standard quantum well devices, the much greater relative depth of its potential well should cause quantum effects to wash out. Moreover, calculation of the electric dipole moment using the eigenstates derived in the exercise above indicates that there should be little absorption of incident light having no electric field component in the direction normal to the diode. The diode response should, therefore, demonstrate strong sensitivity with respect to the angle of incidence of plane polarized light as it varies from normal, increasing greatly with angle. No evidence for the existence of this phenomenon has ever been observed, however.

While the foregoing analysis predicts blurring of quantum properties in ideal diodes, the effect should be even greater in actual devices, which are anything but atomically smooth. The High Resolution Cross Sectional Transmission Electron Microscopy (HRXTEM) micrograph of a test structure from a typical PtSi/*p*-Si detector array fabricated at the Rome Air Development Center (RADC), shown in Fig. 2.2, provides a rather graphic example of this. The silicide film in Fig. 2.2 is practically sinusoidal, with

a peak to valley swing more than twice the film thickness itself. In this case, complete obliteration of any quantum effects might be expected. Optical absorption data derived from transmission and reflectance measurements show no evidence of either significant attenuation at normal incidence or discrete structure, as anticipated.^{2,3} Most detectors, including those analyzed in Chapter 4, do not display undulations of this magnitude; however, the PtSi films are non-epitaxial in all cases and all display some degree of roughness at the atomic level. Therefore, despite the structural similarities between ultra-thin Schottky barrier diodes and quantum well structures, the bulk of the available evidence indicates that a quantum mechanical treatment of the photoresponse of Schottky diodes is inappropriate.

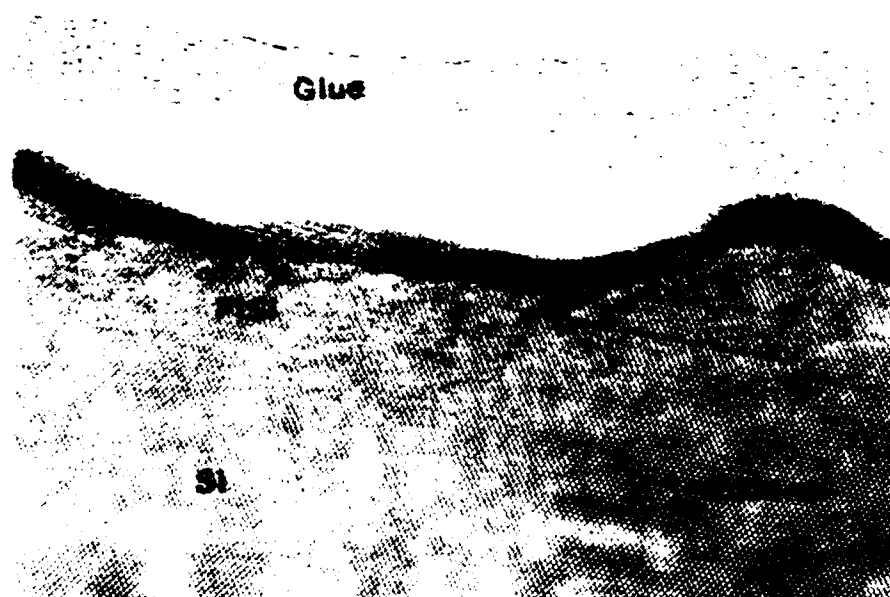


Fig. 2.2. HRXTEM micrograph of a 20Å (nominal) PtSi/*p*-Si Schottky photodiode produced at the Rome Air Development Center. The sample was prepared and analyzed by K.B. Kim.

2.2. The Diffusion Model

In light of the arguments against a quantum well model, it would seem that another approach is called for. The remainder of this chapter and Chapter 3 will explore the modelling of the internal photoemission event as a process analogous to that of thermal diffusion. Diffusion and age theories were used extensively in the early to mid-1960s to relate measured hot electron attenuation lengths in metal layers to theoretical scattering parameters,⁴ but have not been applied to the photoyield problem to any degree due to concern over the angular dependence of the excited carrier distribution function.^{5,6} Diffusion theory may be derived from fundamental transport theory under the assumption that the diffusing particles undergo enough random elastic scattering events that the particle distribution function at a given position in space is almost isotropic with respect to the direction of particle momentum. In theoretical treatments of electron or hole transport in metals, consideration of scattering events is limited mainly to collisions with phonons and other electrons or holes, processes which tend to have mean free paths significantly greater than the film thicknesses employed here. Hot carriers in ultra-thin film Schottky diodes are confined near an emitting boundary which could affect the angular characteristics of the carrier distribution and allow carriers to escape after undergoing relatively few randomizing events, undermining the assumptions of diffusion theory. However, in Schottky diodes used for infrared detection, the carrier energies are sufficiently close to the detector threshold level that the barrier transmission is very low, as will be shown later in this section. Emission at the boundary should have only a minor effect on the angular properties of the distribution in the silicide film. In addition, a comparison of photoresponse data with Monte Carlo calculations indicates that the film boundaries may be considered to be diffuse reflectors,⁵ which implies that the reflection of a hot carrier incident on a boundary may be considered an isotropic elastic scattering event. In the presence of a weakly transmitting barrier, most of the carriers that escape

will undergo many boundary reflections prior to emission, so that even in the absence of other forms of scattering the emitted carrier distribution should be nearly isotropic. Both phonon and carrier-carrier scattering are indeed present, however; although carrier-carrier scattering will, for the most part, be considered an inelastic process. Moreover, the polycrystalline and possibly rough silicide films actually produced should provide several additional sources of scattering. With these considerations in mind, it would seem that a diffusion formulation does warrant examination.

2.2.1. Mathematics of the Diffusion Model

As an initial attempt at a diffusion formulation, a one-dimensional diode structure has been assumed in which the non-ideal morphology of the actual devices is manifested only as a source of quasi-elastic scattering. As an approximation of the higher dimensional cases, the one-dimensional problem clearly includes some angular averaging, and any parameter value having a length dependence will only be accurate to within a normalization factor. Occurrences of this averaging process will be indicated from time to time in the development of the solution.

The one-dimensional diode structure is shown again in Fig. 2.3, along with the optical cavity and an anti-reflection coating typically used. For the PtSi/p-Si Schottky barrier diode, the excited carriers will be holes. The standard one-dimensional diffusion equation applied to hot carriers in the silicide film is given by

$$\frac{\partial p(x,t)}{\partial t} = D \frac{\partial^2 p(x,t)}{\partial x^2} - \frac{p(x,t)}{\tau_r}, \quad (2.1)$$

where $p(x,t)$ represents the excited carrier concentration at position x and time t . The diffusion coefficient D incorporates the effects of the various elastic and quasi-elastic scattering mechanisms present, such as phonon emission and grain boundary scattering. Collisions between holes are accounted for through the recombination time τ_r , the mean time for a hot carrier to collide with a cold one. Such events will be assumed to leave both

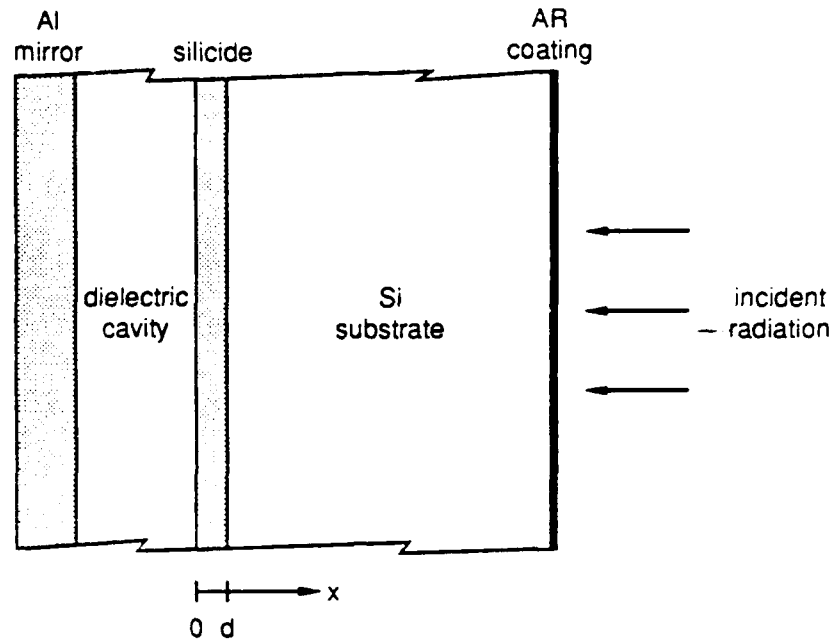


Fig. 2.3. The one-dimensional PtSi/p-Si Schottky barrier diode, shown with the optical cavity structure and an anti-reflection coating to enhance the optical absorption.

carriers involved with insufficient energy to escape the silicide film, in effect resulting in the thermalization of the hot carrier. Carriers incident on the dielectric/silicide interface encounter a high potential barrier and will be reflected back into the film, so the relevant boundary condition there will be

$$D \frac{\partial p(0,t)}{\partial x} = 0. \quad (2.2)$$

In contrast, at the silicide/silicon interface there will be a carrier flux into the silicon substrate which will be assumed to be proportional to the carrier concentration adjacent to the boundary, i.e.

$$-D \frac{\partial p(d,t)}{\partial x} = C p(d,t), \quad (2.3)$$

where C is the barrier escape velocity, a quantity related to the rate at which carriers are emitted over the barrier, and d represents the silicide film thickness. If the initial carrier concentration in the film $p(x,0)$ is given, these equations can be solved simultaneously to

give the concentration at any later time and, therefore, the emitted flux $Cp(d,t)$. Once the emitted flux is determined, the photoyield per photon absorbed in the silicide Y is obtained by integrating the flux over all time $t > 0$ and dividing by the total number of excited carriers at $t = 0$.

The standard diffusion formulation does not specifically address the energy dependence of the excited carrier distribution. Since one would expect the parameters C , τ , and possibly D to vary for carriers having different energies of excitation, it is clear that p should also exhibit an energy dependence. The diffusion problem as stated implicitly assumes a monoenergetic carrier distribution, i.e. $p(x,t)$ is actually $p(x,t,E)$. Since a photon having energy $h\nu$ can produce carriers having energies of excitation anywhere from zero up to $h\nu$ above the Fermi level, some sort of energy averaging will be required in order to obtain the photoyield for a given photon energy from the solution to the diffusion equation. This method of incorporating the energy dependence represents an approximation, and does not include energy losses associated with quasi-elastic scattering processes, such as phonon emission. Carriers lose energy only through inelastic collisions, which effectively remove them from further consideration. One additional note: the boundary condition at $x = d$ implies that there will be emission into the substrate as long as there is a non-zero excited carrier concentration in the film. Since this is not true of carriers excited to energies less than the Schottky barrier height ϕ in the absence of quantum mechanical tunnelling, it is clear that the diffusion problem describes only those carriers excited to energies exceeding the barrier height. Carriers having energies less than the barrier height do not contribute to the yield in this formulation.

With these considerations in mind, the excited carrier distribution at a given energy $p(x,t,E)$ may be obtained from Eqs (2.1)-(2.3) using the method of separation of variables. If the expression $M(x,E)N(t,E)$ is substituted for $p(x,t,E)$, Eq. (2.1) may be manipulated to give

$$\frac{1}{N} \frac{\partial N}{\partial t} + \frac{1}{\tau_r} = D \frac{1}{M} \frac{\partial^2 M}{\partial x^2} . \quad (2.4)$$

Since the two sides of Eq. (2.4) are functions of different variables with the exception of E , each may be set equal to a function of E alone, which will be defined as $-k(E)$ for convenience. The two resulting partial differential equations in one variable are easily solved for M and N to give

$$p(x,t,E) = [A \cos(\sqrt{k/D}x) + B \sin(\sqrt{k/D}x)] \exp[-(1/\tau_r + k)t] . \quad (2.5)$$

The boundary condition at the dielectric/silicide interface, given by Eq. (2.2), implies that $B=0$ in Eq. (2.5), while the emission condition of Eq. (2.3) gives rise to a transcendental equation for k

$$\sqrt{k_j/D} \tan(\sqrt{k_j/D}d) = C/D , \quad (2.6)$$

where the subscript j has been added to reflect the presence of multiple solutions. The concentration may therefore be represented by a superposition of solutions of the form given in Eq. (2.5), i.e.

$$p(x,t,E) = \sum_{j=1}^{\infty} A_j \cos(\sqrt{k_j/D}x) \exp[-(1/\tau_r + k_j)t] . \quad (2.7)$$

Since the equation for $M(x,E)$ derived from Eq. (2.4) is of the Sturm-Liouville form, the set of functions $\cos[(k_j/D)^{1/2}x]$ form an orthogonal basis for functions defined on the interval $x \in (0,d)$. This fact allows the A_j 's to be determined in terms of the initial distribution of hot carriers in the film at $t = 0$. The inner product of the function $\cos[(k_j/D)^{1/2}x]$ with Eq. (2.7) at $t = 0$ leads to the expression

$$A_j = \frac{\int_0^d p(x,0,E) \cos(\sqrt{k_j/D}x) dx'}{\int_0^d \cos^2(\sqrt{k_j/D}x) dx'} . \quad (2.8)$$

The integral in the denominator may be evaluated to give

$$\begin{aligned} \int_0^d \cos^2(\sqrt{k_j/D}x') dx' &= \frac{d}{2} + \frac{1}{4\sqrt{k_j/D}} \sin(2\sqrt{k_j/D}d) \\ &= \frac{d}{2} + \frac{1}{2\sqrt{k_j/D}} \sin^2(\sqrt{k_j/D}d) \end{aligned} \quad (2.9)$$

with proper use of Eq. (2.6) and the identity $\sin(2z) = 2\sin(z)\cos(z)$. An expression for $\sin^2[(k_j/D)^{1/2}d]$ may be obtained by simultaneous solution of Eq. (2.6) and the identity $\sin^2z + \cos^2z = 1$, which produce the result

$$\int_0^d \cos^2(\sqrt{k_j/D}x') dx' = \frac{1}{2} \left[d + \frac{C/D}{(C/D)^2 + k_j/D} \right] \quad (2.10)$$

which along with Eqs. (2.7) and (2.8) in turn provides the solution for $p(x,t,E)$

$$\begin{aligned} p(x,t,E) &= 2 \sum_{j=1}^{\infty} \frac{[(C/D)^2 + k_j/D]}{[(C/D)^2 + k_j/D]d + C/D} \int_0^d p(x',0,E) \cos(\sqrt{k_j/D}x') dx' \\ &\quad \times \cos(\sqrt{k_j/D}x) \exp(-1/\tau_r + k_j)t). \end{aligned} \quad (2.11)$$

The photoyield per absorbed photon giving rise to an excited carrier of energy E is then determined by integrating the emitted flux $Cp(d,t,E)$ over all $t \geq 0$ and normalizing to the total number of excited carriers at $t = 0$, and is given by

$$\begin{aligned} Y(E) &= \frac{2C^2\tau_r}{D} \sum_{j=1}^{\infty} \left\{ \frac{1}{[(C/D)^2 + \alpha_j^2]d + C/D} \right\} \left[\frac{1}{D\tau_r\alpha_j^2 + 1} \right] \\ &\quad \times \left[\frac{\alpha_j}{\sin \alpha_j d} \int_0^d \frac{p(x,0,E)}{P_o(E)} \cos(\alpha_j x) dx \right], \end{aligned} \quad (2.12)$$

where the parameter $\alpha_j \equiv (k_j/D)^{1/2}$ has been defined for clarity and $P_o(E)$ represents the total number of carriers initially excited in the silicide film at energy E . Since the integral in the final bracketed term depends on $p(x,0,E)$ and, therefore, on the optical absorption

profile, it will, in general, be complicated. However, in a number of relevant instances the integral may be readily evaluated. If the optical absorption in the film is uniform, i.e. $p(x,0,E)$ is constant with respect to x , the final term reduces to $1/d$. This should be a reasonable approximation in the thin-film case. While a constant concentration profile does not satisfy the boundary conditions for the problem, it may still be expanded in terms of the normal modes of the system and does not violate the assumptions upon which Eq. (2.12) was based.⁷ In addition, if a single carrier is excited at $x = a$, the initial concentration will be proportional to a delta function, and the final term becomes $\alpha_j \cos(\alpha_j a) / \sin(\alpha_j d)$. In any event, the total photoyield per absorbed photon of energy $h\nu$ can be determined from the relation

$$Y = \langle Y(E) \rangle = \frac{\int_{\phi}^{h\nu} g(E) Y' E dE}{\int_0^{h\nu} g(E) dE} ,$$

or

$$Y \approx \frac{1}{h\nu} \int_{\phi}^{h\nu} Y' E dE \quad (2.13)$$

if both the density of states $g(E)$ and their absorption cross-section are fairly constant within $h\nu$ of the Fermi level. Here ϕ represents the Schottky barrier height, and all energies are measured from the Fermi level. As indicated earlier, C , τ_r , and possibly D may depend on the value of E , creating the potential for a fairly complicated energy integral. However, in the case of PtSi/*p*-Si infrared detectors, $\phi \geq 0.19$ eV and $h\nu \leq 1.0$ eV, which restricts the interval of integration to a narrow range of energies and suggests the use of various approximation techniques. The simplest approximation involves the replacement of C , τ_r , and D by their mean values for a given photon energy. This method will be applied here; more accurate methods will be discussed in Chapter 3. If it is further assumed that the normalized initial concentration profile is independent of energy, which

should be the case for a fairly constant density of states and absorption cross section near the Fermi level, the ratio $p(x,0,E)/P_o(E)$ may be replaced by $p(x,0)/P_o$ and the yield per absorbed photon of energy $h\nu$ then becomes

$$Y = \frac{2C^2\tau_r}{D} \left(\frac{h\nu - \phi}{h\nu} \right) \sum_{j=1}^{\infty} \left\{ \frac{1}{[(C/D)^2 + \alpha_j^2]d + C/D} \right\} \left[\frac{1}{D\tau_r\alpha_j^2 + 1} \right] \times \left[\frac{\alpha_j}{\sin \alpha_j d} \int_0^d \frac{p(x,0)}{P_o} \cos(\alpha_j x) dx \right], \quad (2.14)$$

where C , τ_r , and D are functions of $h\nu$. Inspection of this relation reveals that there are essentially only two independent variables, since C , τ_r , and D never appear individually.

The foregoing expression may be readily evaluated numerically; however, in certain instances the sum converges quite rapidly and the result is greatly simplified. If the barrier transmission probability is small or the elastic scattering processes in the silicide film are weak, i.e.

$$\frac{Cd}{D} \ll 1, \quad (2.15)$$

then the sum may be approximated very accurately by the first term only and the yield equation may be reduced to

$$Y = \left(\frac{h\nu - \phi}{h\nu} \right) \frac{1}{1 + d/(C\tau_r)}. \quad (2.16)$$

In this limit, the diffusion constant does not appear in the expression for Y and the number of variables is reduced to one ($C\tau_r$). The vanishing of the diffusion constant in Eq. (2.16) would seem to imply that the elastic scattering parameters have a negligible effect on the one-dimensional photoyield when this approximation is valid.

The limiting case discussed above may be cast in a more physical light through the use of some simplifying assumptions regarding the parameters C and D . As mentioned earlier, $C = \langle C(E) \rangle$ is the mean barrier escape velocity for carriers excited by incident

photons of energy $h\nu$. If the barrier was perfectly transmitting, the escape velocity for incident carriers would simply be the average component of the carrier velocity in the direction normal to the barrier. The mean carrier speed should be approximately equal to the Fermi velocity v_f for $h\nu \leq 1.0$ eV. If θ represents the angle between the trajectory of a carrier incident on the barrier and the surface normal, then the normal component of the carrier velocity will be $v_f \cos \theta$. For an isotropic carrier velocity distribution, the average value of $v_f \cos \theta$ over the range $0 \leq \theta \leq \pi/2$ will be $1/2v_f$. However, since the barrier will not, in general, be perfectly transmitting, the transmission function $T = \langle T(E) \rangle$ must be factored in as well, which leads to a mean escape velocity of $1/2v_f T$ for carriers incident on the barrier. Since C is the escape velocity for all carriers adjacent to the barrier, of which only half will actually be incident in an isotropic distribution, it may then be expressed as $C \approx 1/4v_f T$. The diffusion constant D may be modelled to first order using the kinetic theory of gases.⁸ This method gives $D \approx v_f L_s / 3$, where L_s represents a mean free path for quasi-elastic scattering events and three dimensional effects have been explicitly included. Eq. (2.15) may now be expressed as

$$L_s \gg \frac{3}{4} T d . \quad (2.17)$$

A simple estimate of T may be made using a semi-classical "escape-cone" argument similar to the analysis performed by Mooney² and illustrated in Fig. 2.4. In this diagram, it is assumed that the bands in both the semiconductor and the silicide are parabolic, and details of the band structure matching at the silicide/silicon interface are ignored. The parabolic approximation should be quite accurate for the semiconductor; it will be less so in the silicide.^{9,10} However, the same assumptions are commonly employed in ballistic transport models,^{11,12,13,14} and they allow a tractable result to be reached here. The parabolicity of the silicide conduction band leads to the spherical constant energy (or, equivalently, constant k-vector) surfaces shown in the figure. As in the derivation of the expression for D , this approach involves a three-dimensional treatment. Since electrons

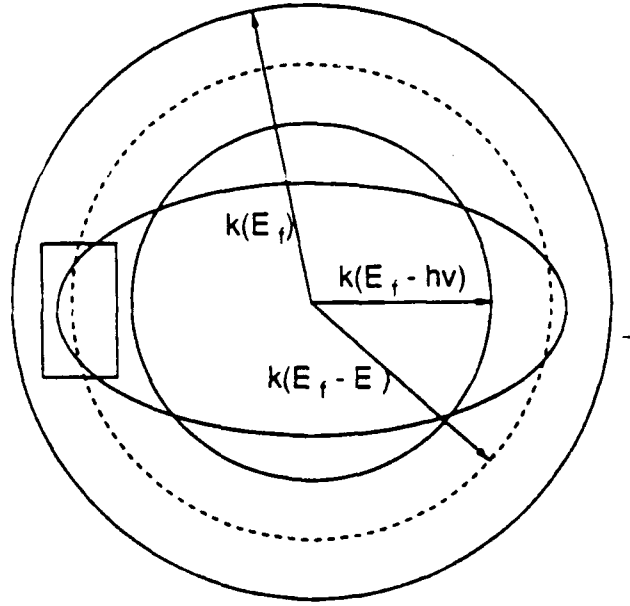


Fig. 2.4. The "escape cone" for excited holes in k -space. The spheres represent states of constant energy or k -vector for parabolic energy bands. States from which holes may be emitted over the Schottky barrier lie within the ellipsoid. For a barrier on the right and holes of energy E , the relevant region of k -space is indicated by the box.

initially having energies lying between the Fermi level and $h\nu$ below it will be excited by incoming photons, these states constitute the excited hole states contained between the spheres of radii $k(E_f)$ and $k(E_f - h\nu)$ in k -space. If the total energy and parallel momentum of a hole surmounting the barrier are conserved, the criterion for emission becomes

$$\frac{\hbar^2 k_{\perp}^2}{2m_m} + \frac{\hbar^2}{2} \left(\frac{1}{m_m} + \frac{1}{m_s} \right) k_{\parallel}^2 \leq E_f - \phi, \quad k = \sqrt{\frac{2m_m}{\hbar^2} (E_f - E)}, \quad (2.18)$$

where m_m and m_s are the hole effective masses in the silicide (or "metal") and the semiconductor, respectively; k is the excited hole wave vector in the silicide, resolved into its components parallel and perpendicular to the interface; and E_f is the Fermi energy of the silicide. Note that this is somewhat different from the corresponding criterion for electron emission from a metal or silicide into an n -type semiconductor, which simply states that the energy associated with the normal component of the hot electron momentum must exceed the height of the barrier. In addition, it should be mentioned that the conservation

of parallel momentum is somewhat of a question, since this assumption also implies specular reflection and it appears, as noted in the beginning of this section, that scattering from the interface is diffuse. The appearance of diffuse reflection, however, may simply result from the approximation of what is actually a somewhat rough interface by a theoretically abrupt one. Eq. (2.18) corresponds to an ellipsoid in k -space within which a state must lie for emission to be allowed. Only half the ellipsoid is actually relevant, since states in the other half will be directed away from the barrier. The transmission function for holes excited to an energy E relative to the Fermi level is then the fraction of the surface area of the hemisphere of radius $k(E_f - E)$ lying within the half ellipsoid, which lies within the half angle $\theta(k)$ given by

$$\sin \theta(k) = \left(\frac{k_{\parallel}}{k} \right) \leq \left(\frac{m_s}{m_m} \right)^{1/2} \left(\frac{E - \phi}{E_f - E} \right)^{1/2} \approx \left(\frac{m_s}{m_m} \right)^{1/2} \left(\frac{E - \phi}{E_f} \right)^{1/2}, \quad (2.19)$$

where it has been observed that $E_f \gg h\nu$. The transmission function for carriers of a given energy $T(E)$ may then be expressed as

$$T(E) = \frac{1}{2\pi} \int_0^{2\pi} \int_0^{\theta(k)} \sin \theta' d\theta' d\phi' = \frac{1}{2} \left(\frac{k_{\parallel}}{k} \right)^2 = \frac{1}{2} M \frac{E - \phi}{E_f}, \quad (2.20)$$

where terms have been retained to second order in (k_{\parallel}/k) and M denotes the ratio m_s/m_m . $T(E)$ may then be averaged over the energy range relevant to the diffusion model to give an expression for T

$$T = \langle T(E) \rangle = \frac{1}{h\nu - \phi} \int_{\phi}^{h\nu} T(E) dE = \frac{1}{4} M \frac{h\nu - \phi}{E_f}. \quad (2.21)$$

Note that as in the evaluation of Eq. (2.13) for Y , a constant density of states has been assumed which eliminates the usual factor of $E^{1/2}$ from the integral. If it is assumed that m_m is approximately equal to the free electron mass and that m_s is an average of the light and heavy hole effective masses in silicon¹⁵ weighted by their relative transmission

probabilities, then $M \approx 0.4$. If it is further assumed that $E_f = 8.5\text{eV}$,⁹ then $T \leq 0.01$ for $h\nu \leq 1.0\text{ eV}$. This implies that the simplified yield expression in Eq. (2.16) should hold if $L_s \gg (7.5 \times 10^{-3})d$, or $L_s \gg 3.75\text{Å}$ for $d = 500\text{Å}$ and $L_s \gg 0.15\text{Å}$ for $d = 20\text{Å}$. Based on this analysis, it would appear that the limit will be reached in any physically realizable thin-film PtSi/p-Si diodes. Moreover, since M and E_f will have similar values in other materials, the condition should be satisfied for most thin-film Schottky barrier devices, providing the incident photon energy is not too large. Because the barrier transmission probability is so small, the limiting condition is reached even if scattering is fairly strong, and the scattering parameter D will not enter into the expression for the photoyield. Using the foregoing expressions for C and T , the parameter $C\tau_r$ may be replaced by

$$C\tau_r = \nu_f \tau_r M \frac{h\nu - \phi}{16E_f} = L_r M \frac{h\nu - \phi}{16E_f} \quad (2.22)$$

where the quantity $\nu_f \tau_r$ is equated with the inelastic scattering length L_r , which will, in general, be a function of $h\nu$. The simplified yield expression may now be recast as

$$Y = \frac{h\nu - \phi}{h\nu} \left[\frac{1}{1 + 16 E_f d / [L_r M (h\nu - \phi)]} \right] \quad (2.23)$$

It should be noted that this expression is similar in form to the result that would be obtained from a one-dimensional ballistic transport model in which phonon scattering has been completely ignored.

As indicated above, values of Cd/D approaching or exceeding one may not be physically meaningful. However, in the event that $Cd/D \geq 1$, no comparably simple reduction in the general form is possible and the yield must be determined using the full solution. Fig. 2.5 shows how the yield varies with C/D for a given value of $C\tau_r$. Curve (A) corresponds to the $Cd/D \ll 1$ limit, while for curve (B), $Cd/D \gg 1$ for $d \geq 100\text{Å}$. It seems that the effect of elastic scattering in the thin-film devices, if important at all, is a reduction in the device photoyield. This contrasts with the case of thicker diodes, in

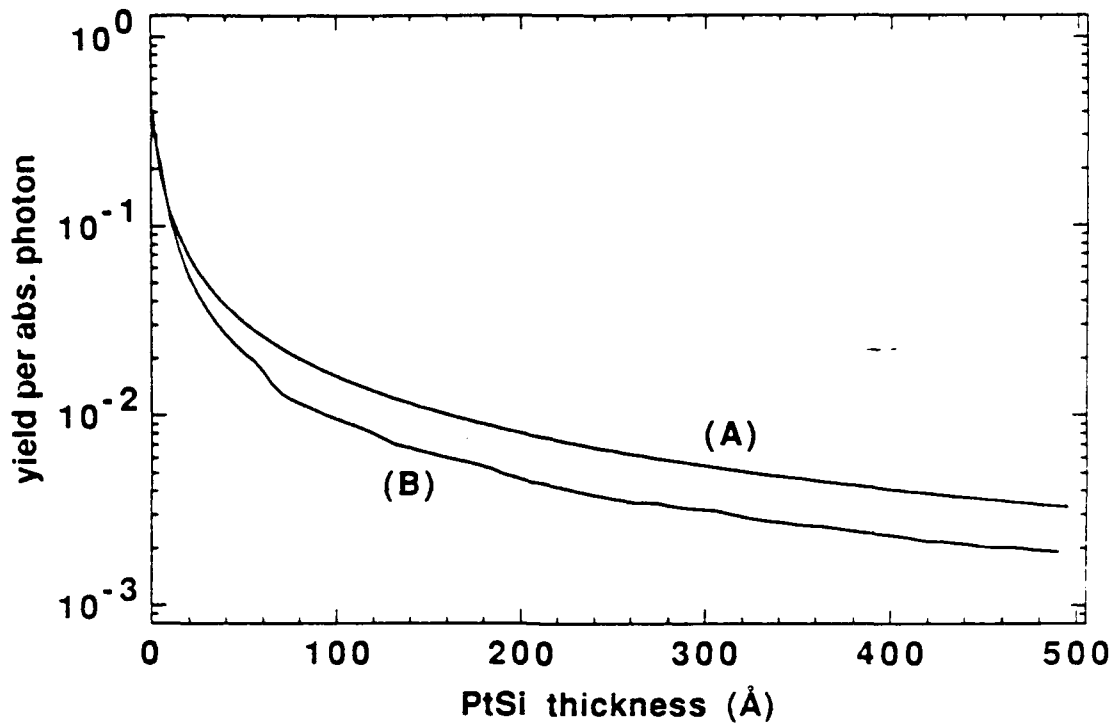


Fig. 2.5. The variation of the yield per absorbed photon with the parameter C/D . The value of $C\tau_r$ is fixed at 4\AA , and the incident photon energy is assumed to be $3.07\mu\text{m}$. Curve (A) is calculated with the assumption that $C/D=(5000\text{\AA})^{-1}$, or $Cd/D\ll 1$; while curve (B) is calculated with $C/D=(12.5\text{\AA})^{-1}$, or $Cd/D\gg 1$ over much of the thickness range shown. The lack of smoothness in curve (B) results from the limited precision of the numerical procedure used for its calculation.

which elastic scattering in the bulk is the only process by which carriers not initially excited into an escape trajectory may be redirected into one. Boundary reflections are apparently more efficient at redirecting momentum than are bulk scattering processes.

2.2.2. Evaluation of Model Parameters

Experimental data on the photoyield of the thin-film PtSi/*p*-Si system has become available through the work of Mooney.² Mooney's results are presented in a series of Fowler plots showing the photoyield per absorbed photon as a function of incident photon energy for diodes with various silicide layer thicknesses. A summary of the data appears in Table 2.1. In the table, the parameter C_1^* is obtained by fitting the function

$$C_1^* \frac{(h\nu - \phi)^2}{h\nu}$$

to the data. On a Fowler plot, this represents a linear fit. Note that C_1^* differs from the C_1 parameter commonly used in the literature, which includes the effects of optical absorption. Of the ten diodes examined by Mooney (numbered two to eleven), only nine were used in this work. The rejected diode showed a photoresponse similar to that in the diodes with PtSi layers five times its own thickness, a response too inconsistent to be considered here. The Fowler plots may be transformed to give the photoyield as a

Table 2.1. Summary of the experimental data collected by Mooney on the photoyield per absorbed photon of PtSi/p-Si Schottky barrier diodes. The rise in the error limits at smaller silicide thicknesses reflects the increase in curvature of the Fowler plots in this range.

Diode no.	PtSi thickness (Å)	Barrier height (eV)	$\sqrt{C_1^*}$ (eV ^{-1/2})	C_1^* (eV ⁻¹)
2	10	0.22	1.04 ± 0.10	1.08 ± 0.21
4	20	0.22	0.95 ± 0.15	0.90 ± 0.29
5	40	0.24	0.60 ± 0.05	0.36 ± 0.06
6	80	0.25	0.48 ± 0.04	0.23 ± 0.04
7	100	0.22	0.54 ± 0.04	0.29 ± 0.04
8	100	0.23	0.54 ± 0.03	0.29 ± 0.03
9	120	0.25	0.38 ± 0.01	0.14 ± 0.01
10	200	0.24	0.38 ± 0.01	0.14 ± 0.01
11	400	0.25	0.35 ± 0.02	0.12 ± 0.01

function of thickness at a number of different photon energies, a form more suitable for comparison with the diffusion model. The model has been fitted to the transformed data at each energy using a simple logarithmic least squares algorithm; some representative examples are presented in Fig. 2.6. Examination of the parameter values derived from the

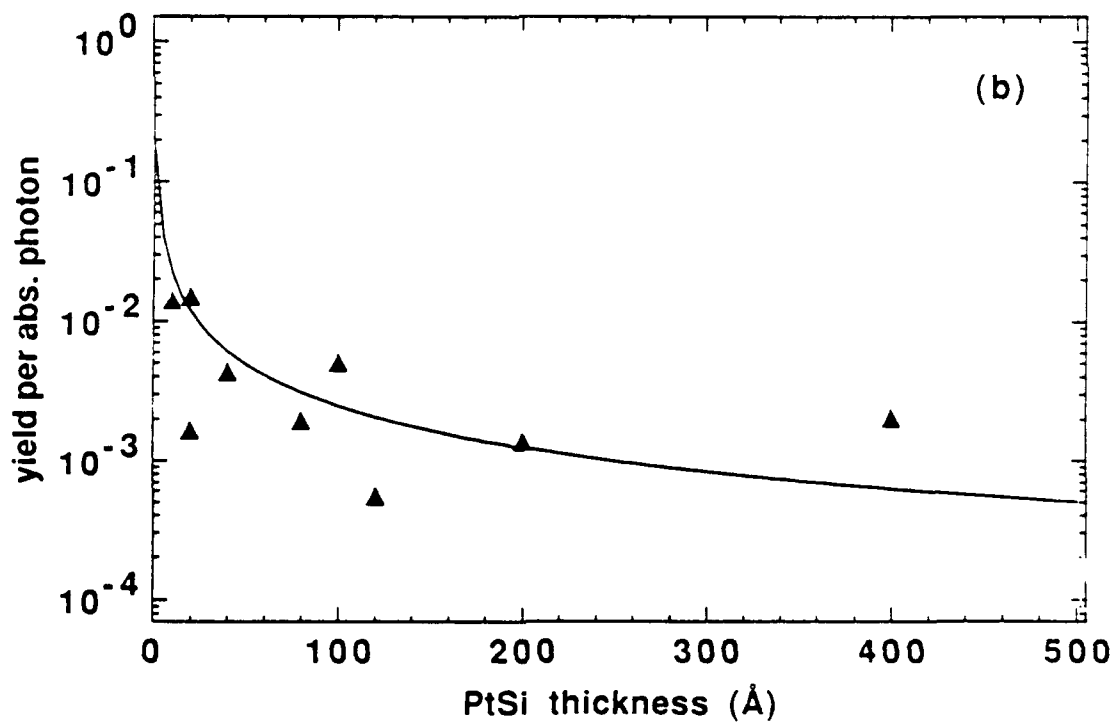
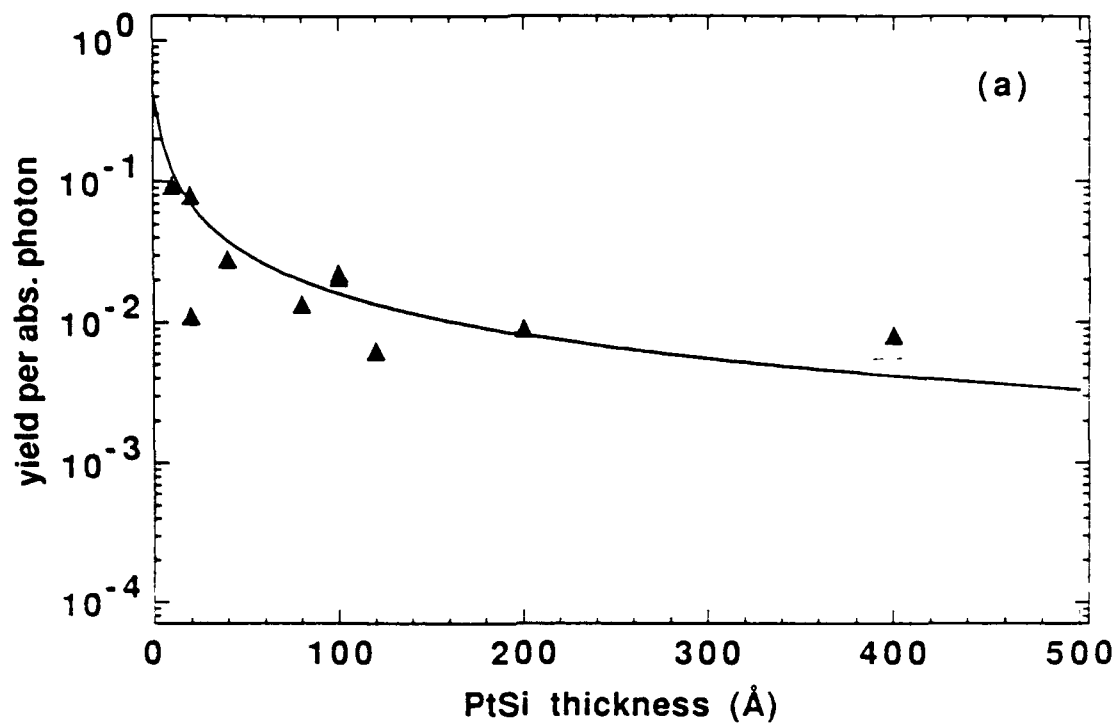


Fig. 2.6. The optimum fit of the diffusion model to the experimental data of Mooney taken at incident photon energies of (a) $3.07\mu\text{m}$ and (b) $4.25\mu\text{m}$.

procedure just described indicates that the data conforms to the limiting case $Cd/D \ll 1$ mentioned earlier, and plots derived from the simplified yield expression were found to be indistinguishable from those produced by the general expression over the range of silicide layer thicknesses considered. The value of $C\tau_r$, obtained by fitting the simplified yield expression to the data is plotted as a function of energy in Fig. 2.7. The plot suggests that $C\tau_r$ is a fairly linear function of the photon energy within the relevant span of energies. If the expression for $C\tau_r$ given in Eq. (2.22) is examined, it is apparent that a linear function will be obtained if τ_r (or L_r) varies slowly with the incident photon energy over the relevant range. If L_r is assumed to be constant, a least squares fit of Eq. (2.22) to the

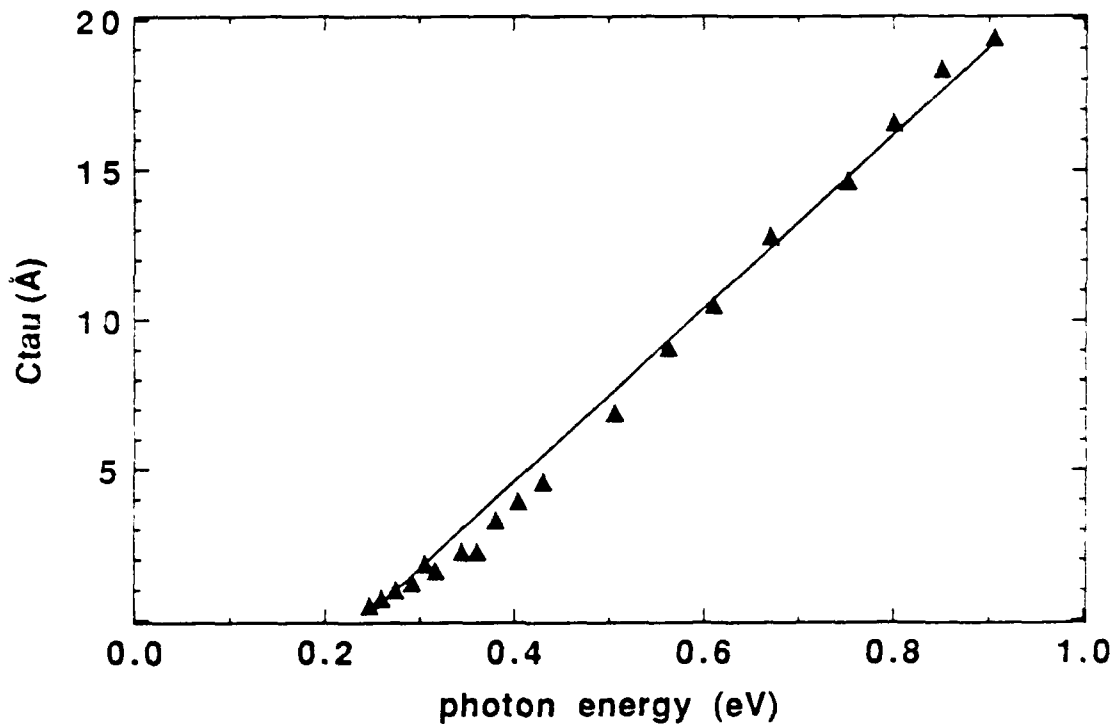


Fig. 2.7. The values of $C\tau_r$ as a function of energy obtained by fitting the diffusion model to Mooney's data, together with an optimized linear fit.

values of $C\tau_r$ obtained from the data over the range $0.25\text{eV} \leq h\nu \leq 0.91\text{eV}$ implies that $L_r \approx 8000\text{Å}$ if $E_f = 8.5\text{eV}$, $M=0.4$, and $\phi = .235\text{eV}$, the average optical barrier height for Mooney's diodes. This result agrees with previous estimates of inelastic scattering

lengths for hot holes.¹⁶ It should be noted, however, that the various approximations involved in the calculation, especially the angular averaging inherent in the one-dimensional treatment, imply that this result may be correct only to within a factor of two or so.

Examination of the results of the data fitting procedure shown in Fig. 2.6 reveals two points worth mentioning. There clearly exists a fair amount of scatter in the data, especially at the longer wavelengths. Estimating the quality of the fits for photon energies approaching the Schottky barrier height is, therefore, somewhat difficult. Observation of the fits at the shorter wavelengths reveals that the yield curve derived from the model seems to possess less curvature at the smallest film thicknesses than the data. This is not a complete surprise, since the model does not include energy losses resulting from elastic collisions. Nonetheless, the fits appear to be reasonably good, and a comparison of the results of the simplified yield expression incorporating the linear approximation to $C\tau_r$ with Mooney's Fowler plots shows good agreement as the examples in Fig. 2.8 indicate.

2.2.3. Comparison with Previous Models

In Chapter 1, various ballistic transport models developed prior to this work were discussed. Specific models of interest include those described by Vickers,¹¹ Dalal,¹² and Mooney and Silverman.¹³ Each of these leads to photoyield expressions more complicated than the one presented in Eq. (2.23), and it is instructive to examine these models in the limit suggested by the diffusion formulation and to compare their results with Eq. (2.23). In all three of these models, the elastic scattering length appears explicitly. Since the diffusion formulation implies that the exact values of the quasi-elastic scattering parameters should be unimportant in determining the photoyield for diode thicknesses below 500Å, it will be assumed that the elastic scattering length is infinite. If it is further assumed that $d \ll L_r$, a hypothesis which holds in the diffusion model, Vickers' expression for the photoyield per absorbed photon becomes

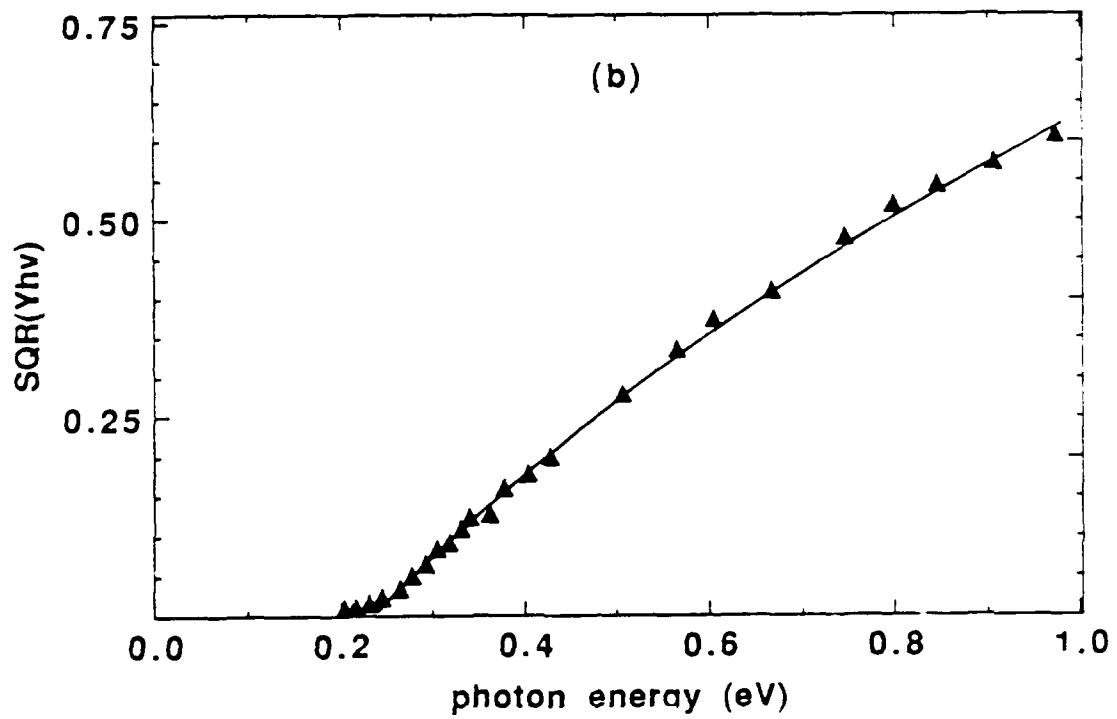
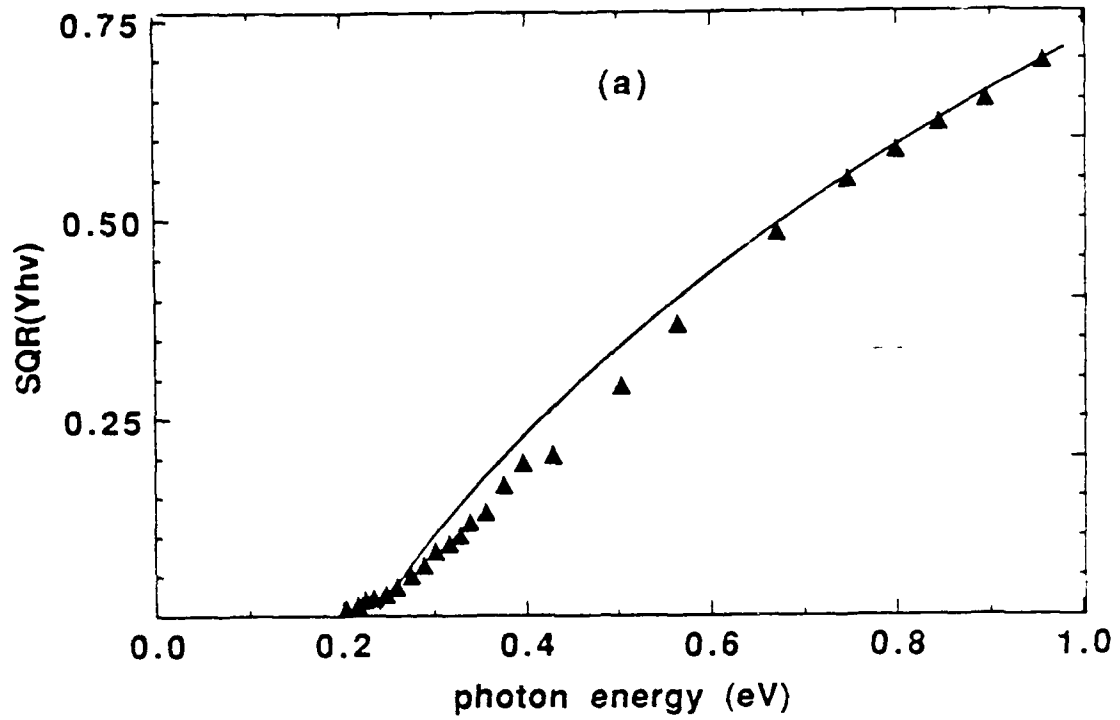


Fig. 2.8(a-b). Fowler plots comparing the results of the diffusion model to Mooney's experimental data for diodes with (a) 10Å and (b) 20Å PtSi layers.

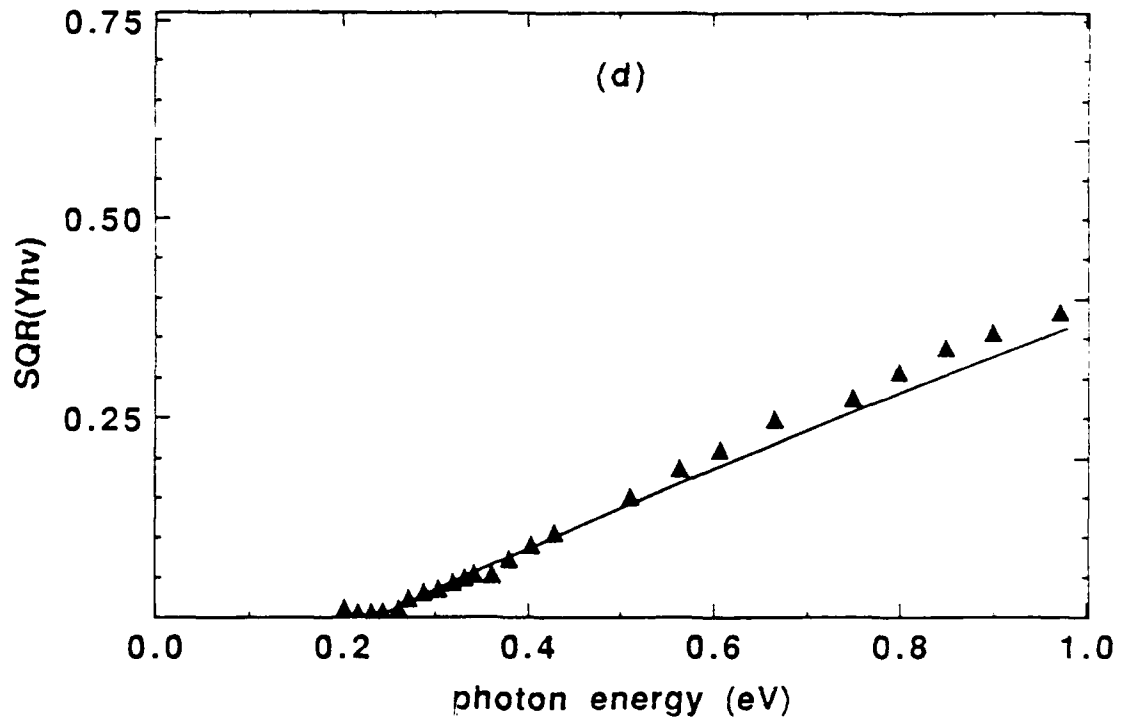
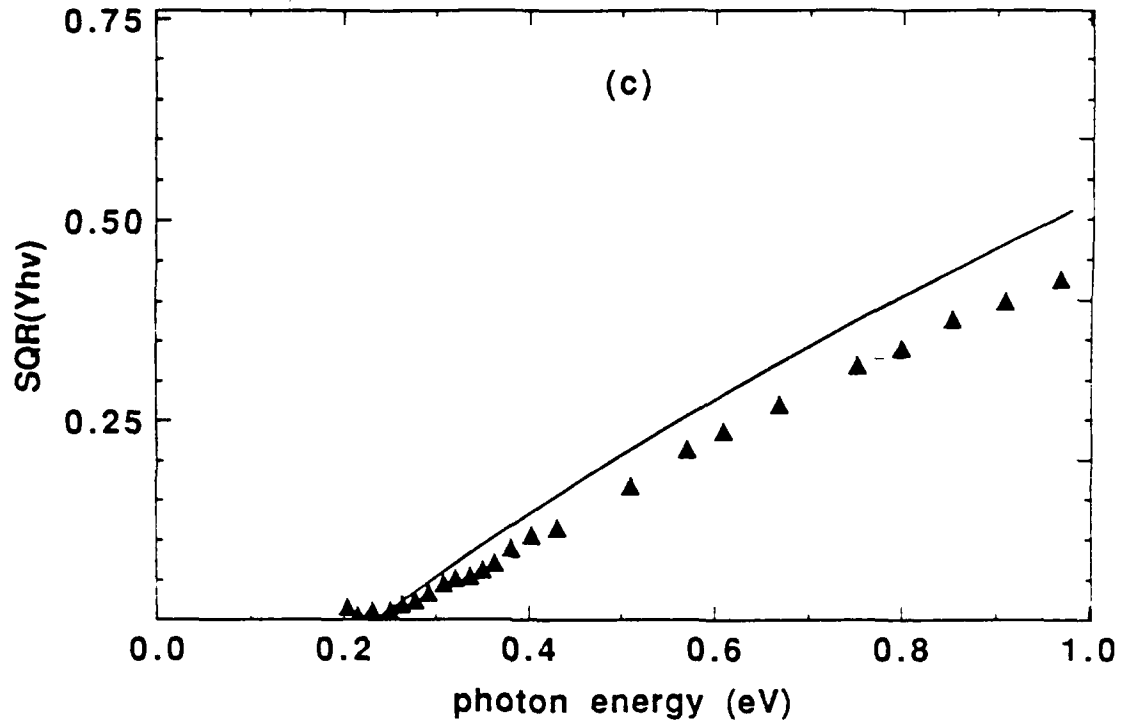


Fig. 2.8(c-d). Fowler plots comparing the results of the diffusion model to Mooney's experimental data for diodes with (c) 40Å and (d) 100Å PtSi layers.

$$Y_V \approx Y_f \left\{ \frac{1}{2} + \frac{1}{(d/L_r)[\ln(L_r/d) + 1 - \gamma]} \right\}, \quad (2.24)$$

where

$$Y_f = M \frac{(h\nu - \phi)^2}{8E_f h\nu} \quad (2.25)$$

is the Fowler yield,² γ is Euler's constant, and L_r has been substituted for the L_e used by Vickers. As $d \rightarrow 0$, this expression becomes infinite. This result is no surprise, since Vickers assumes the total fraction for carriers emitted is sufficiently small that the excited carrier distribution is never corrected for the transmitted flux. If the Dalal model is examined under the same assumptions, the yield takes the form¹⁷

$$Y_D \approx \frac{1}{1 + (d/L_r Y_f)}. \quad (2.26)$$

This relation is similar to the prediction of the diffusion model, although the photon energy dependence is somewhat different. In the limit as $d \rightarrow 0$, however, Y_D approaches one; since Dalal failed to correct for the lack of transmission of carriers excited to energies less than the Schottky barrier height. In contrast to the Vickers and Dalal results, the Mooney and Silverman formulation appears to provide a much more accurate description of the yield in the zero thickness limit. To examine the Mooney model, two additional assumptions are required. Mooney includes the effects of both energy losses due to phonon scattering and quantum mechanical reflection at the barrier, two phenomena not dealt with in the present diffusion formulation. Removing these two extensions, the Mooney photoyield becomes

$$Y_M \approx Y_f \left\{ 1 + \frac{(1 - Y_f/Y_\infty) \left(1 - \frac{5}{4} d/L_r \right) - \left(1 - \frac{3}{2} Y_f/Y_\infty \right) [d/L_r [\ln(L_r/d) + 1 - \gamma]]}{Y_f/Y_\infty + (1 - 2Y_f/Y_\infty) [d/L_r [\ln(L_r/d) + 1 - \gamma]]} \right\}. \quad (2.27)$$

where

$$Y_{\infty} = \frac{h\nu - \phi}{h\nu}. \quad (2.28)$$

As $d \rightarrow 0$, Y_M becomes $(h\nu - \phi)/h\nu$, which is identical to the diffusion result. For the purpose of comparison, Eqs. (2.23), (2.24), (2.26) and (2.27) are all plotted along with Mooney's photoyield data for $h\nu = 3.07\mu\text{m}$ in Fig. 2.9. In each case, the value of L_r was chosen to optimize the fit to the data. From the figure, it is apparent that there exists no major difference between the fits for $10\text{\AA} \leq d \leq 500\text{\AA}$. The Vickers and Mooney models predict a somewhat higher yield for silicide thicknesses larger than 100\AA , but the difference is less than a factor of two. However, to obtain these curves, the Vickers and Mooney models require values of L_r on the order of $20,000\text{\AA}$, while the diffusion and Dalal models require L_r on the order of $4,000$ to $8,000\text{\AA}$. The smaller values are much more in line with the theoretical estimates of L_r .¹⁶ Moreover, while all of the models fit

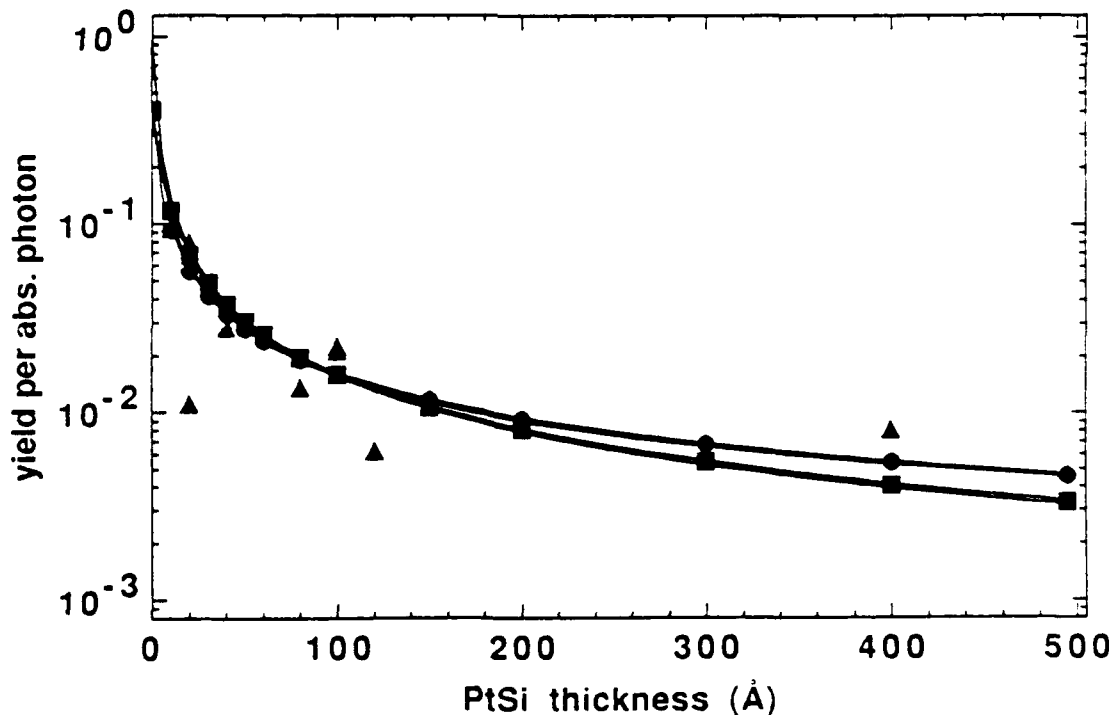


Fig. 2.9. Comparison of various models shown with the experimental data (designated by triangles) taken at a photon energy of $3.07\mu\text{m}$. At silicide thicknesses greater than 150\AA , the diffusion model (squares) and the Dalal model are virtually identical, as are the Mooney model (circles) and the Vickers model.

the data reasonably well, the diffusion formulation shows the relative importance of barrier transmission and elastic scattering processes in the determination of the photoyield in a much clearer fashion than the ballistic approach.

2.2.4. Determination of Quantum Efficiency

Although the primary concern so far has been the calculation of the internal photoyield per absorbed photon, the quantity of interest in the application of these devices is the yield per incident photon, or quantum yield. While the yield per absorbed photon is maximized as the silicide film thickness approaches zero, the fact that the optical absorbance of the film drops to zero at that point leads to an optimum film thickness maximizing the yield per incident photon which is obviously larger than zero. Given an optical structure, the fraction of incident light of a specified wavelength absorbed by the film may be predicted as function of thickness. This function may be multiplied by Eq. (2.23) to give the photoyield per incident photon; the position of its maximum value reflecting the tradeoff between absorption and emission. As an example, Fig. 2.10 shows the photoyield per incident photon at three different wavelengths for the device structure of Fig. 2.3. Calculation of the absorption of the optical cavity has been described in the literature and is explained in more detail in Appendix A. Repeated calculation of the yield versus silicide thickness while varying the thickness of the SiO₂ dielectric layer allows the determination of the optimum cavity and silicide layer thicknesses for a given wavelength. Table 2.2 lists the results of this exercise, the necessary optical constants for which were taken from Mooney^{2,3} and Palik.¹⁸ It should be noted that the cavity size may also be varied to increase the yield for a suboptimal PtSi layer thickness above the level shown in Fig. 2.10, but the maximum quantum efficiency obtained for the device will always be less than the value listed in Table 2.2 for that wavelength.

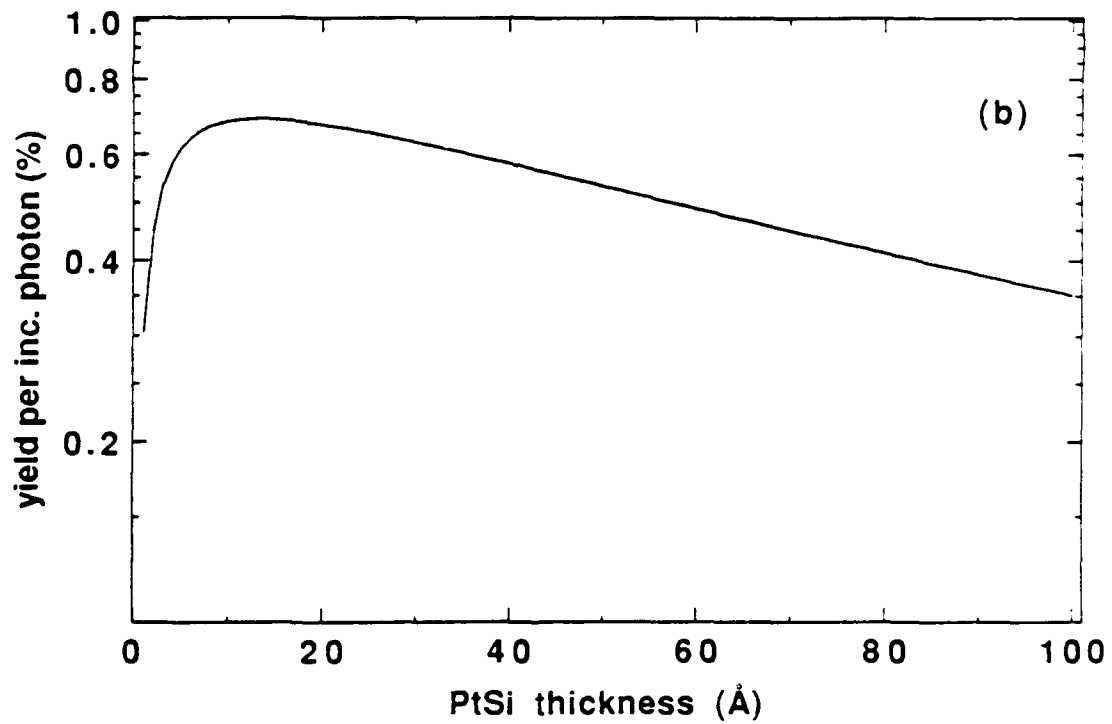
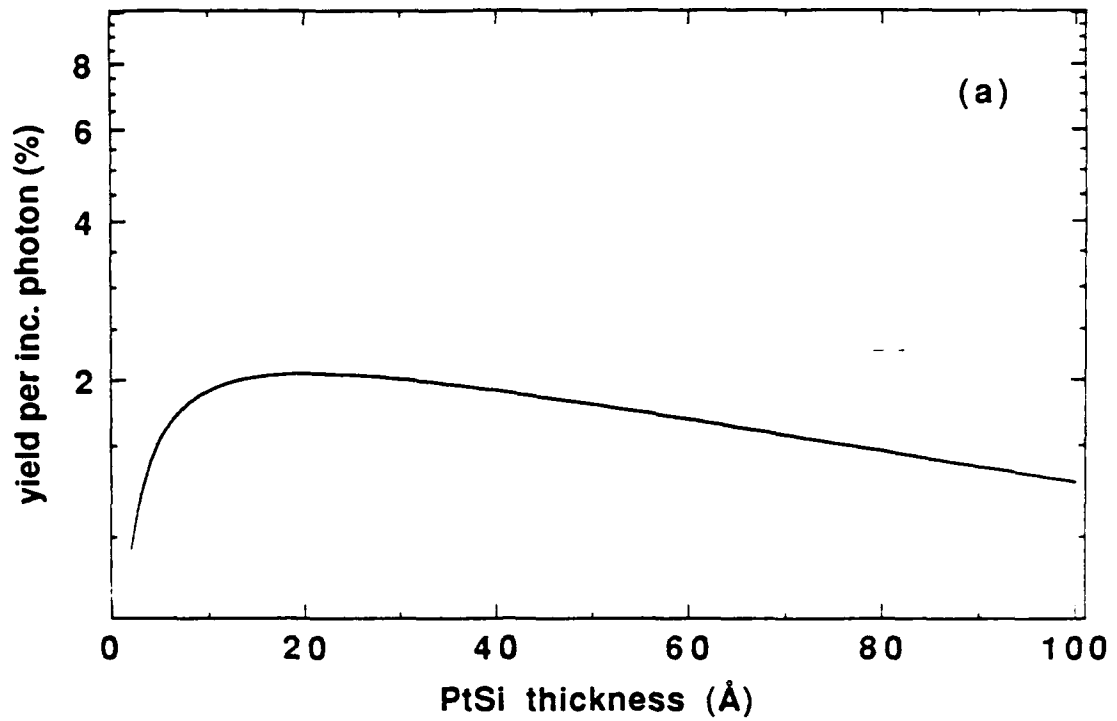


Fig. 2.10(a-b). The photoyield per incident photon for PtSi/*p*-Si diodes at wavelengths of (a) 3.07 μ m and (b) 4.07 μ m. A tuned optical cavity and an anti-reflection coating are assumed to be present in each case.

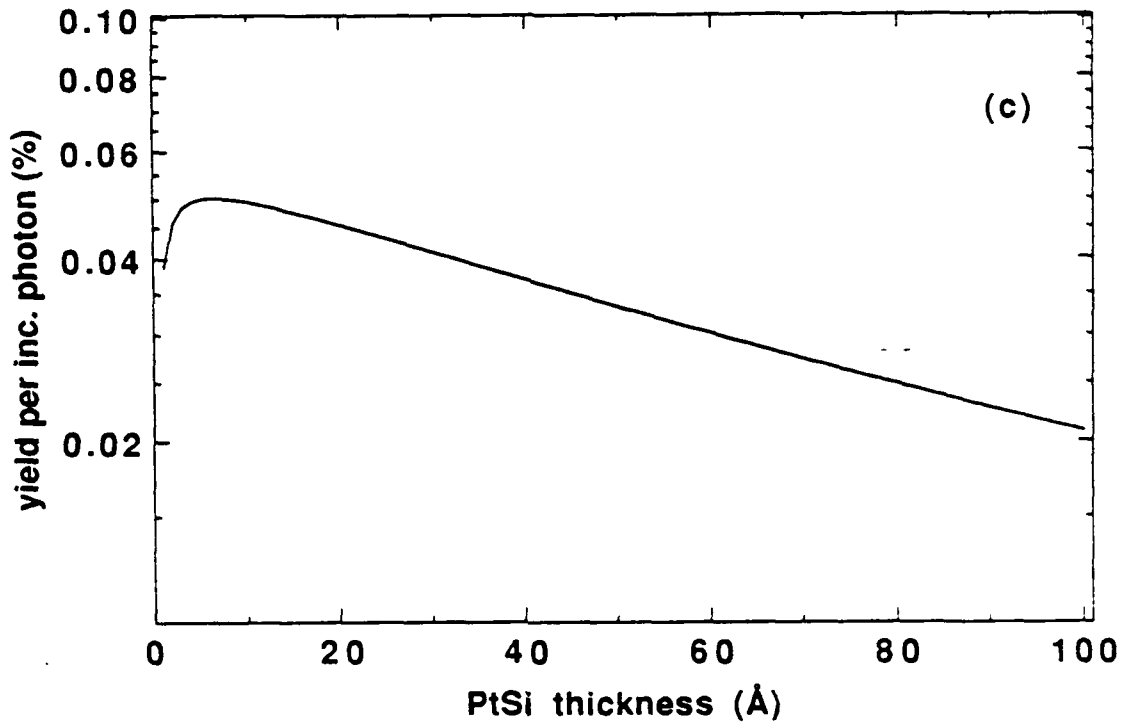


Fig. 2.10(c). The photoyield per incident photon for a PtSi/*p*-Si diode at a wavelengths of 5.01 μ m. A tuned optical cavity and an anti-reflection coating are assumed to be present.

Table 2.2. Optimum optical cavity and PtSi layer thicknesses and corresponding quantum efficiencies for incident light at various wavelengths.

Wavelength (μ m)	Optimum PtSi Thickness (\AA)	Optimum Cavity Width (\AA)	Quantum Efficiency (%)
3.07	20	6000	2.05
4.07	13	7900	0.70
5.01	6	9600	0.05

Both Fig. 2.10 and Table 2.2 indicates that the optimum silicide film thickness at all wavelengths from 3 to 5 μ m will be extremely thin, especially at the longer wavelengths. A simple polynomial fit to the optical absorption curves of the diode/cavity structures,

some of which are shown in Appendix A, shows that the absorption in the relevant thickness range may be approximated very closely by the expression

$$A \approx \frac{d}{L_{a1}} \left(1 - \frac{d}{L_{a2}} \right), \quad (2.29)$$

where

$$L_{a1} = 50 \left(\frac{1}{0.39 + 0.19/h\nu} \right) \text{ and } L_{a2} = 98 \left(\frac{0.49 + h\nu}{1.09 - h\nu} \right). \quad (2.30)$$

L_{a1} and L_{a2} will have the dimensions of angstroms when the photon energy is given in units of electron-volts. Eqs. (2.29) and (2.30) may then be combined with either Eq. (2.16) or Eq. (2.23) to give a simple equation for the overall quantum efficiency of the PtSi/*p*-Si Schottky photodiode with optical cavity

$$\eta \approx \left(\frac{h\nu - \phi}{h\nu} \right) \frac{d}{L_{a1}} \left(1 - \frac{d}{L_{a2}} \right) \left(\frac{1}{1 + d/C\tau_r} \right), \quad (2.31)$$

where the parameters L_{a1} , L_{a2} , and $C\tau_r$ all depend on the photon energy $h\nu$. The optimum silicide layer thickness may then be determined by the solution of the equation $\partial\eta/\partial d = 0$ for d , which gives

$$d_{opt} \approx \sqrt{L_{a2} C\tau_r} - C\tau_r. \quad (2.32)$$

The implications of Fig. 2.10 are not limited solely to the prediction of an exceptionally thin optimum silicide layer. It is also clear from the assorted plots that the maximum in the quantum efficiency as a function of thickness is quite broad, especially at the shorter wavelengths. As an example, Fig. 2.10(a) shows that while the optimum PtSi thickness at $3.07\mu\text{m}$ is approximately 20\AA , no substantial reduction in the efficiency is anticipated as the film width varies from that value until it falls below 10\AA or rises above 40\AA . This observation might help to explain some of the "anomalous" data that has been reported.¹⁹ The lack of an observed drop in the efficiency as film thickness are reduced

from their predicted optimum values at higher photon energies could very well be due in part to the presence of a relatively broad maximum.

It is useful at this point to recapitulate the essential physical insights revealed in this chapter unencumbered by mathematical detail. It has been shown that the photoresponse of thin film PtSi/p-Si Schottky diodes can be described quite accurately by a fairly simple analytical model based on the assumption that hot carrier transport is primarily diffusive. The yield per absorbed photon appears to be determined principally by the mean distance a photoexcited hole travels before colliding with a cold hole and the transmission of the Schottky barrier. High performance photodiodes are characterized by low barrier heights and long scattering lengths. Elastic scattering seems to be relatively unimportant; but any effect due to such processes is expected to be detrimental, in contrast to the findings for thick film devices. In combination with a suitable model for the radiation absorption in the silicide layer, the diffusion formulation also allows the calculation of the optimum PtSi layer thickness at a given incident photon energy. The maximum appears to be quite broad, a fact which could be responsible for some of the unexpected response levels previously observed in certain devices. Each of these observations follows from just the simplest incarnation of the diffusion model. In the next chapter, several extensions to the basic form will be considered which will shed additional light on the photoresponse process.

References for Chapter 2

1. D. Bohm, Quantum Theory (Dover, New York, 1989).
2. J.M. Mooney, Ph. D. thesis, University of Arizona, 1986.
3. J.M. Mooney, "Infrared Optical Absorption of Thin PtSi Films Between 1 and 6 μm ," J. Appl. Phys. 64, 4664 (1988).
4. S.M. Sze, J.L. Moll, T. Sugano, "Range-Energy Relation of Hot Electrons in Gold," Solid-State Electron. 7, 509 (1964).

5. R. Stuart, F. Wooten, W.E. Spicer, "Monte Carlo Calculations Pertaining to the Transport of Hot Electrons in Metals," *Phys. Rev.* 135, A495 (1964).
6. B. Davison, Neutron Transport Theory (Oxford, London, 1958).
7. R. Courant, D. Hilbert, Methods of Mathematical Physics Volume I (Wiley-Interscience, New York, 1953), p. 427.
8. F. Reif, Fundamentals of Statistical and Thermal Physics (McGraw-Hill, New York, 1965), p. 484.
9. O. Bisi, C. Calandra, "Transition Metal Silicides: Aspects of the Chemical Bond and Trends in the Electronic Structure," *J. Phys. C* 14, 5479 (1981).
10. I. Abbati, L. Braicovich, B. De Michelis, O. Bisi, R. Rovetta, "Electronic Structure of compounds at Platinum-Silicon (111) Interface," *Solid-State Comm.* 37, 119 (1981).
11. V.E. Vickers, "Model of Schottky Barrier Hot-Electron-Mode Photodetection," *Appl. Opt.* 10, 2190 (1971).
12. V.L. Dalal, "Simple Model for Internal Photoemission," *J. Appl. Phys.* 42, 2274 (1971).
13. J.M. Mooney, J. Silverman, "The Theory of Hot-Electron Photoemission in Schottky-Barrier IR Detectors," *IEEE Trans. Electron. Dev.* ED-32, 33 (1985).
14. C.R. Crowell, S.M. Sze, "Quantum-Mechanical Reflection of Electrons at Metal-Semiconductor Barriers: Electron Transport in Semiconductor-Metal-Semiconductor Structures," *J. Appl. Phys.* 37, 2683 (1966).
15. S.M. Sze, Physics of Semiconductor Devices, 2nd ed. (Wiley, New York, 1981), p. 850.
16. R.N. Stuart, F. Wooten, W.E. Spicer, "Mean Free Path of Hot Electrons and Holes in Metals," *Phys. Rev. Lett.* 10, 7 (1963).
17. D. Lange, private communication.
18. E.D. Palik, Handbook of Optical Constants of Solids (Academic Press, Orlando, 1985).
19. J. Silverman, P. Pellegrini, J. Comer, A. Golubovic, M. Weeks, J. Mooney, J. Fitzgerald, "Characterization of Thin PtSi/p-Si Schottky Diodes," *Mat. Res. Soc. Symp. Proc.* 54, 515 (1986).

Chapter 3

Extensions to the Diffusion Model

Chapter 2 introduced the diffusion model in its simplest form and demonstrated its ability to provide an excellent description of the available data. However, a number of relevant effects were either glossed over or completely ignored in the development of the solution. While the variation of the photoresponse with the silicide layer thickness was examined in detail, the various energy considerations were often treated in a highly heuristic manner. In the present chapter, a number of extensions to the basic formulation of the model are considered, including the incorporation of the detailed energy dependence of the various parameters used in the model, the addition of hot carrier energy losses due to phonon emission in the silicide layer, and the inclusion of possible hot carrier multiplication at higher photon energies. The analysis of these effects provides additional insight into the photoresponse process beyond that obtained from the initial study.

3.1. Incorporation of Energy Dependent Transport Parameters

In Section 2.2.1, it was assumed that the various transport parameters used in the diffusion model vary only with the energy of the incident radiation rather than the energies of excitation of individual carriers, which allowed the yield to be approximated by

$$Y = \frac{1}{h\nu} \int_{\phi}^{h\nu} Y(E) dE \approx \left(\frac{h\nu - \phi}{h\nu} \right) Y(h\nu) . \quad (3.1)$$

where, as indicated earlier, the density of states near the Fermi is assumed to be constant. However, as noted in that discussion, the parameters C , τ_r (or L_r), and, to some extent, D might be expected to display a significant variation with energy over the range of excitation. D , as will become obvious in the next section, relies equally on the scattering lengths for all collision processes occurring in the silicide film, of which only de-excitation exhibits a strong energy dependence. The approximation of D with a single value for a given photon energy should, therefore, introduce only a small degree of error into the result. On the other hand, it is not at all clear that the same approximation should hold for C and τ_r . It would be a worthwhile exercise, therefore, to examine the changes produced in the simple result of Chapter 2 when the functional dependences of C and τ_r are fully accounted for.

It will prove useful at the outset of this analysis to rephrase some of the results of Chapter 2. In the derivation of the simplified yield expression of Eq. (2.16) from the exact but more complicated energy-dependent summation of Eq. (2.12), the energy approximation indicated in Eq. (3.1) was performed before the reduction of the sum. However, if Eq. (2.15) holds at every energy of excitation, i.e. if

$$\frac{C(E)d}{D(E)} \ll 1 \quad (3.2)$$

for all E , then the order of these two operations may be reversed. In addition, since $C(E) \approx 1/4v_f T(E)$ and $L_r(E) \approx v_f \tau_r(E)$, the product $C\tau_r$ may be stated in terms of the barrier transmission function and the inelastic scattering length, which are more convenient parameters for the present energy analysis. The yield per absorbed photon can then be calculated from the relation

$$Y \approx \frac{1}{hv} \int_0^{hv} \frac{1}{1 + 4d / [T(E)L_r(E)]} dE \quad (3.3)$$

without neglecting the energy content of the parameters.

In Chapter 2, both $T(E)$ and $L_r(E)$ were replaced by their average values over the range of the integral. The next logical step would be to insert the semi-classical escape-cone transmission function that was derived in Eqs. (2.18)–(2.21) and used to calculate the average value of T into Eq. (3.3) while retaining the approximation for L_r . The integral produced in this manner is readily solved to give

$$Y = \frac{(h\nu - \phi)}{h\nu} - 8 \left(\frac{E_f d}{ML_r h\nu} \right) \ln \left(1 + \frac{ML_r (h\nu - \phi)}{8E_f d} \right), \quad (3.4)$$

which, while analytically quite different from Eq. (2.23), produces very similar numerical results as indicated in Fig. 3.1. Although Fig. 3.1 shows only curves for a 20Å diode, a close correspondence between the two formulae is observed over the entire relevant thickness range, which lends credence to the earlier use of average parameter values. Moreover, neither equation can be distinguished as providing a better fit to the available

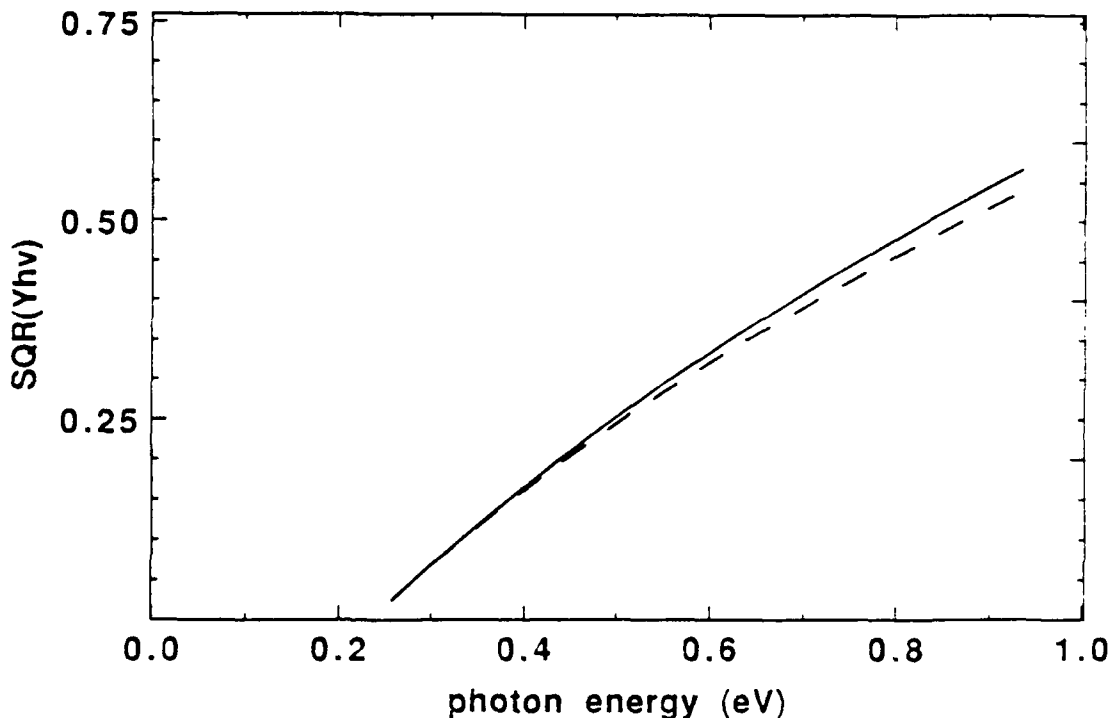


Fig. 3.1. A comparison of the numerical results produced by Eqs. (2.23) (solid line) and (3.4) (dashed line) for a 20Å PtSi/p-Si diode. The same parameter values were employed in both cases: $\phi = 0.235\text{eV}$, $M = 0.4$, $E_f = 8.5\text{eV}$, and $L_r = 8000\text{Å}$.

experimental data when diodes of varying thickness are examined. In light of these observations, the simpler form of Eq. (2.23) seems preferable to the somewhat more exact solution.

While the escape-cone argument should provide an adequate approximation to the actual barrier transmission function, the emission of a hole or an electron over a potential barrier only slightly lower than the particle energy is clearly a quantum mechanical event. The use of a quantum mechanical transmission function, therefore, deserves some study. The lightly doped substrates employed in these devices in combination with the low barrier height should produce an extremely wide potential barrier with little slope, a shape well approximated by the simple step shown in Fig. 3.2. The actual barrier will be a smoothed version of Fig. 3.2, which should display more muted quantum mechanical effects than the abrupt step. The actual transmission function, neglecting morphological considerations, would, therefore, be expected to lie somewhere between the escape-cone

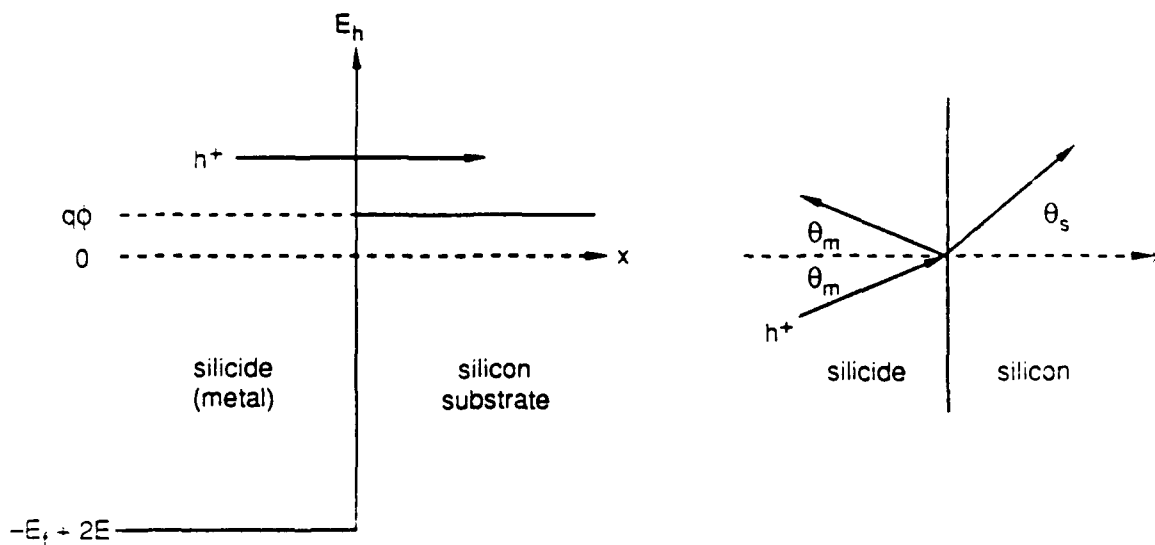


Fig. 3.2. Quantum mechanical step barrier shown from the hole perspective. Among the consequences of this point of view is the energy dependent barrier height.

and quantum mechanical step results. However, the step barrier will give an reasonable idea of the possible consequences of the quantum nature of the emission process while providing a tractable functional form for the energy integration.

The issue of transmission over a step barrier is one of the most basic quantum mechanical problems that exists, and the details of the calculation will be omitted. Two caveats associated with this particular instance that were touched upon already in Sections 2.1 and 2.2.1 bear repeating, however. The effective mass discontinuity at the interface causes a violation of the conservation of probability current and introduces a factor of $1/M$ into the result. In addition, the necessary invocation of conservation of parallel momentum implies specular reflection from the interface, a response that may be at odds with the observed data. With these considerations in mind, the transmission function for an incident hole with wave vector k_m is given by

$$T(k_m) = \left(\frac{1}{M}\right) \frac{4k_m \cos \theta_m k_s \cos \theta_s}{[k_m \cos \theta_m + k_s \cos \theta_s]^2} \quad (3.5)$$

where

$$k_m = \sqrt{\frac{2m_m(E_f - E)}{\hbar^2}} \quad , \quad k_s = \sqrt{\frac{2m_s(E - q\phi)}{\hbar^2}} \quad , \quad \text{and} \quad k_m \sin \theta_m = k_s \sin \theta_s \quad ; \quad (3.6)$$

and the angles are taken with respect to the interface normal as indicated in Fig. 3.2. Eq. (3.6) implies that the quantum mechanical escape-cone described by θ_m will be fairly small for carrier energies less than 1eV, allowing the terms $\sin \theta_m$ and $\cos \theta_m$ to be replaced by θ_m and 1, respectively. If this approximation is employed and θ_s eliminated, Eq. (3.5) becomes

$$T(k_m) = \left(\frac{1}{M}\right) \frac{4k_m \sqrt{k_s^2 - k_m^2 \theta_m^2}}{[k_m + \sqrt{k_s^2 - k_m^2 \theta_m^2}]^2} \quad (3.7)$$

Eq. (3.7) may then be integrated over all allowed angles of incidence to determine the quantum mechanical transmission function for all holes of energy E impinging on the

barrier in a manner similar to that employed in the corresponding semi-classical case illustrated by Eq. (2.20). Within the small angle approximation, the integral may be solved exactly; and, if terms to fourth order in k_s/k_m are retained, a usable solution is reached.

$$\begin{aligned}
 T(E) &= \frac{1}{2\pi} \int_0^{2\pi k_s/k_m} \int_0^0 T(k_m) \theta' d\theta' d\phi' \approx \frac{4}{3M} \left(\frac{k_s}{k_m}\right)^3 \left(1 - \frac{3}{2} \frac{k_s}{k_m}\right) \\
 &\approx \frac{4}{3} M^{1/2} \left(\frac{E - \phi}{E_f}\right)^{3/2} - 2M \left(\frac{E - \phi}{E_f}\right)^2 ; E \gg h\nu
 \end{aligned} \tag{3.8}$$

Like the semi-classical transmission function, the quantum mechanical version may be employed in two ways, both in the calculation of an average value for a given photon energy for use in Eq. (3.1) and in the more rigorous integration indicated by Eq. (3.3). For the present, the energy dependence of the inelastic scattering length will continue to be neglected. The fully integrated method fails to yield an exact result in this case; however, a good approximation to the integral may be obtained. As discovered in the semi-classical analysis, the two methods yield very different analytical solutions but almost identical numerical results. A fit of either model to the Mooney data with L_r as the single adjustable parameter, however, requires L_r to decrease steadily with increasing photon energy. Since L_r was assumed to be constant, an obvious contradiction exists. It would seem that the combination of a quantum mechanical transmission function with a constant inelastic scattering length does not provide a proper description of the physics of the situation. Despite its simplicity, the basic form of the model is definitely superior.

Although largely ignored to this point, the inelastic scattering length L_r may also exhibit a strong energy dependence and merits discussion. Theoretical consideration of the interaction between excited carriers and the Fermi surface in ideal metals leads to an inverse-squared variation of L_r with the energy of excitation above the Fermi level, i.e.

$$L_r(E) \approx L_{r0} \left(\frac{E_0}{E} \right)^2, \quad (3.9)$$

where L_{r0} represents the scattering length at some reference energy E_0 .^{1,2} Such a variation, if actually present, would certainly be significant even over the limited range of photon energies normally encountered. Moreover, Eq. (3.9) indicates that changes in L_r will occur in opposition to those in T , so that although the barrier transmission probability shrinks as the energy of excitation decreases, the average carrier lifetime increases markedly. This effect would tend to moderate changes in the $T(E)L_r(E)$ term in Eq. (3.3) and could help to explain the success of the earlier use of average parameter values.

While the use of Eq. (3.9) in conjunction with the transmission functions studied earlier is clearly desirable, it would be worthwhile to first examine its ability to describe the energy characteristics of the problem by itself. Just as L_r was held constant while changes in T were investigated, so may T be fixed while the effect of the energy content of L_r alone on the yield is evaluated. Like the transmission functions, the expression for L_r was used to calculate an average value for a given photon energy as well as for direct insertion into Eq. (3.3). Once again, the two approaches were found to generate solutions that differed in appearance but were virtually identical numerically. However, as in the case of the quantum mechanical transmission function, a fit of either form to Mooney's data utilizing $TL_{r0}E_0^2$ as the fitting parameter failed to produce a consistent result. Eq. (3.9) alone apparently cannot account for the entire energy character of the photoyield.

The most rigorous treatment of the energy characteristics of the problem would obviously be given through the incorporation of both Eq. (3.9) and either of the two transmission functions. This approach would be expected to generate a solution at least as accurate as that of the basic model, and an inferior result would imply a definite deficiency in the understanding of the underlying physics present. While the outcome will not prove to be distinguishably better than that of the simpler form, it will be gratifying to see that it is not distinguishably worse.

When the energy dependent scattering length and the quantum mechanical transmission function are inserted into Eq. (3.3), the integral is unfortunately discovered to possess neither an exact solution nor any obvious approximation which might lead to one. A numerical solution could be attempted, but part of the initial intent of this work was the development of a reasonably simple analytical solution. On the other hand, the average value of each parameter for E between ϕ and $h\nu$ is easy to extract; and, based on the close correlation between the fully integrated and averaged results for energy variations in a single parameter, it seems likely that the average value method would give a fairly accurate result. This technique leads to a yield per absorbed photon of the form

$$Y = \left(\frac{h\nu - \phi}{h\nu} \right) \left(1 + \frac{4d}{L_{r0} \frac{E_0^2}{h\nu\phi} \left[\frac{8}{15} M^{1/2} \left(\frac{h\nu - \phi}{E_f} \right)^{3/2} - \frac{2}{3} M \left(\frac{h\nu - \phi}{E_f} \right)^2 \right]} \right)^{-1} \quad (3.10)$$

A fit of Eq. (3.10) to the Mooney data does, in fact, indicate that the value of $L_{r0}E_0^2$ is reasonably constant and approximately equal to $2200 \text{ \AA} \cdot \text{eV}^2$, which corresponds to an inelastic scattering length of about $22\,000 \text{ \AA}$ at $4 \mu\text{m}$. This is much longer than the value predicted by the simpler form of the model, but is not unlike that obtained from the Mooney model in the limit of no phonon scattering, as indicated in Chapter 2. Mooney, however, assumed a constant value for L_r over the span $\phi \leq h\nu \leq 1 \text{ eV}$, while here L_r will vary from $39\,000$ down to 2200 \AA over the same interval. A comparison of Eq. (3.10) with the basic model of Eq. (2.23) is shown in Fig. 3.3 for the case of a 20 \AA diode. While the curvature differs somewhat between the two fits, neither can claim to represent a superior approximation to the data. Although contrasting assumptions underlie the two forms, both generate very similar results.

The combination of the semi-classical transmission function with the energy dependent scattering length produces an equally interesting yet very different outcome. In this case, the integral in Eq. (3.3) does, in fact, have an exact solution. However, since

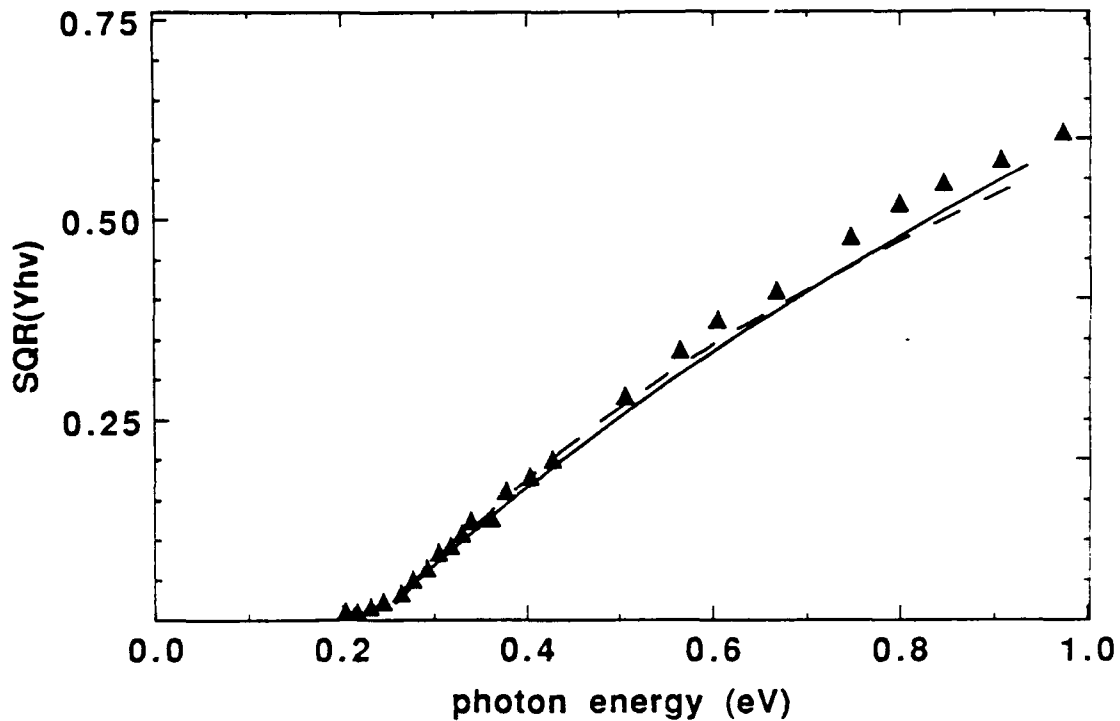


Fig. 3.3. A comparison of the basic diffusion model (solid line) with the model incorporating both a quantum mechanical barrier transmission function and an inverse squared inelastic scattering length (dashed line) along with Mooney's data for a 20Å PtSi/p-Si diode.

the average value method again provides an excellent alternative, this stirring tribute to algebra will not be reproduced here. Actually, the use of average values is somewhat less successful in this case, but the agreement is still remarkable. The yield in this instance may then be expressed by

$$Y = \left(\frac{h\nu - \phi}{h\nu} \right) \left\{ 1 + \frac{4d}{L_{r0} \frac{E_0^2}{h\nu\phi} \left[\frac{1}{4} M \left(\frac{h\nu - \phi}{E_f} \right) \right]} \right\}^{-1} \quad (3.11)$$

When Eq. (3.11) is optimized with respect to the Mooney data, the fitting parameter $L_{r0}E_0^2$ appears to stabilize at approximately 610 Å-eV² in the 3–5μm range (680 Å-eV² for the exact result), but begins to rise with decreasing wavelength below 3μm. While this behavior might seem to invalidate Eq. (3.11), another possible explanation exists.

One of the fundamental postulates upon which the discussion of the diffusion model has been based is the assumption that the collision of a hot carrier with a cold one results in the de-excitation of the hot carrier. However, when the energy of the incident photons approaches a magnitude twice the barrier height or greater, an equal division of the hot carrier energy between the two carriers involved can produce two carriers with sufficient energy for emission. An unequal division should still leave one hot carrier, although at a somewhat lower energy than the original. The consequences of multiplication will be contemplated in more detail later in this chapter, but for the present it will suffice to say that within the current framework of the diffusion formulation, the onset of multiplication would in all probability be indistinguishable from an apparent increase in the hot carrier inelastic scattering length. In the case of the PtSi/*p*-Si Schottky diode, multiplication would be expected to start at photon energies between 0.4 and 0.5eV, or 2.5 to 3 μ m. This concurs closely with the findings of Eq. (3.11).

It may be concluded from this analysis that while the energy dependence of the various parameters utilized by the diffusion model may be incorporated into the solution with a high degree of rigor, the basic form of the model provides as good a description of the available experimental data as the more complex versions. Excellent fits are obtained with the assumption of either a semi-classical barrier transmission function and a constant inelastic scattering length or the combination of a quantum mechanical transmission function and an inverse squared scattering length. In addition, the use of the semi-classical transmission function in conjunction with the inverse squared scattering length may point out the onset of multiplication when compared with the experimental data, an occurrence which will be examined in greater detail in Section 3.3.

3.2. Phonon Energy Losses

Despite the careful treatment of the energy dependence of the diffusion model parameters presented in Section 3.1, one major shortcoming in the consideration of the

energy distribution of the excited carrier distribution remains. So far, it has been assumed that each group of holes photoexcited into a small energy interval can be discussed separately within the diffusion formulation and the results for all the different groups averaged together to obtain the overall device photoyield for a given photon energy. In reality, hot carriers undergo a continuous energy loss process due to optical phonon emission, which couples these individual groups together and limits the extent to which they can be considered separately. The success of the various forms of the diffusion model examined to this point in describing the experimental data and the condition $Cd/D \ll 1$ from which they follow imply that the inclusion of phonon effects should not radically alter the previous results; however, it would be of interest to perform a more rigorous analysis to indicate what role these effects actually do play in the determination of the photoyield. While the implicit assumption in diffusion theory of either a monoenergetic carrier distribution or transport parameters that are independent of energy does not allow for collision processes which modify the energy of a hot carrier without resulting in its capture, the formulation may be extended to describe the variation of the carrier distribution with energy as well as position and time. The standard diffusion equation, i.e. Eq. (2.1), may be derived from basic transport theory, which incorporates such effects quite readily and, therefore, provides a means for the rigorous development of an extended diffusion model. The formula resulting from the analysis will prove to be quite intuitive; however, the full derivation will clearly show the assumptions underlying the result and, hence, its inherent limitations. In addition, the role of all other forms of bulk scattering in the diffusion formulation will be elucidated by this process.

The derivation of the extended diffusion equation closely parallels that of neutron age theory and will progress in a manner very similar to that used by Marshak to generate the age approximation.³ However, two important distinctions exist between the two problems which simplify the analysis in this case. In the slowing down of neutrons, hot neutrons lose varying amounts of energy through collisions with essentially stationary

nuclei and are deflected through angles determined by the amount of energy loss. On the other hand, the excited holes in a Schottky diode lose discrete amounts of energy through the emission of phonons, a process which redirects the carrier momentum in a random fashion. The collision integral which arises in the transport theory is greatly simplified under these conditions.

The time-dependent transport equation governing the behavior of the excited hole distribution in the silicide film is given by

$$\frac{\partial p(\mathbf{r}, \Omega, E, t)}{\partial t} + \mathbf{v} \cdot \nabla p(\mathbf{r}, \Omega, E, t) = -\frac{vp(\mathbf{r}, \Omega, E, t)}{L(E)} + \int \frac{vp(\mathbf{r}, \Omega', E + \Delta E_p, t)}{L_p(E + \Delta E_p)} \frac{d\Omega'}{4\pi} + \int \sum_{i=1}^{\infty} \frac{vp(\mathbf{r}, \Omega', E, t)}{L_i(E)} \frac{d\Omega'}{4\pi} + \frac{1}{4\pi} P_0(\mathbf{r}) \delta_{E, E_0} \delta(t) \quad (3.12)$$

In Eq. (3.12), $p(\mathbf{r}, \Omega, E, t) d\mathbf{r} d\Omega dE$ denotes the number of hot holes with spatial coordinates between \mathbf{r} and $\mathbf{r} + d\mathbf{r}$, unit vector in the direction of the hole momentum between Ω and $\Omega + d\Omega$, and energy between E and $E + dE$ at time t . In addition, \mathbf{v} represents the hot hole velocity, ΔE_p is the energy of an optical phonon mode, E_0 is the initial energy of excitation of the distribution, $P_0(\mathbf{r})$ describes the initial concentration of hot holes as a function of position, L_p is the mean optical phonon scattering length, L_i represents the mean scattering length for some arbitrary lossless scattering event such as a grain boundary or small k acoustic phonon collision, and $L(E)$ is the total mean free path for all scattering events, i.e.

$$\frac{1}{L(E)} = \frac{1}{L_r(E)} + \frac{1}{L_p(E)} + \sum_{i=1}^{\infty} \frac{1}{L_i(E)} \quad (3.13)$$

Eq. (3.12) resembles Eq. (1) of Marshak, but has been altered in accordance with hole transport. In addition, the carrier energy E has been retained in favor of the lethargy parameter used in age theory. The left-hand side of the equation describes the time rate of

change of the distribution function due to carrier translation in the direction Ω . The first term on the right-hand side accounts for carriers displaced from the element $p(\mathbf{r},\Omega,E,t)d\mathbf{r}d\Omega dE$ through all forms of scattering, both elastic and inelastic; while the two integrals represent holes scattered into $p(\mathbf{r},\Omega,E,t)d\mathbf{r}d\Omega dE$ through phonon emission and any essentially lossless scattering processes. All elastic and quasi-elastic (i.e. optical phonon) scattering process are assumed to be isotropic, with a probability of deflection in any direction given by $d\Omega/4\pi$. Although Raman scattering studies show two prominent optical phonon modes in thin PtSi films at 10 and 17 meV,⁴ only a single mode has been employed here for simplicity. Also, the hot carrier velocity has been assumed to be constant for an energy change of ΔE_p . The final term on the right is the source term, which in this case explicitly incorporates the initial state of the system into the transport equation.

In its original form, the diffusion equation produced a solution for a carriers with a certain energy of excitation E which was then averaged over the full range of possible energies for a given incident photon energy to generate the final expression for the total photoyield. In contrast, the transport equation describes the concentration of hot carriers at a given energy E that were initially excited to a specific energy E_0 . Calculation of the total photoyield in this case will require a summation of the yield at energy E over all possible final states for holes initially excited to E_0 before the average over all possible values of E_0 is performed. This does not present any serious complications. One interesting consequence of this particular grouping, however, is the fact that the energies E will be discrete and can be described by the expression $E = E_0 - n \Delta E_p$, where n represents the number of phonon collisions undergone. Subsequently, E will be replaced by the integer variable $n = n(E_0)$, where the dependence on E_0 will, in general, be suppressed.

The full range of flexibility offered by Eq. (3.12) clearly will not be required in this instance. For a one-dimensional diffusion model, only the x spatial coordinate is of

interest. This fact allows the replacement of the terms \mathbf{r} and $\mathbf{v} \cdot \nabla$ by x and $v\mu\partial/\partial x$, respectively, where μ is the cosine of the angle between Ω and the x axis. Because of the rotational symmetry which exists with respect to the x axis in one dimension, specification of μ completely describes the direction of carrier momentum, which then permits the replacement of the Ω dependence of the concentration by a dependence on μ . Furthermore, in accordance with age theory, it will be assumed that the carrier distribution is nearly isotropic, so that $p(x, \mu, E, t)$ is well approximated by the first two terms of its expansion in spherical harmonics, i.e.

$$p(x, \mu, n, t) \approx \frac{1}{4\pi} [p_0(x, n, t) + 3\mu p_1(x, n, t)] \quad (3.14)$$

If both the zero and first moments of Eq. (3.12) are taken after the insertion of Eq. (3.14), a system of two equations for the functions p_0 and p_1 results:

$$\begin{aligned} \frac{\partial p_0(x, n, t)}{\partial t} = & -v \frac{\partial p_1(x, n, t)}{\partial x} - v p_0(x, n, t) \left[\frac{1}{L_r(n)} + \frac{1}{L_p(n)} \right] + \\ & + \frac{v p_0(x, n-1, t)}{L_p(n-1)} H(n-1) + P_0(x) \delta_{n,0} \delta(t) \quad , \end{aligned} \quad (3.15)$$

$$\frac{\partial p_1(x, n, t)}{\partial t} = -\frac{v}{3} \frac{\partial p_0(x, n, t)}{\partial x} - \frac{v p_1(x, n, t)}{L(n)} \quad , \quad (3.16)$$

where H in Eq. (3.15) represents the Heaviside step function. An intriguing observation arises from scrutiny of Eqs. (3.15) and (3.16). The assumption of isotropic scattering implies that the collision integrals of Eq. (3.12) possess only zero order moments, in contrast to the age theory derivation. A bulk imperfection which exhibits directionally dependent scattering might invalidate this result; however, the random occurrence of such imperfections within the silicide films makes a preferential scattering direction unlikely.

An analytical reduction of the two simultaneous equations does not exist. The age theory approximation circumvents this annoying detail by neglecting the time dependence of p_1 . With this simplification, Eqs. (3.15) and (3.16) are easily combined to give a single equation for p_0 :

$$\begin{aligned} \frac{\partial p_0(x,n,t)}{\partial t} = & \frac{vL(n)}{3} \frac{\partial^2 p_0(x,n,t)}{\partial x^2} - vp_0(x,n,t) \left[\frac{1}{L_r(n)} + \frac{1}{L_p(n)} \right] + \\ & + \frac{vp_0(x,n-1,t)}{L_p(n-1)} H(n-1) + P_0(x) \delta_{n,0} \delta(t) . \end{aligned} \quad (3.17)$$

The strong resemblance that this expression bears to the diffusion equation may be further enhanced by the parameter assignments

$$D(n) = \frac{vL(n)}{3} , \quad \frac{1}{\tau(n)} = \frac{1}{\tau_r(n)} + \frac{1}{\tau_p(n)} , \quad \frac{1}{\tau_r(n)} = \frac{v}{L_r(n)} , \quad \frac{1}{\tau_p(n)} = \frac{v}{L_p(n)} ; \quad (3.18)$$

which allow Eq. (3.17) to be re-written in the form

$$\begin{aligned} \frac{\partial p_0(x,n,t)}{\partial t} = & D(n) \frac{\partial^2 p_0(x,n,t)}{\partial x^2} - \frac{p_0(x,n,t)}{\tau(n)} + \\ & + \frac{p_0(x,n-1,t)}{\tau_p(n-1)} H(n-1) + P_0(x) \delta_{n,0} \delta(t) . \end{aligned} \quad (3.19)$$

With the exception of the final two terms, the second of which simply incorporates the initial condition for the problem directly into the differential (actually differential-difference) equation, Eq. (3.19) is identical in form to the standard diffusion equation given by Eq. (2.1) and may justifiably claim to represent an extended form of the diffusion model. The form of the extended equation, as alluded to earlier, is quite intuitive. The additional term describes the scattering of phonons into an element of phase space as a relaxation process characterized by a mean phonon scattering time τ_p . While this result probably could have been obtained through judicious guessing, the insight gained into the underlying assumptions, especially those regarding the angular character of both the scattering events and the carrier distribution, is well worth the effort. Moreover, it is instructive to observe how the presence of lossless scattering mechanisms not considered in detail here is reflected through the parameter D .

Before a solution to Eq. (3.19) is attempted, it is necessary to determine the boundary conditions for the extended model. The net flux of carriers in the x direction in any increment of position and energy will be given, in general, by

$$\text{Flux(in } +x) = \int v p(x, \mu, n, t) \mu d\mu \quad , \quad (3.20)$$

where the range of the integral extends over all μ . If the partial expansion of Eq. (3.14) is substituted for p , the vanishing of the p_0 term reduces the right-hand side of the expression to $v p_1(x, n, t)$. With the definition of D and the earlier assumption that the time dependence of p_1 may be neglected in Eq. (3.16), the flux becomes

$$\text{Flux(in } +x) = -D(n) \frac{\partial p_0(x, n, t)}{\partial x} \quad . \quad (3.21)$$

This permits the boundary condition at $x = 0$ to be stated as

$$D(n) \frac{\partial p_0(0, n, t)}{\partial x} = 0 \quad , \quad (3.22)$$

which is virtually identical to the corresponding condition for the simple model contained in Eq. (2.2). The boundary condition at the silicide/silicon interface, on the other hand, implied that the flux out of the film was proportional to the concentration of hot carriers at the barrier, independent of their angles of incidence. If Eq. (3.14) is integrated over all μ in order to obtain the directionally independent concentration, only the p_0 term remains and the boundary condition becomes

$$-D(n) \frac{\partial p_0(d, n, t)}{\partial x} = C(n) p_0(d, n, t) \quad . \quad (3.23)$$

Actually, the previous analyses of various forms of C clearly allow a directionally dependent form of C to be defined, which might suggest that Cp be integrated over μ rather than p alone. However, separation of the two angular dependences will prove to be necessary for an analytical solution and is more in keeping with the original intent of the model. The photocurrent flux at a given time in a specified energy increment may then be

described by $Cp_0(d,n,t)$. The p_1 term has apparently dropped out of the analysis at this point; however, the assumptions made earlier which involved it must be checked when p_0 has been determined.

Eqs. (3.19), (3.22), and (3.23) together represent the extended form of the diffusion model. An analytical solution may be obtained for this problem just as in the simpler case, but an additional approximation is required. The dependence of the parameters C and D on n in Eq. (3.23) prevents the separation of the variable x , a fact which essentially nullifies any chance to obtain a solution in closed form. It will, therefore, be necessary to assume at the outset that C and D vary only with the incident photon energy and not with the individual energies of excitation, an approximation utilized early in the development of the basic model but relaxed later on. As discussed in Section 3.1 and further illustrated through the derivation in this section, this assumption is well justified in the case of D but is much less so with regard to C . However, the analysis of Section 3.1 showed close correspondence between the numerical results generated by the original model for rigorous and approximate inclusion of the energy dependence of C , so the average value of C will be used here despite the fact that a larger disparity might be expected in this instance.

A combination of the method of finite Fourier transforms⁵ and inductive reasoning will be employed to solve the extended model. To begin, it will be assumed that the concentration $p_0(x,n,t)$ may be written as a series expansion of the form

$$p_0(x,n,t) = \sum_{j=1}^{\infty} M_j(x)N_j(n,t) \quad , \quad (3.24)$$

where the M_j 's are the normalized set of eigenfunctions of the problem

$$D \frac{\partial^2 M_j(x)}{\partial x^2} = -k_j M_j(x)$$

$$D \frac{\partial M_j(0)}{\partial x} = 0 \quad , \quad -D \frac{\partial M_j(d)}{\partial x} = CM_j(d) \quad . \quad (3.25)$$

Eq. (3.25) is quite similar to the original diffusion problem covered in Section 2.2.1, and the eigenfunctions may be obtained from Eqs. (2.4)–(2.11) in the form

$$M_j(x) = \left\{ \frac{2[(C/D)^2 + k_j/D]}{[(C/D)^2 + k_j/D]d + C/D} \right\}^{1/2} \cos(\sqrt{k_j/D}x) ,$$

$$\sqrt{k_j/D} \tan(\sqrt{k_j/D}d) = C/D . \quad (3.26)$$

If both sides of Eq. (3.19) are multiplied by M_j and integrated over the interval $x \in [0, d]$, the orthonormality of the M_j 's leaves the following equation in n and t only:

$$\frac{\partial N_j(n, t)}{\partial t} = - \left[k_j + \frac{1}{\tau(n)} \right] N_j(n, t) + \frac{1}{\tau_p(n)} N_j(n-1, t) H(n-1) +$$

$$+ \delta_{n,0} \delta(t) \int_0^d P_0(x') M_j(x') dx' , \quad (3.27)$$

which may be solved inductively despite the fact that it is not fully separable. Although there exists an answer to Eq. (3.27) as it stands, the result is greatly simplified if τ and τ_p vary slowly with energy and may be assumed to be constant for a given photon energy just like C and D . While a small change in the energy and, hence, the velocity of a hole above the Fermi energy produces a substantial shift in motion relative to carriers at the Fermi surface, only a slight alteration in the motion relative to the lattice occurs. For this reason, the mean phonon scattering time (or length) will probably not display the strong energy dependence expected of the mean hot hole-cold hole scattering time (or length). Moreover, if optical phonon scattering is more probable than inelastic scattering, then τ will be determined mainly by the phonon scattering time and will also vary slowly with energy. This assumption will, therefore, be employed.

When $n = 0$, the $n - 1$ term drops out of Eq. (3.27) while the initial condition remains, which leaves

$$\frac{\partial N_j(0,t)}{\partial t} = \delta(t) \int_0^d P_0(x') M_j(x') dx' - \left[k_j + \frac{1}{\tau} \right] N_j(0,t) \quad (3.28)$$

It is obvious from the theory of generalized functions that Eq. (3.28) represents the generalized derivative of the function $N_j(0,t)$, where the second term on the right gives the derivative for all $t \geq 0$ and the coefficient of the delta function gives the jump discontinuity in $N_j(0,t)$ at $t = 0$.⁵ $N_j(0,t)$ can then be determined by inspection to be

$$N_j(0,t) = \exp\left[-\left(k_j + \frac{1}{\tau}\right)t\right] H(t) \int_0^d P_0(x') M_j(x') dx' \quad (3.29)$$

On the other hand, for $n \geq 1$ the initial condition vanishes from Eq. (3.28) and the phonon term stays. For $n = 1$, this produces

$$\frac{\partial N_j(1,t)}{\partial t} + \left[k_j + \frac{1}{\tau} \right] N_j(1,t) = \frac{1}{\tau_p} N_j(0,t) \quad (3.30)$$

which, together with Eq. (3.29) and the fact that $N_j(1,t)$ is zero for $t \leq 0$, is readily solved to give

$$N_j(1,t) = \left(\frac{t}{\tau_p}\right) \exp\left[-\left(k_j + \frac{1}{\tau}\right)t\right] H(t) \int_0^d P_0(x') M_j(x') dx' \quad (3.31)$$

If successive iterations of this process are performed for increasing values of n , it becomes readily apparent that the general solution for arbitrary n is given by

$$N_j(n,t) = \frac{1}{n!} \left(\frac{t}{\tau_p}\right)^n \exp\left[-\left(k_j + \frac{1}{\tau}\right)t\right] H(t) \int_0^d P_0(x') M_j(x') dx' \quad (3.32)$$

As required, $N_j(n,t)$ has a value of zero at $t = 0$ except when $n = 0$, in which case it jumps to the value given by the integral. Given the expressions for M_j and N_j , p_0 is ascertained from Eq. (3.24) to be

$$p_0(x, n, t) = 2 \sum_{j=1}^{\infty} \frac{[(C/D)^2 + k_j/D]}{[(C/D)^2 + k_j/D]d + C/D} \int_0^d P_0(x') \cos(\sqrt{k_j/D} x') dx' \\ \times \cos(\sqrt{k_j/D} x) \left(\frac{1}{n!}\right) \left(\frac{t}{\tau_p}\right)^n \exp[-(1/\tau + k_j)t] H(t) . \quad (3.33)$$

With the exception of the terms in n , this is identical to the concentration found for the simple model in Chapter 2.

Before the analysis continues, however, some of the assumptions employed in the derivation of the extended model should be verified using this expression for p_0 . Most of these assumptions were based on certain relationships between p_0 and p_1 , so it will be necessary to first determine p_1 from Eq. (3.33). If the time derivative of p_1 is neglected as it was in the derivation, then p_1 can be found from Eq. (3.16). If the Fourier expansions for the two are compared term by term, it is discovered that

$$p_{1j}(x, n, t) = -\frac{L(n)}{3} \frac{\partial p_{0j}(x, n, t)}{\partial x} = -\frac{L(n)}{3} \left(\frac{k_j}{D}\right)^{1/2} \tan(\sqrt{k_j/D} x) p_{0j}(x, n, t) . \quad (3.34)$$

The initial approximation made concerning the carrier distribution allowed the concentration to be represented by the first two terms in its expansion in spherical harmonics, as indicated in Eq. (3.14). This requires that $p_1 \ll p_0$, which is not necessarily true at every x due to the presence of the tangent function in Eq. (3.34). However, experience with the basic model indicates that the $j = 1$ term will probably dominate the result, and in this case the argument of the tangent function will be quite small. In addition, at $x = d$ where the validity is most critical, Eq. (3.26) implies that $p_{1j} = -L/3(C/D)p_{0j} = (C/v)p_{0j}$, which should be much less than p_{0j} . The elimination of the time derivative of p_1 itself needs to be justified as well. Eq. (3.34) implies that

$$\left| \frac{-(L/v) \partial p_{1j} / \partial t}{p_{1j}} \right| = \left(\frac{L}{v} \right) \left| \frac{n}{t} - \left(k_j + \frac{1}{\tau} \right) + \alpha t \right| . \quad (3.35)$$

Unless $t = 0$ or $j \gg 1$, the value of the right-hand side of Eq. (3.35) should be less than or approximately equal to one whenever $p_{1j}(x, n, t)$ is significant in size, and it should

approach one only when the sign of the time derivative term is such that the magnitude of p_1 will be overestimated in its absence. The neglect of the time derivative of p_1 in Eq. (3.16), therefore, seems to be reasonable.

With these concerns addressed, the photoyield may now be determined from Eq. (3.33). The yield per absorbed photon is calculated by integrating the flux over the barrier $Cp_0(d, n, t)$ over all time $t \geq 0$, summing over all possible n for a given initial energy of excitation E_0 , integrating over E_0 in the range $\phi \leq E_0 \leq h\nu$, and normalizing to the total number of excited carriers at $t = 0$. These operations will commute with the summation over j in Eq. (3.33) so that only those factors which depend on n or t will be affected. The remaining parts of the equation will be temporarily ignored. After a suitable change of variable, the time integral is transformed into the familiar gamma function and the result

$$\int_0^{\infty} \frac{1}{n!} \left(\frac{t}{\tau_p}\right)^n \exp[-(1/\tau_r + k_j)t] H(t) dt = \left(\frac{1}{k_j + 1/\tau_r}\right) \left[\frac{1}{\tau_p(k_j + 1/\tau_r)}\right]^n \quad (3.36)$$

follows immediately. Since $1/[\tau_p(k_j + 1/\tau_r)] < 1$, Eq. (3.36) describes a simple geometric series in n , the summation of which is readily expressed in closed form. For a given E_0 , n can vary from zero up to the largest integer not exceeding $(E_0 - \phi)/\Delta E_p$ for carriers able to escape. If the maximum value of n is assumed to be $(E_0 - \phi)/\Delta E_p$, then the summation of Eq. (3.36) over n gives

$$\sum_{n=0}^{(E_0 - \phi)/\Delta E_p} \left(\frac{1}{k_j + 1/\tau_r}\right) \left[\frac{1}{\tau_p(k_j + 1/\tau_r)}\right]^n = \left(\frac{1}{k_j + 1/\tau_r}\right) \left\{1 - \left[\frac{1}{\tau_p(k_j + 1/\tau_r)}\right]^{(E_0 - \phi)/\Delta E_p + 1}\right\}. \quad (3.37)$$

This expression is readily integrated over E_0 . If, as in Chapter 2, it is assumed that the density of states is relatively constant within $h\nu$ of the Fermi level, then the total photoyield per absorbed photon may be expressed as

$$Y = \frac{2C^2\tau_h}{D} \sum_{j=1}^{\infty} \left(\frac{h\nu - \phi}{h\nu} - \frac{\Delta E_p}{h\nu} \left\{ \frac{1 - [\tau_p(k_j + 1/\tau)]^{-(h\nu - \phi)/\Delta E_p}}{\tau_p(k_j + 1/\tau) \ln[\tau_p(k_j + 1/\tau)]} \right\} \right) \left\{ \frac{1}{[(C/D)^2 + k_j/D]d + C/D} \right\} \\ \times \left[\frac{1}{k_j \tau_h + 1} \right] \left\{ \frac{\sqrt{k_j/D}}{\sin(\sqrt{k_j/D}d)} \int_0^d \frac{P_0(x')}{P_{0\varepsilon}} \cos(\sqrt{k_j/D}x') dx' \right\}, \quad (3.38)$$

where $P_{0\varepsilon}$ is the total number of carriers excited into a given increment of energy space and the transcendental condition in Eq. (3.26) has been judiciously applied.

If Eq. (3.38) is compared with the yield of the basic model described by Eq. (2.14), the two appear to be essentially identical except for the term in ΔE_p . The main impact of the inclusion of energy losses due to optical phonon emission seems to be an increase in the apparent Schottky barrier height by an amount given by this new term. This would explain the systematic discrepancy between the electrical and optical barrier heights that has been observed.⁶ As with the original model, the condition $Cd/D \ll 1$ permits substantial simplification of the complicated yield expression. In this limit, which Section 2.2.1 indicates will almost certainly be reached, the summation is accurately represented by the $j=1$ term only and $(k_1/D)^{1/2}d$ is extremely small, so that the yield can be reduced to

$$Y \approx \left(\frac{h\nu - \phi - \Delta E_p f(d, h\nu, \tau_p/\tau_h, C\tau_h, \Delta E_p, \phi)}{h\nu} \right) \frac{1}{1 + d/(C\tau_h)}, \quad (3.39)$$

where

$$f = \frac{1 - [1 + \tau_p/\tau_h(1 + C\tau_h/d)]^{-(h\nu - \phi)/\Delta E_p}}{[1 + \tau_p/\tau_h(1 + C\tau_h/d)] \ln[1 + \tau_p/\tau_h(1 + C\tau_h/d)]}. \quad (3.40)$$

Eq. (3.39) has been written to further the interpretation that the apparent barrier height increases in the presence of phonon losses. Examination of Eqs. (3.39) and (3.40) shows that even when phonon losses are counted, the diffusion constant D still vanishes from the simplified yield expression, so that fully elastic scattering processes appear to have a negligible effect on the photoyield.

The extended model of Eqs. (3.39)–(3.40) produces a good fit to the Mooney data with proper adjustment of the two fitting parameters τ_p/τ_h and $C\tau_h$. One caveat must be observed, however. With the assumption that the discrepancy between the electrically and optically measured barrier heights results from the phonon loss effect mentioned above, it becomes necessary to use the electrically determined average barrier height of $\phi = 0.20$ eV for consistency. Unfortunately, while the model incorporating phonon losses fits the data at least as well as the other versions of the model considered so far, it can not be distinguished as providing a superior description. In addition, a unique parameter assignment cannot be made based on the data fitting procedure. Independent measurements of the various lifetimes mentioned have not been made due to the extreme difficulty involved in observing such brief phenomena, so it is not possible at this time to resolve this predicament. However, an assessment of the impact of various levels of phonon scattering on the yield can certainly be performed, and the results of such a study are shown in Fig. 3.4. Since the purpose of this exercise is to observe the effect of phonon scattering on the yield rather than to accurately fit data, the optically determined barrier height has been used to generate these curves. In addition, a semi-classical barrier transmission and constant scattering lengths have been assumed. From the figure, it is clear that the predicted yield is virtually identical to that of the basic model as long as $\tau_p/\tau_h \geq 1$, i.e. as long as hole-hole scattering is more probable than optical phonon emission. As τ_p/τ_h falls below 1 and phonon scattering becomes stronger, all other parameters remaining constant, the yield at each photon energy also begins to drop. Moreover, for τ_p/τ_h on the order of 0.01, the shape of the photoyield curve changes radically, so much that an error could be made when extrapolating the curve in order to ascertain the barrier height. It is abundantly clear from this that the incorporation of phonon losses can drastically affect the yield if optical phonon scattering is highly probable relative to de-excitation, a result that was not predicted by the original form of the model. Although only the simplest consistent set of parameter energy dependences was employed to

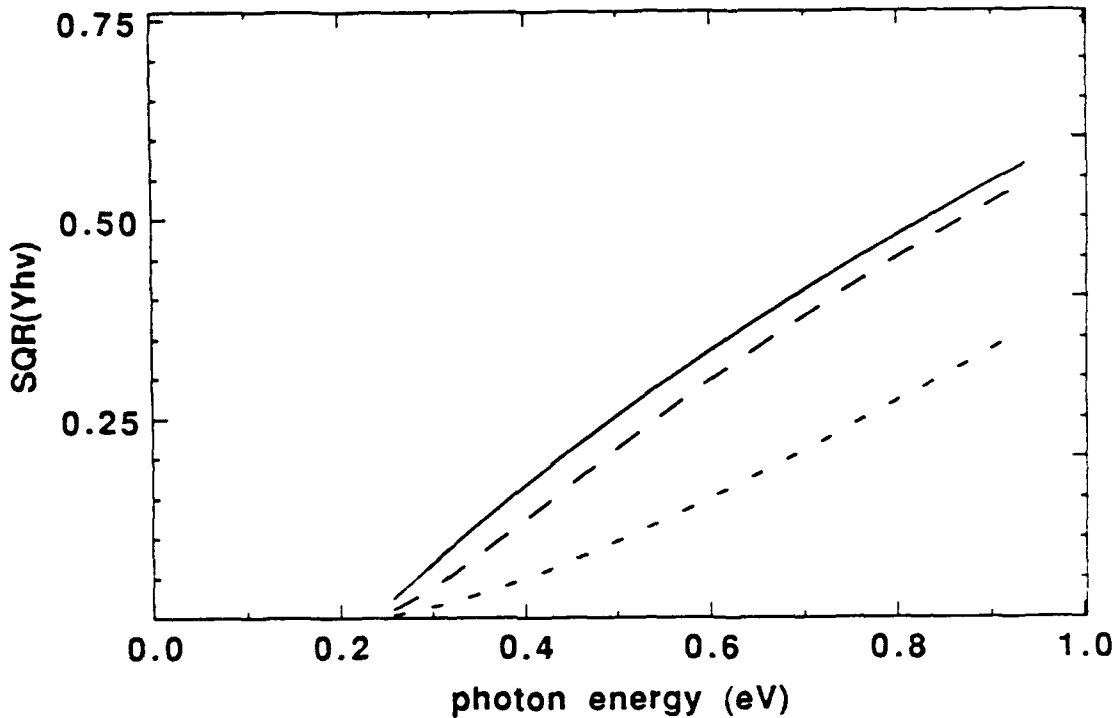


Fig. 3.4. The effect of various levels of optical phonon scattering on the photoyield. The solid curve describes the yield for $\tau_p/\tau_h \geq 1$, the long dashed curve for $\tau_p/\tau_h \approx 0.1$, and the short dashed curve for $\tau_p/\tau_h \approx 0.01$. The optically determined barrier height and a 20Å PtSi layer have been used in all cases.

calculate these curves, the consequences for the more rigorous parameter assignments investigated in Section 3.1 will be similar.

3.3. Carrier Multiplication at Higher Photon Energies

One final phenomenon which deserves some thought is the possible multiplication of hot carriers at higher photon energies. It has been assumed to this point that the collision of a hot hole with a cold hole at or below the equilibrium Fermi level results in the de-excitation of the hot hole and eliminates its chances for escape. This should indeed occur if the hot carrier loses roughly half of its energy to the cold carrier and the incident photon energy only moderately exceeds the barrier height. However, if the photon energy and, hence, the maximum possible energy of excitation approach or surpass an amount double

the height of the barrier, the possibility exists that a collision of this type could produce two carriers with sufficient energy to escape rather than none. Even if the event fails to produce multiplication, at least one of the carriers should still be left with enough energy for emission. This effect is not considered in any of the standard photoyield models mentioned in Chapter 2. For PtSi/*p*-Si diodes operating in the 3-5 μ m band or IrSi/*p*-Si diodes at 8-12 μ m, the photon energies lie sufficiently close to the respective barrier heights that multiplication may be justifiably neglected; however, the majority of the "anomalous" yield measurements reported have been taken at higher energies⁷ and could conceivably be explained by this mechanism. A brief theoretical analysis of the effect within the diffusion formulation could, therefore, prove useful.

The general transport formalism introduced in Section 3.2 to incorporate energy losses due to phonon emission provides a means for the addition of multiplication to the diffusion model. If phonon scattering is ignored, the analysis becomes almost identical to the derivation of the age theory mentioned earlier. Unfortunately, the approximations which lead to the relatively simple age theory equation are not particularly accurate when the hot carriers scatter off particles of the same mass, and lose even more validity when the carriers under consideration span only a narrow range of energies. Without these assumptions, the result obtained for the present problem is a horrendous mess. Therefore, a less rigorous but much more tractable analysis will be undertaken which will utilize the results of the phonon loss exercise completed earlier.

To simplify matters, it will be assumed that the scattering of a hot carrier by a cold or stationary carrier leaves each with half of the original energy of excitation and a random direction of motion. This clearly represents an approximation, for while phonon emission results in a quantized energy loss and randomizes the momentum direction of a hot carrier, scattering of a moving particle by a stationary particle produces a variable energy loss with a scattering angle determined by the amount of loss. Nonetheless, the approximation seems reasonable and should give an indication of the effect of multiplication on the yield.

Therefore, for incident photon energies less than twice the barrier height, hot hole-cold hole collisions will be assumed to cause thermalization of the hot hole; while for photon energies between 2ϕ and 4ϕ , collisions involving carriers with energies of excitation in this range will be assumed to produce two hot carriers each with half the incident carrier energy. Since the data only cover photon energies up to about 4ϕ , only a single multiplication event will be considered. In addition, phonon losses will be neglected in this case.

Since the diffusion equations utilized so far have been linear in the carrier concentration $p(x,E,t)$, the total concentration in the presence of multiplication can be determined by the superposition of the additional amount due to this process alone on top of the result calculated from the basic model of Chapter 2. With the guidance of Eq. (3.19) for the phonon loss problem and the approximations indicated above, the equation governing the additional concentration may be determined intuitively as

$$\frac{\partial p_m(x,E,t)}{\partial t} = D \frac{\partial^2 p_m(x,E,t)}{\partial x^2} - \frac{p_m(x,E,t)}{\tau_n} + \frac{4}{\tau_h} p(x,2E,t) H(h\nu - 2E) ,$$

$$D \frac{\partial p_m(d,E,t)}{\partial x} = 0 , \quad -D \frac{\partial p_m(d,E,t)}{\partial x} = C p_m(d,E,t) . \quad (3.41)$$

The factor of four in the multiplication term comes from the production of two carriers as a result of each collision combined with a two-fold compression of energy space. The quantity $p(x,2E,t)$ is just the concentration at $2E$ calculated with the original model neglecting multiplication. Note that the variable n introduced in the phonon exercise has been scrapped, since the possibility of only a single multiplication event precludes the need for a double summation/integration over the energy variable. The initial condition for Eq. (3.41) in the absence of the multiplication term is zero.

The solution of Eq. (3.41) proceeds in a manner identical to that employed to solve the phonon loss problem. An answer of the form

$$p_m(x, E, t) = \sum_{j=1}^{\infty} M_j(x) N_j(E, t) \quad , \quad (3.42)$$

is assumed, where the M_j 's form a set of normalized eigenfunctions given by Eq. (3.26) which satisfy the boundary conditions given in Eq. (3.41). If the inner product of the diffusion equation of Eq. (3.41) and the eigenfunction M_j is taken, the orthonormality of the eigenfunctions leads to the following equation for N_j :

$$\begin{aligned} \frac{\partial N_j(E, t)}{\partial t} + \left(k_j + \frac{1}{\tau_h}\right) N_j(E, t) &= \frac{4}{\tau_h} N_j(2E, t) H(h\nu - 2E) \\ &= \frac{4}{\tau_h} \exp\left[-\left(k_j + \frac{1}{\tau_h}\right)t\right] H(h\nu - 2E) \int_0^d P_0(x') M_j(x') dx' \quad , \quad (3.43) \end{aligned}$$

where $N_j(2E, t)$ can be obtained from the results of Sections 2.2.1 and 3.2. Eq. (3.43) is essentially identical to Eq. (3.30), and slight modification of the answer provided by Eq. (3.31) yields

$$N_j(E, t) = \frac{4t}{\tau_h} \exp\left[-\left(k_j + \frac{1}{\tau_h}\right)t\right] H(h\nu - 2E) \int_0^d P_0(x') M_j(x') dx' \quad . \quad (3.44)$$

The added concentration due to multiplication may then be expressed as

$$\begin{aligned} p_m(x, E, t) &= \sum_{j=1}^{\infty} \frac{8[(C/D)^2 + k_j/D]}{[(C/D)^2 + k_j/D]d + C/D} \int_0^d P_0(x') \cos(\sqrt{k_j/D}x') dx' \\ &\quad \times \cos(\sqrt{k_j/D}x) \left(\frac{t}{\tau_h}\right) \exp\left[-(1/\tau_h + k_j)t\right] H(h\nu - 2E) \quad , \\ \sqrt{k_j/D} \tan(\sqrt{k_j/D}d) &= C/D \quad . \quad (3.45) \end{aligned}$$

The extra yield expected can then be calculated by integrating over all time $t \geq 0$, integrating over energy from 0 to $h\nu/2$, and normalizing to the total number of excited holes at $t = 0$. If, as in previous incarnations of the model, both the density of states and their optical absorption cross-section are assumed to be constant within $h\nu$ of the Fermi:

level, the yield due to multiplication per absorbed photon for a given photon energy becomes

$$Y_m = \frac{4C^2\tau_h}{D} \left(\frac{h\nu - 2\phi}{h\nu} \right) H(h\nu - 2\phi) \sum_{j=1}^{\infty} \left\{ \frac{1}{[(C/D)^2 + k_j/D]d + C/D} \right\} \left(\frac{1}{k_j\tau_h + 1} \right)^2 \times \frac{\sqrt{k_j/D}}{\sin(\sqrt{k_j/D}d)} \int_0^d \frac{P_0(x')}{P_{0E}} \cos(\sqrt{k_j/D}x') dx' \quad (3.46)$$

where P_{0E} represents the total number of carriers initially excited into a given increment of energy space. In accordance with all prior analyses, Eq. (3.46) can be greatly simplified in the event that $Cd/D \ll 1$, so that Y_m will be well estimated by the formula

$$Y_m \approx \left(\frac{h\nu - 2\phi}{h\nu} \right) \frac{2d/(C\tau_h)}{[1 + d/(C\tau_h)]^2} H(h\nu - 2\phi) \quad (3.47)$$

In contrast to the normal photoyield expressions, Eq. (3.47) does not have its maximum value in the limit as the silicide thickness d goes to zero, but, instead, is largest when $d = C\tau_h$. This phenomenon may be explained by noting that as d falls below $C\tau_h$, the likelihood that excited holes will escape before suffering a collision with another hole becomes significant. Since multiplication cannot occur without such scattering events, the yield due to carriers which exist as a consequence of multiplication will decrease. Given the formula for Y_m , the total photoyield per absorbed photon can be determined from the expression

$$Y \approx \left(\frac{h\nu - \phi}{h\nu} \right) \frac{1}{1 + d/(C\tau_h)} + \left(\frac{h\nu - 2\phi}{h\nu} \right) \frac{2d/(C\tau_h)}{[1 + d/(C\tau_h)]^2} H(h\nu - 2\phi) \quad (3.48)$$

It should be noted that the incorporation of multiplication has added no new parameters to the formulation, unlike the addition of phonon losses.

Only one of the various combinations of transmission function and hole-hole scattering length energy formulae considered earlier in Section 3.1 in conjunction with the basic form of the model appeared to admit the possibility of multiplication, specifically the

pairing of the semi-classical transmission function with the inverse-squared scattering length. Since the other combinations either provided a consistent fit to the data as they stood or clearly missed the ballpark, there is no sense in considering them in the presence of multiplication. For the case of interest, Eq. (3.11) implies that $C\tau_h$ is given by

$$C\tau_h = \frac{1}{16} L_{r0} M \frac{E_0^2}{hv\phi} \left(\frac{hv - \phi}{E_f} \right). \quad (3.49)$$

For $M = 0.4$, $\phi = 0.235\text{eV}$, and $E_f = 8.5\text{eV}$, a fit of the basic model to the Mooney data indicated that the quantity $L_{r0}E_0^2$ appears to be fairly constant with an average value of about $610 \text{ eV}\cdot\text{\AA}^2$ for photon energies up to 2ϕ , beyond which the value required rises monotonically with the photon energy. If Eq. (3.49) is substituted into Eq. (3.48) using this value of $L_{r0}E_0^2$, a good fit to the data should be obtained without any further parameter adjustment. The results of this procedure, shown in Fig. 3.5 for diodes with 10 and 20\AA PtSi layers, are rather remarkable. As indicated in both cases but particularly in that of the 10\AA diode, the slope of the predicted Fowler curve appears to match that of the data extremely well—amazingly well considering the somewhat heuristic treatment of the hole-hole scattering event. A kink in the data originally thought to be a possible artifact of the measurement appears instead, based on this analysis, to signal the onset of multiplication. It should again be emphasized that no new parameters or parameter optimization were employed to generate Fig. 3.5. Unlike the various forms of the model considered earlier, this version might indeed be considered to provide a discernibly superior fit to the available data over the entire 0.2 to 1.0eV range. However, as mentioned at the beginning of this section, operation in the standard 3 to 5\mu m window occurs below the threshold of multiplication, where Eq.(3.48) reverts to the basic form of the model.

It still remains to be seen if multiplication could account for some of the anomalous yield measurements alluded to earlier. The measurements in question were performed on

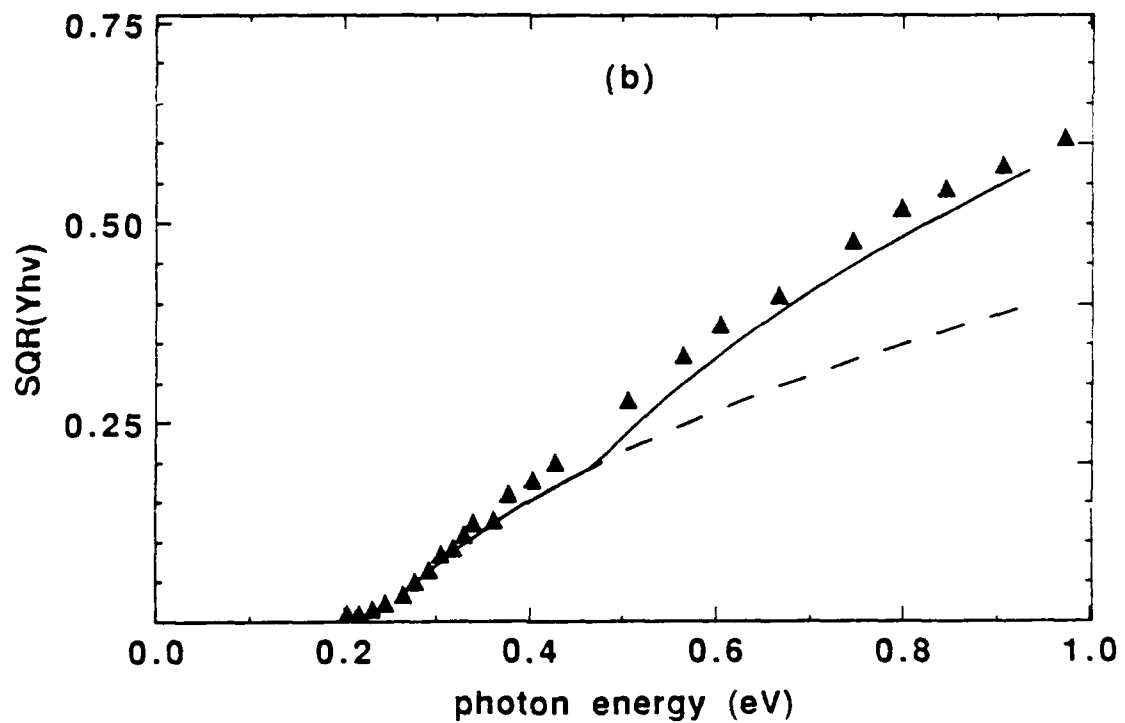
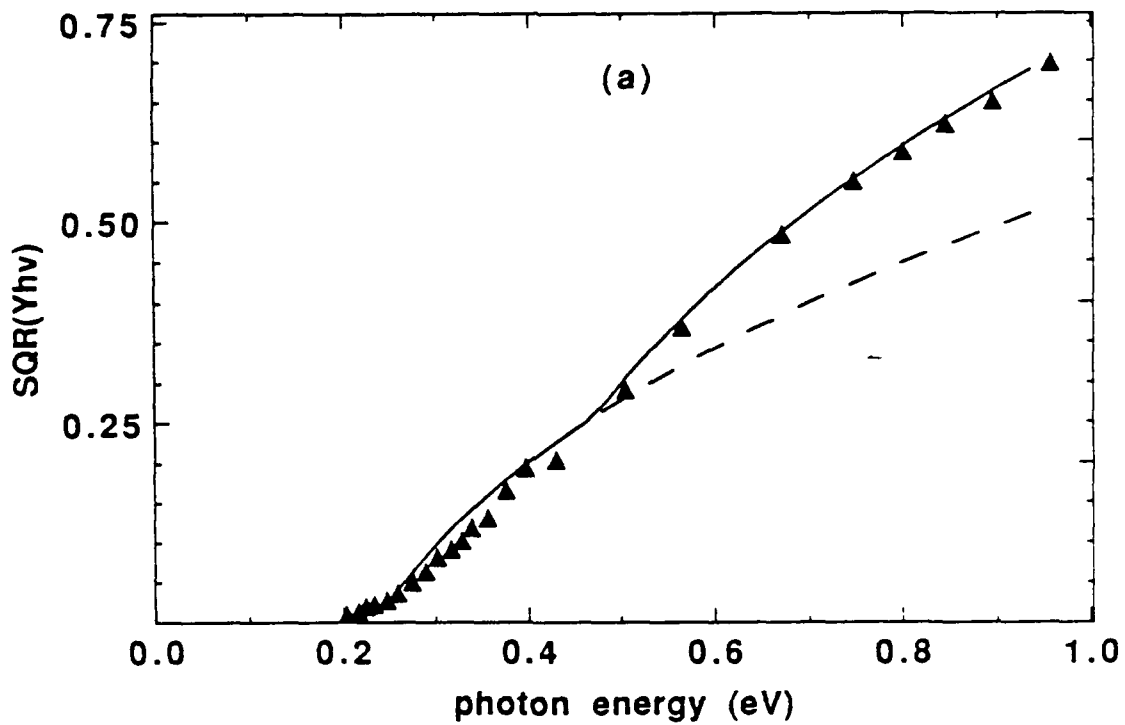


Fig. 3.5. A comparison of the photoyield predicted by the diffusion model incorporating hot carrier multiplication (solid line) with the data obtained by Mooney (triangles) for (a) 10Å and (b) 20Å PtSi/p-Si Schottky photodiodes. The dashed lines represent the diffusion model with the semi-classical transmission function and an inverse-squared hole-hole scattering length but no multiplication.

extremely thin, i.e. less than 10\AA , diodes at wavelengths shorter than $2\mu\text{m}$. The fact that the added yield stemming from multiplication peaks for $d = C\tau_h$ rather than zero bodes poorly for an explanation founded on this effect. Fig. 3.6 shows a comparison of the predictions of Eq. (3.48) with those of the basic diffusion model of Chapter 2 for a 5\AA PtSi/*p*-Si diode. While the yield at higher photon energies with multiplication taken into account does exceed that projected by the basic model, the increase in yield is fairly minor

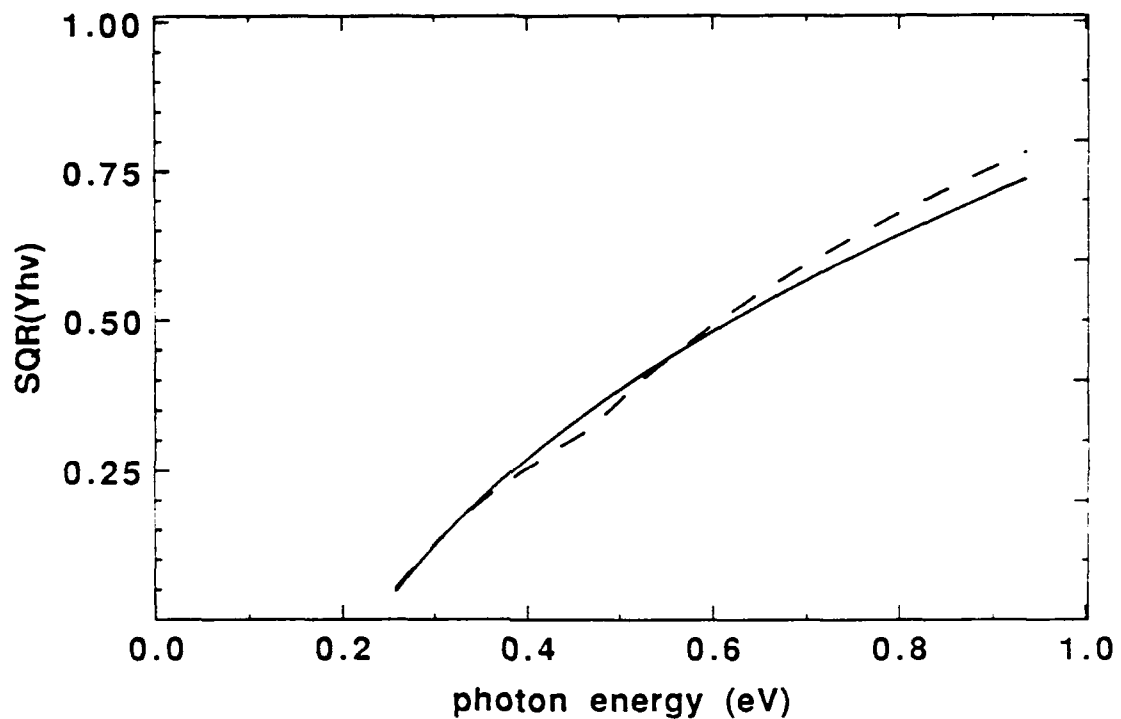


Fig. 3.6. A comparison of the predictions of the diffusion model incorporating multiplication (dashed line) with those of the basic model of Chapter 2 (solid line) for a 5\AA PtSi/*p*-Si diode.

and certainly does not approach the level reported in the literature. The resolution of the paradox does not appear possible through the invocation of multiplication.

This essentially completes the theoretical analysis of Schottky diode photoresponse. In this chapter, several enhancements to the basic diffusion model presented in Chapter 2 have been studied. A more detailed analysis of the inelastic scattering length and the barrier transmission parameters used by the model revealed that the substitution of

presumably more accurate quantum mechanical expressions for the semi-classical ones originally employed did not discernibly improve the fit to the available data on PtSi/*p*-Si diodes. On the other hand, the combination of a semi-classical transmission function and a quantum mechanical scattering length suggested the presence of a mechanism not previously taken into account, i.e. the onset of hot carrier multiplication at higher photon energies. The extension of the diffusion formulation to incorporate multiplication significantly enhanced the match between the predicted photoyield and the experimental measurements on the thinnest diodes and provided an explanation for some of the nuances in the curvature of the data. Another modification of the basic formulation permitted a study of the effect of energy losses by hot holes due to the emission of optical phonons. The results of the calculation indicated that a high probability for the occurrence of these events would produce a variable increase in the apparent optical barrier height and a corresponding reduction in the photoyield. Neither multiplication nor phonon losses have ever been included in analytical models of Schottky barrier photoresponse before. Ultimately, however, the perceived limitations on silicide-silicon Schottky photodiode performance remained unchanged from those discovered in Chapter 2. Low Schottky barrier heights and the minimization of all forms of bulk scattering appear to constitute the primary requirements for the production of high efficiency devices.

References for Chapter 3

1. J.J. Quinn, "Range of Excited Electrons in Metals," *Phys. Rev.* 126, 1453 (1962).
2. D. Pines, P. Nozieres, The Theory of Quantum Liquids, Vol. I (Benjamin, New York, 1966), pp. 61-63.
3. R.E. Marshak, "Theory of the Slowing Down of Neutrons by Elastic Collision with Atomic Nuclei," *Revs. Mod. Phys.* 19, 185 (1947).
4. J.C. Tsang, Y. Yokota, R. Matz, G. Rubloff, "Raman Spectroscopy of PtSi Formation at the Pt/Si(100) Interface," *Appl. Phys. Lett.* 44, 430 (1984).

5. E. Zauderer, Partial Differential Equations of Applied Mathematics (Wiley, New York, 1983).
6. J.M. Mooney, Ph. D. thesis, University of Arizona, 1986.
7. J. Silverman, P. Pellegrini, J. Comer, A. Golubovic, M. Weeks, J. Mooney, J. Fitzgerald, "Characterization of Thin PtSi/p-Si Schottky Diodes," Mat. Res. Soc. Symp. Proc. 54, 515 (1986).

Chapter 4

Characterization of PtSi/p-Si Schottky Barrier Diodes

Chapters 2 and 3 identified the major device and material parameters which limit the efficiency of silicide-silicon Schottky photodetectors operating in the infrared spectral regime. Both the barrier height and the probability of optical phonon emission must be minimized and the barrier transmission and hot hole lifetime maximized for optimum detector performance. In this chapter, the potential for favorable modification of these characteristics through variations in the processing methods used during PtSi/p-Si diode fabrication will be discussed. Early analysis of diodes fabricated at the Rome Air Development Center (RADC), an example of which was shown in Fig. 2.2, demonstrated that a much higher level of silicide film undulation was present than anticipated. Kinks in the film could heighten both the local interfacial electric field and the associated barrier transmission, while the extreme geometry could affect the assorted scattering parameters in a positive manner. The possibility of controlling the extent of this phenomenon raised hopes of improving the photodetector performance. In the present analysis, the effects of process alterations on both the microstructure and the internal photoresponse of the devices will be considered in detail. The study will actually be expanded to include silicide layers too thick for practical use as photodetectors but suitable for Schottky contacts in integrated circuits in order to determine the changes in the process-induced phenomena with increasing PtSi thickness. In addition, a study of the more fundamental interaction that occurs between platinum and silicon at room temperature will also be

presented which will introduce some of the experimental techniques used throughout this work.

4.1. Experimental Considerations

Silicide Schottky detectors are normally fabricated via the deposition of the metallic component and a subsequent anneal of approximately one hour at a temperature below the lowest binary eutectic. PtSi films are normally formed at temperatures of approximately 350°C, while the IrSi layers of interest at longer wavelengths are typically grown at somewhat higher temperatures in the neighborhood of 500°C. If both the deposition and the anneal take place *in situ* under sufficiently high vacuum, silicidation progresses in two steps.^{1,2,3} In the initial stage, platinum is the dominant diffusing species,⁴ a fact which causes the apparent snowplowing of impurities away from the original metal-silicon interface toward the free surface as the bi-metal silicide phase Pt₂Si is formed.^{2,5,6} The stable monosilicide grows at a slower rate as silicon diffuses from the substrate into the silicide layer, producing a PtSi film approximately twice the thickness of the platinum film originally deposited. The growth sequence can, however, be altered if the substrate surface has been oxidized or if a sufficiently high oxygen partial pressure is present during either the deposition or anneal.^{1,3} Platinum reacts neither with oxygen nor SiO₂, and the presence of either can block the diffusion of the metal. Oxygen pressures as low as 10⁻⁸ Torr have been observed to affect the growth of moderately thick films, while 10⁻⁶ Torr levels are potent enough to completely disrupt the progression of the phase fronts. Films of moderate thickness grown in the presence of either oxygen or a slightly oxidized substrate show a high degree of roughness and poor crystallinity relative to those fabricated under clean conditions.^{3,7} The films are polycrystalline and non-epitaxial in all cases, as PtSi is not lattice matched to silicon.

With the exception of the devices produced at RADAC, all the diodes mentioned in this work were fabricated using the e-beam evaporation system described by Abelson.⁸

The unit is ion pumped, and can maintain an annealing pressure of approximately 2×10^{-8} Torr with the aid of a titanium sublimator operating in conjunction with a liquid nitrogen cooled cryopanel. To reach this pressure, the system must be baked under vacuum at 100°C for several hours after samples are loaded. For this work, however, a bake-out was only performed every four loading cycles, so that 2×10^{-8} Torr represented the base rather than the operating pressure. The system pressure can rise to as much as 3×10^{-7} Torr during metal evaporation under these conditions, but is normally about 1×10^{-7} Torr during the annealing stage. Substrate heating is accomplished using a rapid thermal annealing (RTA) unit with a hole cut in the bottom which allows metal deposition at elevated temperatures. Substrate temperatures are measured using a K-type thermocouple attached to a one inch square piece of silicon wafer with a small amount of Sauereisen thermal cement. The silicon square sits on the back side of the object wafer in the evaporation chamber in reasonably good thermal contact; however, it is necessary to calibrate the temperature measurements with a test wafer to which a C-type thermocouple has been e-beam welded.⁹ Separate calibrations were performed for each silicide thickness employed, since the addition of the metal is expected to increase the thermal absorption of the wafer. The calibrated substrate temperature readings are expected to be accurate to $\pm 2^\circ\text{C}$. Samples fabricated for microstructural evaluation received blanket evaporations covering a 1.5 inch diameter area in the center of the 3 inch wafers used, while diodes intended for photoresponse measurements were delineated using a shadow mask during evaporation. To obtain shadow masks which could remain in contact with the object wafers during the annealing stage without either contaminating the samples or drastically affecting their thermal absorption, patterns were cut through a set of silicon wafers by Applied Fusion in San Leandro, CA, using a laser cutting technique. The masks were subsequently coated with LPCVD oxide to prevent their silicidation and unwanted adhesion to the object wafers. The masks provide 0.5 and 0.75mm diameter I-V/C-V measurement dots, 2.5x2.5mm (0.5mm corner radius) internal photoemission

samples, and a number of relatively large and presumably very leaky areas which can be used as substrate contacts. Some of the masks also incorporate van der Pauw measurement pads as well. Only "bare" diodes were made, i.e. no guard rings, optical cavity structures, or optical coatings of any sort were added to any of the diodes; since the goal of the study was to compare relative performance of diodes formed by the different processing techniques rather than to optimize the performance for a given set of processing conditions.

Microstructural characterization of the various samples was accomplished through a combination of Transmission Electron Microscopy (TEM) and Auger Sputter Profiling (ASP). TEM sample preparation and analysis were performed by Ki Bum Kim, presently of Philips Research Labs, in a manner which has been described in the literature.¹⁰ While TEM was heavily utilized early in this study, it was discovered that nearly all of the necessary information could be obtained from the examination of Auger profiles. The Auger analysis of a sample consumes much less time than a comparable TEM evaluation, so the Auger technique was employed almost exclusively for most of the later work. Auger profiles were generated with a Varian Auger Spectrometry System interfaced to a Hewlett-Packard 300 series computer and multiprogramming unit. This spectrometer utilizes a single pass cylindrical mirror analyzer with an integral electron gun and records differential Auger spectra. In all cases, the electron gun was operated at an accelerating voltage of 5 keV with a total beam current of 2 μ A rastered over an area 450–500 μ m on a side. The fairly low beam flux was chosen to minimize beam heating of the samples under analysis, particularly those samples which had not been annealed. The system has been modified to allow differential pumping during the sputtering process with a Balzers turbomolecular pump capable of maintaining a base system pressure of 2×10^{-9} Torr. Differential pumping of the ion source allows sputtering at low inert gas pressures with no significant degradation of the vacuum environment over time. For films up to 120 \AA in thickness, sample sputtering was accomplished using a 1 keV xenon ion beam operated at

a current density of about $2.4 \mu\text{A}\cdot\text{cm}^{-2}$, while for thicker films the beam density was raised to about $9.4 \mu\text{A}\cdot\text{cm}^{-2}$. The former flux sputters PtSi at a rate of $5.5\text{--}8.5\text{\AA}/\text{min}$, while the latter etches at a rate of about $18\text{--}20\text{\AA}/\text{min}$.

Internal photoresponse measurements were performed with the aid of an optical measurement system similar to that described by Taubenblatt¹¹ but modified for use in the mid-infrared. Radiation is produced by an Oriel SiC "global" source, the light from which passes through a Kratos monochromator utilizing a diffraction grating optimized for use with 3 to $7\mu\text{m}$ wavelength radiation. One of several long pass filters is placed at the exit slit of the monochromator to remove the higher order harmonics from the transmitted beam. A pair of CaF_2 lenses focuses the beam onto a MgF_2 coated mirror, which deflects the beam downward through a second pair of lenses and a sapphire window into an evacuated MMR Technologies LTMP-2 low temperature measurement system capable of achieving sample cooling down to approximately 76K . The samples are mounted such that they are illuminated from the front, i.e. silicide, side. Due to the apparent adsorption of residual gases onto the sample surface when cooled even at a vacuum of only a few mTorr, the LTMP vacuum "chamber" was modified to accommodate a 1.5 inch diameter pumping line to which a 2.75 inch Conflat flange was affixed. A Varian $30\text{L}/\text{sec}$ ion pump provides background pressures well below the mTorr range. The monochromatic light beam is chopped, which allow the diode response to be measured using a lock-in amplifier at greatly reduced background levels relative to the DC case. This arrangement generates the relative voltage responsivity of the diode under test, which tends to minimize the effects of the substrate and substrate contact resistances particular to the test structure on the results. The absolute voltage responsivity differs from the quantum efficiency discussed in the preceding chapters by the dynamic resistance of the diode in question. The diode response must be normalized to the total output of the optical system, which is measured using a Dexter Research Center thermopile with a KRS-5 window monitored by a Keithley Instruments nanovoltmeter. Monochromator control and data logging tasks are

handled by a Macintosh II computer through a G.W. Instruments I/O board designed for the Macintosh Nubus system.

4.2. Room Temperature Interaction Between Pt and Si

As a prelude to the investigation of the effects of assorted processing variations on PtSi film formation, it is useful to examine the various interfacial reactions which occur at room temperature between platinum and silicon when different substrate cleaning methods are employed. It has been observed that when a thin film of platinum is evaporated onto a room temperature silicon wafer cleaned by a standard wet chemical procedure in which a dilute hydrofluoric acid dip constitutes the final step, disordered intermixing occurs at the interface which leads to the formation of an amorphous silicon-rich silicide layer approximately 30Å thick, along with scattered grains of crystalline Pt₂Si.¹⁰ During the course of this work, it was discovered that the extent of intermixing exhibits a strong dependence on the substrate cleaning technique used prior to the platinum evaporation. The Auger profiles shown in Fig. 4.1 provide a striking example of the importance of the surface preparation. The effect appears to be independent of the amount of deposited platinum; therefore, the results for samples with rather thick platinum layers are shown since the profiles for the thicker films are better resolved than those of the thinner ones. To produce the samples in Fig. 4.1, *n*-type silicon wafers with a resistivity of 5-10 Ω-cm were first subjected to a 10 minute "piranha etch" in heated 4:1 H₂SO₄:H₂O₂ followed by the "Stanford reverse-RCA clean" (RRCA'), which consists of 10 minutes in heated 5:1:1 H₂O:HCl:H₂O₂, 30 seconds in 50:1 H₂O:HF, and 10 minutes in heated 5:1:1 H₂O:NH₄OH:H₂O₂. Each step is followed by a 5 minute rinse in deionized (DI) water, and the wafers are blown dry after the final step using a filtered nitrogen gas flow at 25 psi. This procedure is known to leave a thin, i.e. 10-20Å, native oxide layer on the silicon surface.^{12,13} The sample in Fig. 4.1(a) received an additional 30 second dip in 50:1 H₂O:HF with no subsequent rinse in order to remove this native oxide.^{13,14} A

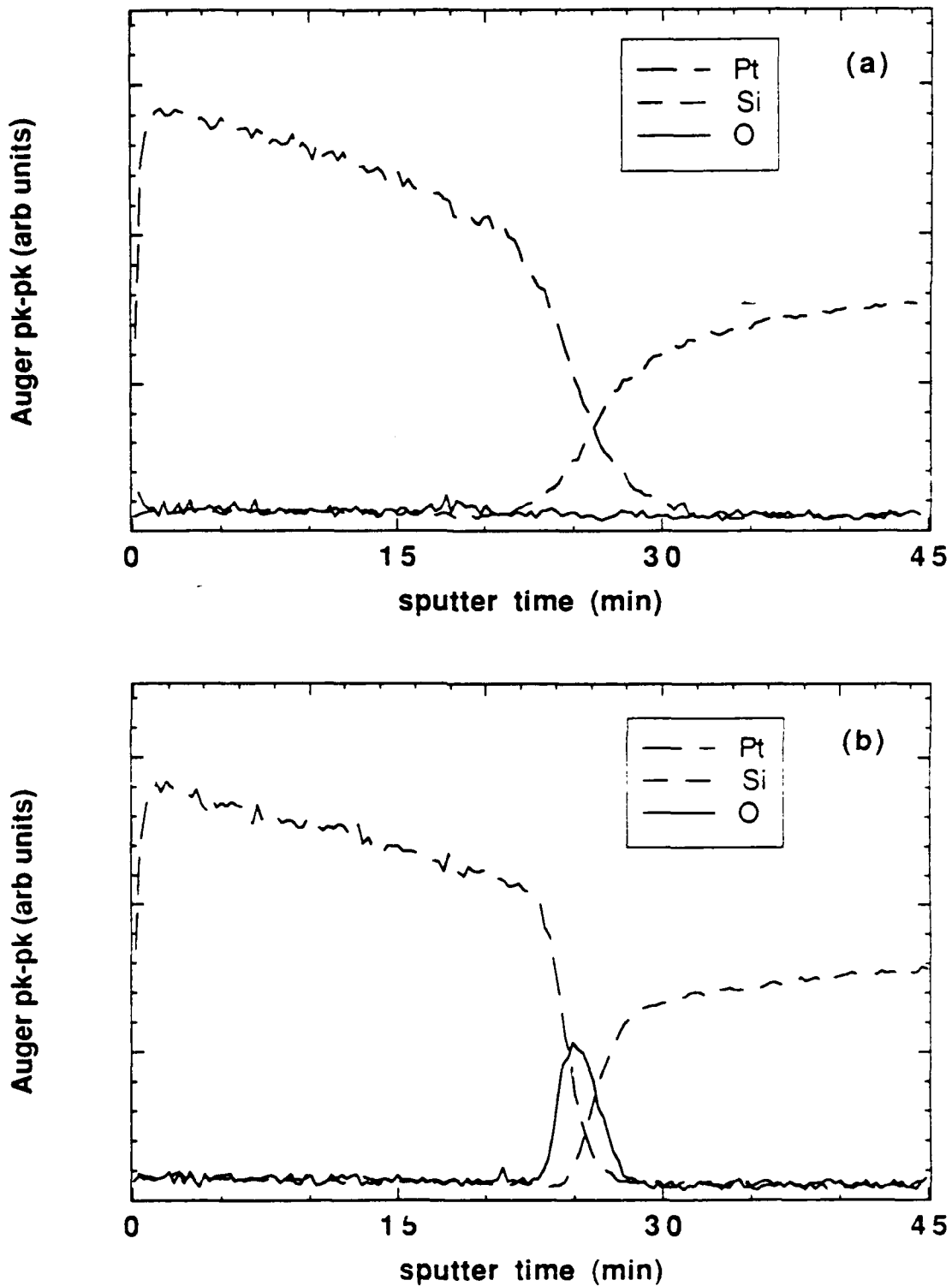


Fig. 4.1. Auger sputter profiles of two 300Å platinum films evaporated onto silicon substrates at room temperature. In (a), the substrate was cleaned using the RRCA' clean followed by a 30 second dip in 50:1 HF:H₂O, while in (b) the HF dip was omitted. An ion beam flux of 6μA-cm⁻² gave a platinum sputtering rate of about 12Å/min.

comparison of the two sets of profiles reveals that while the HF cleaned wafer shows evidence of the interfacial reaction mentioned earlier, the sample with the native oxide exhibits no such behavior. The oxide layer remains intact and prevents any intermixing between the platinum and the underlying substrate, as indicated by the relatively sharp cut-off and cut-on of the platinum and silicon profiles. Some interfacial broadening is always observed in Auger profiles, since a number of effects including the ion mixing and surface roughening induced by the sputtering process and the finite escape depth of the Auger electrons from the sample limit the ultimate depth resolution of the Auger technique. The sputtering time which elapses while the platinum signal drops from 90 to 10% of its initial strength at the platinum-oxide interface in Fig. 4.1(b), when multiplied by the calculated platinum sputtering rate, suggests the presence of 30–35Å of “instrumental broadening” in the Auger data at a depth of 300Å. The HF cleaned sample, on the other hand, displays a noticeably broader interface with some smoothing of the profiles and a lack of any contaminants. The platinum profile in this case yields a total interface width of 70–80Å, including both “instrumental” and chemical effects. The thickness of the oxide in Fig. 4.1(b) can be inferred by extracting the sputtering rate and relative signal intensity from the sputter profile of a thin gate oxide of known thickness analyzed under the same conditions. This procedure suggests that an amount of oxygen equivalent to that contained in 12–14Å of SiO₂ is present in the layer, which agrees very well with the reported data. It is quite clear from this exercise that the substrate surface preparation can have a marked effect on the room temperature kinetics of the platinum-silicon system, a result which would be expected to extend to the PtSi-silicon system as well.

4.3. Effect of Process Variables on the Microstructure

As mentioned previously, there were a number of early indications that variations in the microstructure and, hence, the photoyield of PtSi/p-Si Schottky photodiodes could be achieved through modifications in the process sequence. Several studies of the effects of

various processing methods on the structure of PtSi films with thicknesses in excess of 1000Å have been reported in the literature;^{3,7,15} however, there has been no evidence of any similar efforts concerning films thin enough for use as photodetectors. To explore the possibility of improving the photodetector performance through process optimization, the fabrication parameters that were anticipated to have the highest structural impact were singled out for further study. This subset included the silicon wafer cleaning procedure used prior to deposition of the platinum metal, the temperature of the wafer during the deposition, and the amount of platinum actually deposited. The effects of substrate surface preparation on the behavior of the platinum-silicon system at room temperature were documented in the last section, and a significant impact was expected from each of the three variables in the closely related PtSi-silicon system. In order to identify trends caused by alterations in these parameters in a thorough and consistent manner, a fairly large matrix of samples was constructed and examined. The structural analysis of this matrix using ASP and TEM will be covered in this section. Correlation of these results with those of photoresponse measurements will follow later in this chapter.

To generate the matrix, 5–10 Ω-cm phosphorus doped (100)-oriented silicon wafers were used. These wafers are, of course, n-type; however, for the structural analysis, the conductivity type was ignored. Platinum layers 10, 30, and 300Å thick were deposited for every combination of deposition temperature and cleaning method examined. The 10Å deposition, which generates a PtSi film 20Å thick, is standard for actual photodiode arrays; while the 300Å (600Å silicide) layer is more typical of films used as Schottky contacts in integrated circuits. The intermediate thickness was added to insure consistency in the transition region. Films were evaporated onto substrates at both room temperature and the 350°C annealing temperature and were subsequently sintered for approximately one hour. The samples formed at low temperature required a 15 minute ramp-up to get to the required annealing temperature. The cleaning procedures used were those discussed in the previous section, i.e. the RRCA' method both with and without a final dilute HF dip.

When test wafers were fabricated using different permutations of these parameters, variations were discovered in the roughness of the PtSi-silicon interface, the roughness and contaminants present at the free surface of the silicide layer, and the average grain size in the polycrystalline films. A number of intertwining trends became evident, and an attempt will be made to classify these trends by process variable.

With one exception, the thinnest, i.e. 20Å, films show only minor differences in structure. TEM micrographs of two representative diodes are shown in Fig. 4.2. The PtSi layers appear to be fairly flat, with a silicide-silicon interface undulation of approximately 25% of the film thickness and grain boundaries every 100–150Å along the film. The air (actually glue in the picture)-silicide interface parallels the silicide-silicon interface, which leads to a conformal film of uniform thickness. The similarity ends, however, when the RRCA' clean without the added HF dip is combined with a room temperature deposition. In this case, isolated patches of silicide are produced instead of a uniform film, as indicated in Fig. 4.3. It has been observed that small amounts of platinum evaporated onto an oxidized substrate tend to ball up.¹⁶ Platinum exhibits no tendency to react with SiO₂ chemically, and the free energy is apparently lowered as a result of this islanding. It seems likely that the native oxide left by the peroxide clean and the low substrate temperature during deposition combine to produce a similar effect in this case which cannot be corrected through subsequent annealing. For the remaining samples, the various mixtures of clean and deposition temperature produce only slight contrasts, primarily in the degree of free surface contamination. ASP shows the presence of a thin oxide layer on top of all of the PtSi films grown in this study. For the thin films, significantly thicker oxide layers are generated when the RRCA' clean is employed without the HF dip, and marginally thicker layers result when a lower substrate temperature is used during deposition. No Auger data is shown for the thin film case, since the weak signal level emitted by the small amount of material and operation near the depth resolution limit of the technique lead to profiles that are not terribly illustrative.

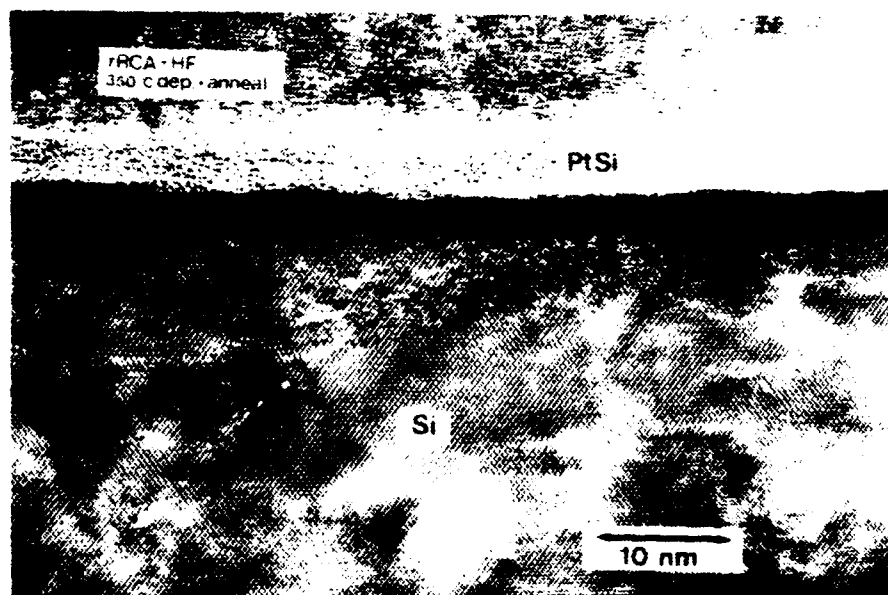
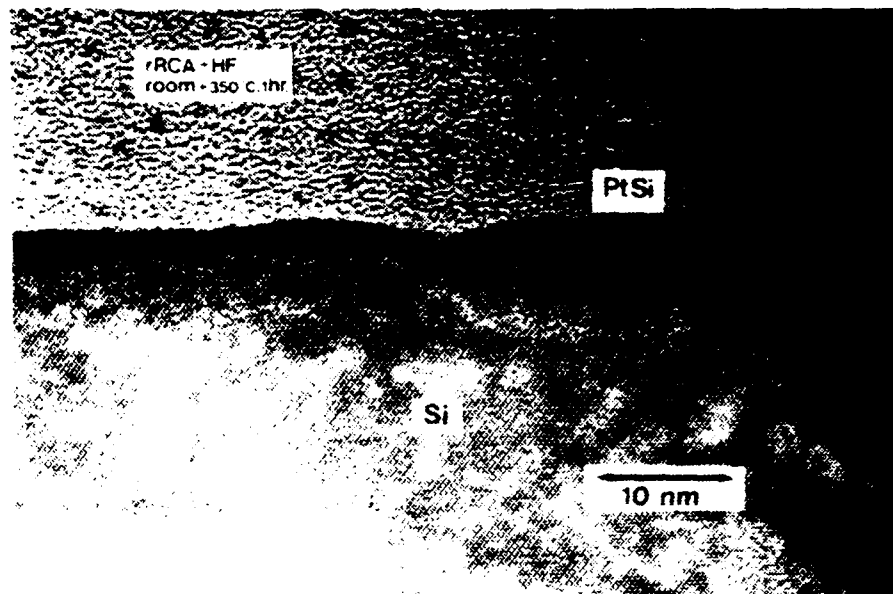


Fig. 4.2. TEM micrographs of two 20Å (nominal) PtSi/n-Si diodes formed via the deposition of platinum onto wafers at (a) a room temperature and (b) 350°C that were cleaned using the RRCA procedure followed by a dilute HF dip. The samples were annealed for one hour at 350°C following deposition.

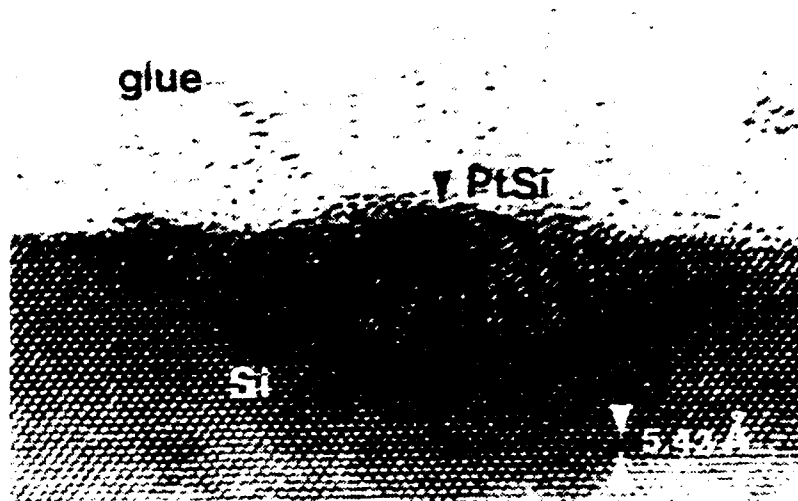


Fig. 4.3. TEM micrograph of the structure formed when 10\AA platinum was deposited onto a room temperature wafer cleaned using the RRCA' method, which leaves a thin residual oxide layer. The sample was annealed for one hour at 350°C following deposition.

The samples fabricated with silicide films of moderate thickness display essentially the same set of morphological trends as the thin film structures. This time, however, evaporation onto the RRCA' cleaned substrate at room temperature does result in the formation of an actual film, albeit a rather rough one. The effect is quite apparent in the Auger profile of Fig. 4.4(a), which is shown along with the profile of the sample formed via deposition onto an HF cleaned surface at the elevated temperature for contrast. Fig. 4.4 shows very clearly how the roughness of the silicide films can be monitored using ASP instead of the more involved TEM analysis. The silicide layer in Fig. 4.4(b) is very well defined, with a distinct ledge in the silicon profile and relatively sharp transitions in all three elemental profiles. In contrast, the silicon profile of Fig. 4.4(a) shows a much less distinct ledge, and the elemental profiles in general are more smeared at the interfaces. Broadening of an interface does not necessarily imply roughening *a priori*. In Section

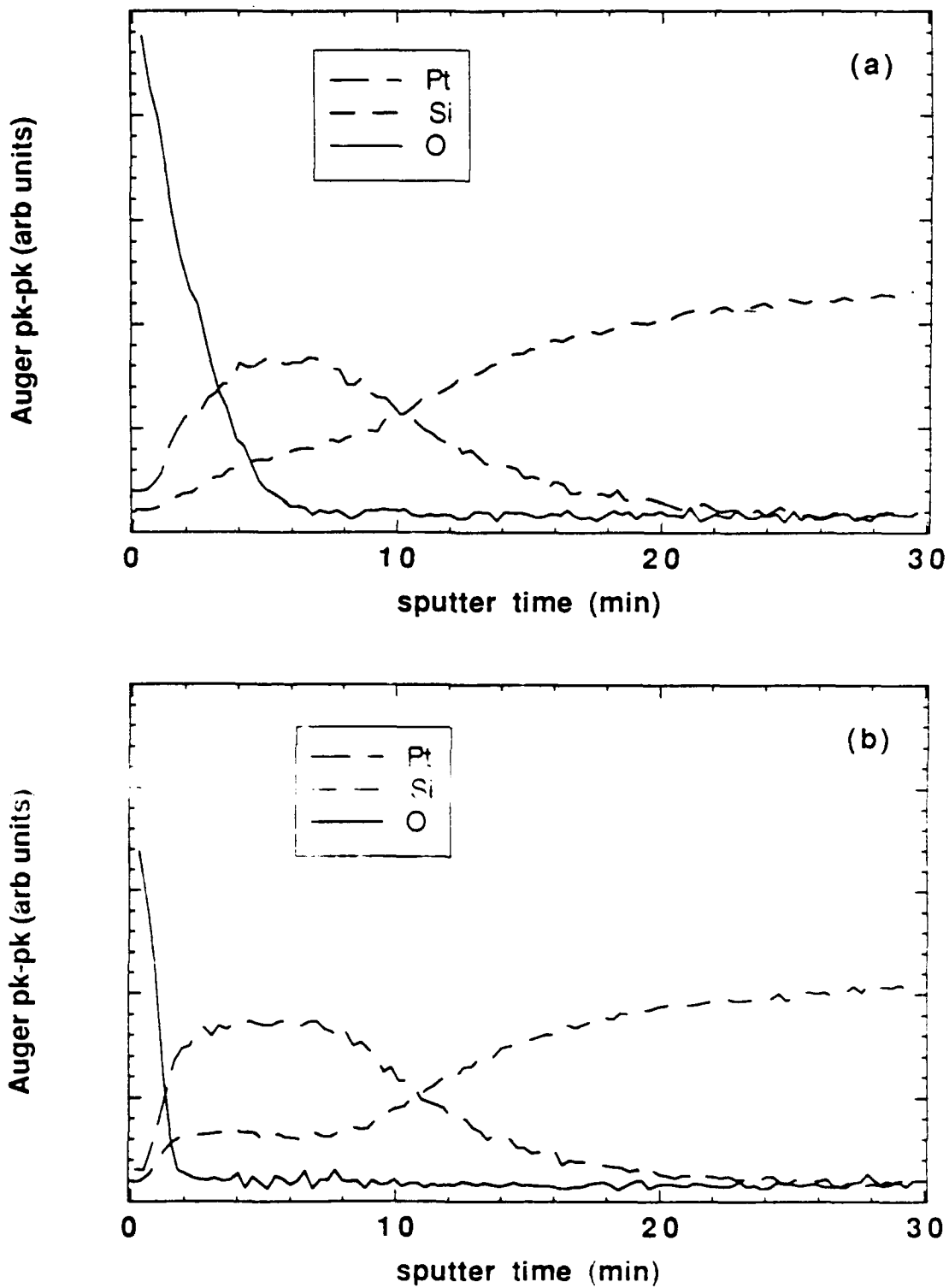


Fig. 4.4. Auger sputter profiles of two 60Å PtSi films on *n*-Si formed via platinum evaporation onto (a) an RRCA' cleaned substrate at room temperature and (b) a substrate at 350°C which had received an RRCA' clean followed by a dilute HF dip. Both samples were annealed for one hour at 350°C after deposition.

4.2, similar blurring of the platinum and silicon profiles for unannealed samples was considered an indication of chemical reaction rather than interfacial roughness. In general, corroboration by an independent analytical technique such as TEM is required to ascertain the specific cause for blurring. For the PtSi-silicon system, the source was indeed established to be interfacial undulation, which allowed subsequent monitoring with the ASP technique alone. Each of the two plots also reveals the presence of the thin oxide layer at the free surface that was mentioned in connection with the thinner silicide specimens. Just as before, the least amount of surface oxide contamination is found when the final HF dip is added to the wafer cleaning procedure and the evaporation is carried out at the annealing temperature.

A more extensive set of observations was made for the thickest group of silicide films, not all of which were in accordance with the thin film data. As mentioned earlier, several studies of this type concerning thick PtSi layers have already been reported. In particular, the work of Crider et. al.^{1,3} and Foll et. al.⁷ covers the influence of the substrate surface preparation on the eventual silicide film microstructure in as much detail as shall be employed in the current analysis. The data presented here supports their findings and extends the investigation to include the impact of deposition temperature and the correlation of the results with the thin film data. The TEM micrograph of Fig. 4.5 shows a cross-section of one of these samples. The most striking microstructural feature is clearly the apparent roughness of the silicide layer. Actually, the undulation at each interface as a percentage of the average film thickness is only slightly larger (for the sample shown) than that observed for the thinner coverages. However, in the present case, the air-silicide interface is divorced from the silicide-silicon interface so that variations in the two are out of synch. This gives a film that is decidedly not of uniform thickness which appears to have an extremely high degree of roughness. As the silicide layer thickness increases, the the film apparently ceases to be conformal at some point between 60 and 600Å. A relatively large grain size is also evident from the TEM image.

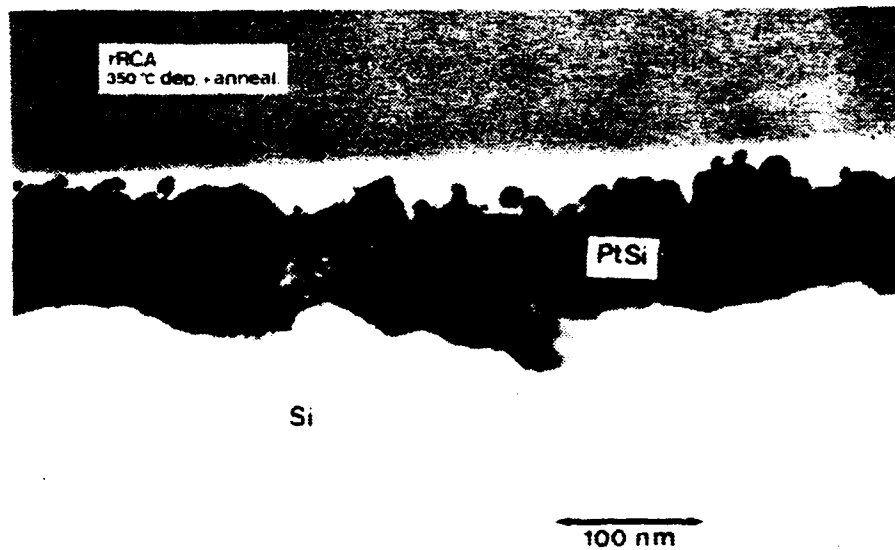


Fig. 4.5. TEM micrograph of a 600Å (nominal) PtSi film grown on an *n*-type silicon substrate cleaned using the RRCA' method and held at room temperature during the platinum evaporation. The sample received one hour anneal following a 15 minute ramp-up in temperature.

with average dimensions running anywhere from 3 to 6 times those discerned in the thin film micrographs depending on the other processing factors.

Interestingly enough, it seems that as the PtSi coverage increases, the effect of the wafer temperature during platinum deposition on the film microstructure reverses. For the thick films, both the interfacial roughness and the oxygen contamination level at the free surface are minimized for a given wafer cleaning procedure when the substrate remains at room temperature for the evaporation, in contrast to the trend observed earlier. The amplitude of the undulation of the PtSi-silicon interface is approximately 20–25% of the average layer thickness when room temperature deposition is employed, while evaporation at 350°C produces amplitudes of 30–35% as evidenced by Fig. 4.5. The roughness of the air-silicide interface is mainly a function of the cleaning method:

however, lower deposition temperatures do lead to noticeably smoother surfaces for a given cleaning method. Auger results reflect the corresponding reduction in surface oxide contamination with the lessening in surface roughness as well. It is not at all clear why this inversion of the microstructural trends should occur for increasing film coverage, and no satisfactory explanation of the phenomenon exists at this time. No obvious correlation between the deposition temperature and the average grain size in the silicide film was ever discovered.

Unlike the deposition temperature, the wafer cleaning method employed prior to the metal evaporation step impacts the thick film morphology in a manner quite consistent with the thin film data. The incorporation of the HF dip following the RRCA' clean causes substantial reductions in both the contamination and the unevenness of the air-silicide interface. Fig. 4.6 shows a comparison of the Auger profiles derived from thick film samples utilizing each of the cleaning techniques. The disparity in the oxygen presence in the vicinity of the top surface is readily apparent. Both plots also reveal additional contamination in the form of carbon, the existence of which is not observed in any of the thin film data. The shape of the carbon profile varies somewhat between the samples, but the total amount of carbon present does not change to any significant degree. The carbon signal seems to be connected more with the PtSi coverage rather than cleaning or deposition temperature. The slight broadening of the PtSi-silicon interface with increasing deposition temperature which was mentioned previously can also be discerned from Fig. 4.6. TEM analysis points out one further trend which cannot be witnessed using ASP. Although the RRCA' clean definitely corrupts integrity of the upper surface of the silicide layer, it is also associated with larger average grain sizes. The characteristic dimension of the grains drops from 600–700Å to 400–500Å when the HF dip is added to the cleaning procedure. This effect may result from a higher degree of isolation between the growing grains along the film when the native oxide is present to disturb the growth sequence.

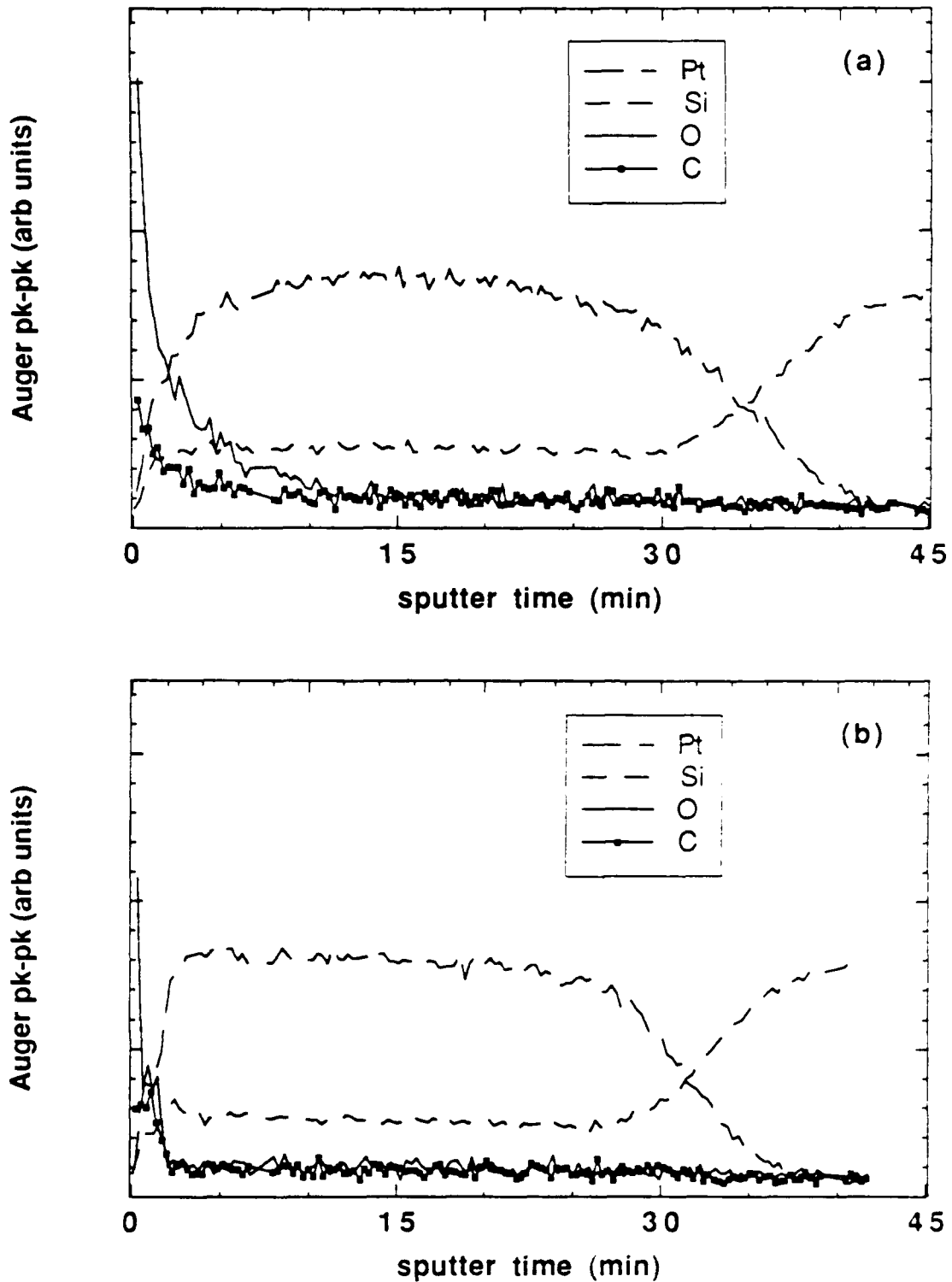


Fig. 4.6. Auger sputter profiles of two 600Å (nominal) PtSi films grown on *n*-Si through the evaporation of platinum onto (a) an RRCA' cleaned substrate at at 350°C and (b) a substrate at room temperature which had received an RRCA' clean with a subsequent dilute HF dip. Both samples were annealed for one hour at 350°C after deposition.

Despite the early expectations, none of the silicide layers characterized in the initial study exhibited anywhere near the level of undulation observed in the RADC diodes that were analyzed. Further studies were later implemented in order to address this troublesome detail. The first of these involved a closer examination of the effect of the HF dip employed as a final cleaning step in half of the previous work. It has been reported that silicon surfaces treated with concentrated HF solutions exhibit microscopic roughening and a certain degree of fluorine incorporation.^{17,18,19} The extent to which these factors might influence the subsequent growth of PtSi films was not clear. For the purpose of this study, only the 60Å silicide layers were grown and all substrates were held at 350°C during deposition. The 60Å thickness was chosen in order to allow observation of any interfacial roughness present with the Auger technique alone, as mentioned earlier. The concentration of the HF solution was varied from the original 50:1 H₂O:HF mixture all the way up to straight (49%) HF. Furthermore, various wafer exposure times running from 10 seconds to 10 minutes were tried at each concentration level. Unfortunately, the Auger profiles were virtually identical in each case, with no evidence of any change with either concentration or wafer immersion time. Variations in the HF dose level do not appear to change the degree of film undulation to any appreciable extent.

With the failure of HF to produce modulated films, one final investigation was initiated. All of the process variables which had so far been considered were directly related to the formation of the diodes. However, the RADC devices analyzed were actually test structures from wafers on which fully functional monolithic staring arrays with their associated CCD readout circuitry had been fabricated. This implies that the actual silicon surface sites where the diodes were formed had been subjected to a number of processing conditions not at all pursuant to the production of the detector elements. Although the smoothness of the initial surface of the wafers used by RADC had been verified,¹⁰ the surface condition immediately prior to diode formation in a functional array

remained unknown. With this in mind, the effect of the growth and subsequent strip of thick SiO₂ layers on the underlying silicon surface was called into question. Oxide growth has been observed to produce roughening of the underlying silicon-SiO₂ interface on both a microscopic and a macroscopic scale under certain growth conditions,^{17,20} and a sufficiently high concentration of HCl in the oxidizing ambient can produce oxide layers which are extremely rough.²¹ The diode sites are normally protected by a field oxide layer grown very early in the process flow which must be removed when diodes are to be formed. Moreover, the part of the sequence associated with the readout circuitry normally involves a number of high temperature secondary oxidation and annealing steps. To examine the impact of standard processing techniques of this type, a set of samples was prepared on which various types of thick oxide layers were grown and stripped off before the diode fabrication was performed. Wet, dry, and TCA/dry oxides ranging in thickness from 3000 to 7500 Å were grown in a standard oxidation furnace at temperatures between 1000 and 1100°C and then etched off in a solution of 10:1 H₂O:HF. After the oxides were removed, all samples were cleaned using the RRCA' clean followed by a 50:1 H₂O:HF dip. As in the HF study, only 60 Å PtSi layers were employed and all samples were heated to 350°C for the platinum evaporation. Despite these efforts, once again no contrast was evident between the Auger profiles of the various samples. No further attempts were made to induce film undulation after this study, and the source of the phenomenon remains a bit of a mystery. The effect very likely stems from either a combination of steps in the RADC process flow or some element in the processing environment unique to RADC. Whatever the cause, all attempts to duplicate the result at Stanford have proven to be unsuccessful.

4.4. Effect of Process Variables on the Photoresponse

While a rich variety of process-induced morphological phenomena is observed for increasing levels of PtSi coverage, the thin film diodes which are of the most interest for

photodetection display little obvious structural change when different fabrication conditions are employed except for the case in which no film actually forms. Some contrast in the level of contamination at the free surface of the silicide layers is evident which might affect the scattering of hot carriers at the interface, but the variation is not large. This does not bode well for attempts to affect the photoresponse of these devices through the optimization of the process flow. However, responsivity data from the diodes actually show much more contrast than might otherwise be expected. Samples were generated for responsivity measurements using the silicon shadow masks mentioned in Section 4.1. *P*-type silicon is obviously required for infrared photoresponse measurements, so (100) oriented boron doped wafers with resistivity values of 5–10 Ω -cm were employed. Only very thin film devices are important for photodetector applications, so test diodes with 10, 20, 40, and 80Å PtSi layers were proposed rather than the 20-60-600Å spread studied earlier. However, due to the difficulties involved in probing very thin films at very low temperatures, only the 80Å diodes have received extensive study. As in the morphological analysis, the effects of both the wafer cleaning method and the substrate temperature during the platinum evaporation were examined. One slight variation was introduced into the cleaning procedure, however. The order of the peroxide solutions was reversed, so that the acidic solution followed the basic. Since both solutions leave a similar native oxide layer on the silicon surface, the substitution of the "RCA" clean" is expected to have no significant impact on the results. Each of the wafers also received an additional 10:1 H₂O:HF dip after its removal from the vacuum system in an attempt to strip off the inevitable oxide layer which forms on top of a PtSi film during diode formation. Elimination of this layer was deemed to be desirable for ease in contacting the diodes. It was at this point that the importance of the oxide skin became clear. The HF etching solution did not wet the oxide surface very well at all, which led to the formation of bubbles on top of the smaller features including all three sizes of diodes created by the shadow mask. Physical agitation of the wafer boat proved to be incapable

of dispersing the bubbles. After the attempted etch, the wafers that had been cleaned prior to deposition using only the RCA' method, which were shown in Section 4.3 to possess the highest levels of surface contamination, displayed what appeared to be "coffee" stains on each of the silicide features including some of the large area contacts. With the aid of a microscope, it could be seen that ridges of contamination had formed around the edges of the bubbles present during the etch. This phenomenon would clearly be expected to substantially impact efforts to provide good electrical contact to diode arrays through secondary metallization. With a 5 micron radius tungsten probe tip inserted into the LTMP-2 probe mount, etched areas of the silicide films could be contacted in every case.

A comparison of the photoresponse performance of the various samples is shown in Fig. 4.7 in Fowler plot form. To obtain the internal yield Y , the raw response data obtained from the test setup was first normalized to the total output of the optical system obtained using the thermopile and then multiplied by the photon energy at each point to account for the fact that the photodiode measures photons per unit time while the thermopile measures energy per unit time.^{22,23} This calculation gives the relative voltage quantum efficiency as a function of photon energy. In the absence of a blackbody calibration standard, no attempt was made to determine any absolute quantities. Next, the optical absorption of a front illuminated 80Å PtSi film on a silicon substrate as a function of photon energy was calculated using Mooney's optical constants.^{24,25} When the calculated quantum efficiency is divided by this absorption curve, the relative internal voltage yield results. The data for each sample actually consists of two overlapping curves which correspond to the two different filters used in conjunction with the monochromator to obtain monochromatic radiation over the full spectral range shown. Fig. 4.7(a) displays the Fowler plots for the samples which utilized the RCA' clean alone prior to deposition. The contrast induced through the adjustment of the wafer temperature during the metal deposition step is striking. The apparent optical barrier height is much lower when the deposition is performed at room temperature rather than the 350°C

annealing temperature, with a value of approximately 0.26eV as opposed to 0.32eV. This result is rather intriguing, since the morphological study indicated that the room temperature deposition in the presence of a native oxide produces a noticeably rougher PtSi film. The 0.32eV barrier corresponds to a cut-off wavelength slightly less than 4 μ m, so that particular device would cover less than half of the 3–5 μ m spectral window. The slopes of the two Fowler curves are quite similar; however, the C_1^* value discussed in Section 2.2.2 would be expected to be lower for the high barrier case if the dynamic resistance of the diodes rises with the barrier height. As a side note, both curves exhibit a few characteristic wiggles which can be traced to the adsorption of residual gases onto the sample surface during the responsivity measurements. Although the system was ion pumped for approximately 20 hours prior to each measurement, the lack of any cold trapping surface in the measurement chamber other than the relatively small Joule-Thompson refrigerator and the sample itself resulted in a small amount of what appeared to be CO₂ adsorption during each cooling cycle based on the positions of the peaks in the energy spectrum.²² Fig. 4.7(b) shows the Fowler curves for the instances in which the wafers were cleaned using the RCA' method followed by an HF dip. When the platinum deposition proceeds with the substrate at room temperature, the photoresponse is not unlike that observed when the HF dip is neglected. The barrier height appears to be marginally higher in relation to the latter case at about 0.27eV, and the slopes of the two plots appear to be comparable. In contrast to the result observed in Fig. 4.7(a), however, the elevation of the deposition temperature actually lowers the apparent barrier height to between 0.24 and 0.25eV, the minimum barrier observed for the four combinations of processing conditions examined. This is the standard fabrication method that is used in practice, and the choice seems to be a good one. It is interesting to note that while the room temperature deposition generates a significantly higher Schottky barrier than the 350°C deposition, the Fowler plot in the former case has a far steeper slope. However, with reference to the C_1^* parameter, a lower dynamic resistance in the low barrier device

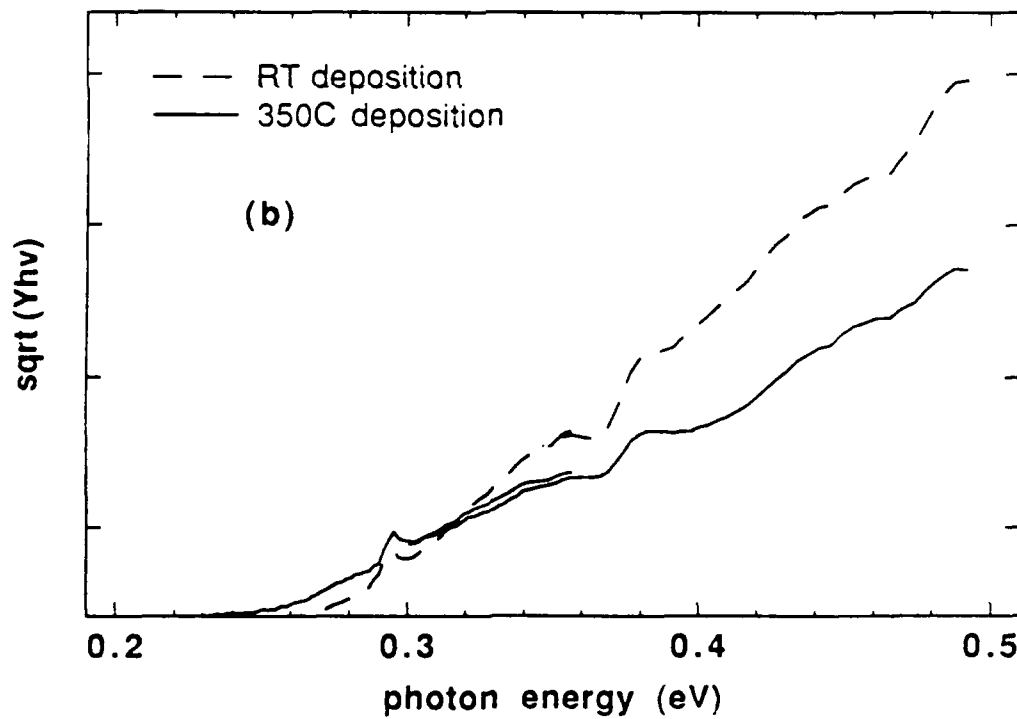
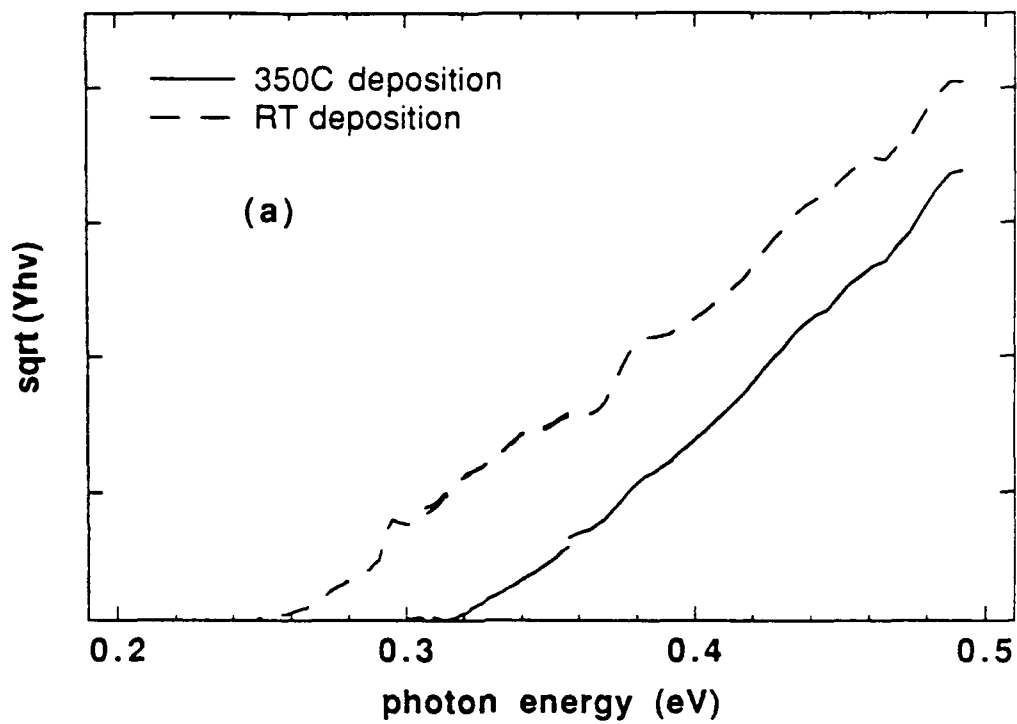


Fig. 4.7. Fowler plots of the relative internal voltage photoyield of 80Å PtSi/*p*-Si Schottky photodiodes which show the effects of variations in substrate temperature during metal deposition for a given substrate cleaning procedure. The samples in (a) were cleaned using only the RCA' method, while those in (b) received an additional 50:1 H₂O:HF dip.

could offset the apparent advantage in the responsivity. Nonetheless, the association of the lesser slope with the sample whose free surface was indicated in the morphological analysis to be the most ideal could indicate a connection between non-uniform surfaces and improved response.

The behavior of the barrier height as a function of fabrication method is somewhat unexpected. In light of the impact of the wafer cleaning procedure on the interfacial kinetics of the platinum-silicon system at room temperature and the contrast evident in the microstructure of the photodiodes after annealing, it is surprising that the barrier height appears to be nearly independent of cleaning technique when the evaporation takes place at room temperature. The sizable disparity between the barrier heights obtained when the substrate temperatures are elevated to 350°C during the deposition is just as curious. It seems that the time spent at moderate temperatures during the 15–20 minute thermal ramp, which is required after a room temperature deposition in order to reach the 350°C annealing point, influences the reaction kinetics in such a manner that cleaning effects are minimized. Since the formation of both Pt₂Si and PtSi can proceed at temperatures as low as 200°C,³ a substantial portion of the silicide reaction will occur during the ramp. However, the advance of the PtSi phase is tremendously slowed at lower temperatures, which provides a longer time for the generation of essentially Pt₂Si alone. Although PtSi appears to form only after Pt₂Si growth is completed even at 350°C under clean conditions, the time for Pt₂Si growth is quite short and there is probably some tendency for both phases to nucleate. The manner in which the nucleation sequence progresses could be significantly altered by the existence of a thin oxide layer at the platinum-silicon interface. The allocation of time for Pt₂Si stabilization on the one hand versus the competition between phases on the other could help to explain why the presence of the native oxide seems only to impact the barrier heights of samples formed via the elevated temperature deposition.

In conclusion, the correlation of the various processing methods with the resulting PtSi/*p*-Si diode microstructure and photoresponse produced mixed results. The study succeeded in showing that significant alterations in both the microstructure and the optically measured Schottky barrier height could indeed be effected through modifications in certain process variables. Unfortunately, from the standpoint of improving the quantum efficiency in the 3–5 μ m spectral regime, the changes induced were diametrically opposed to those desired. For thin film PtSi/*p*-Si photodiodes, the standard fabrication procedure involving deposition onto a heated substrate chemically cleaned with an HF dip as the final step yields the lowest Schottky barrier height, although the voltage responsivity appeared to be higher for the processing sequences which generated less ideal silicide films. With regard to thick contact films, room temperature deposition onto HF treated surfaces produces the most uniform layers.

References for Chapter 4

1. C.A. Crider, J.M. Poate, "Growth Rates for Pt₂Si and PtSi Formation Under UHV and Controlled Impurity Atmospheres," *Appl. Phys. Lett.* **36**, 417 (1980).
2. C. Canali, C. Catellani, M. Prudenziati, W.H. Wadlin, C.A. Evans, Jr., "Pt₂Si and PtSi Formation with High-Purity Pt Thin Films," *Appl. Phys. Lett.* **31**, 43 (1977).
3. C.A. Crider, J.M. Poate, J.E. Rowe, T.T. Sheng, "Platinum Silicide Formation Under Ultrahigh Vacuum and Controlled Impurity Ambients," *J. Appl. Phys.* **52**, 2860 (1981).
4. Murarka, Silicides for VLSI Applications (Academic, Orlando, 1983).
5. J.B. Bindell, J.W. Colby, D.R. Wonsidler, J.M. Poate, D.K. Conley, T.C. Tisone, "An Analytical Study of Platinum Silicide Formation," *Thin Solid Films* **37**, 441 (1976).
6. P.W. Lew, PhD thesis, Stanford University, 1983.
7. H. Foll, P.S. Ho, "Transmission Electron Microscopy Investigation of Silicide Formation on Slightly Oxidized Silicon Substrates," *J. Appl. Phys.* **52**, 5510 (1981).
8. J.R. Abelson, PhD thesis, Stanford University, 1987.

9. J.L. Hoyt, K.E. Williams, J.F. Gibbons, U.S. Patent No. 4,787,551.
10. J.R. Abelson, K.B. Kim, D.E. Mercer, C.R. Helms, R. Sinclair, T.W. Sigmon, "Disordered Intermixing at the Platinum:Silicon Interface Demonstrated by High-Resolution Cross-Sectional Transmission Electron Microscopy, Auger Electron Spectroscopy, and MeV Ion Channeling," *J. Appl. Phys.* **63**, 689 (1988).
11. M. Taubenblatt, PhD thesis, Stanford University, 1985.
12. W. Kern, D.A. Puotinen, "Cleaning Solutions Based on Hydrogen Peroxide for Use in Silicon Semiconductor Technology," *RCA Review* **31**, 187 (1970).
13. R.C. Henderson, "Silicon Cleaning with Hydrogen Peroxide Solutions: A High Energy Electron Diffraction and Auger Electron Spectroscopy Study," *J. Electrochem. Soc.* **119**, 772 (1972).
14. J. Ruzyllo, A.M. Hoff, G. Duranko, "Application of UV Radiation in Pre-oxidation Treatments of Silicon Wafers," presented at the Spring Meeting of the Electrochemical Society in Boston, Mass. (May, 1986).
15. C.-A. Chang, A. Segmuller, H.-C. W. Huang, B. Cunningham, F.R. Turene, A. Sugerman, P.A. Totta, "PtSi Contact Metallurgy Using Sputtered Pt and Different Annealing Processes," *J. Electrochem. Soc.* **133**, 1256 (1986).
16. J.R. Abelson, private communication.
17. P.O. Hahn, M. Grundner, A. Schnegg, H. Jacob, "The Si-SiO₂ Interface Roughness: Causes and Effects," in The Physics and Chemistry of SiO₂ and the Si-SiO₂ Interface, C.R. Helms, B.E. Deal, eds. (Plenum, New York, 1988), p. 401.
18. Y.J. Chabal, G.S. Higashi, K. Raghavachari, V.A. Burrows, "Infrared Spectroscopy of Si(111) and Si(100) Surfaces after HF Treatment: Hydrogen Termination and Surface Morphology," *J. Vac. Sci. Technol.* **A7**, 2104 (1989).
19. V.A. Burrows, Y.J. Chabal, G.S. Higashi, K. Raghavachari, S.B. Christman, "Infrared Spectroscopy of Si(111) Surfaces after HF Treatment: Hydrogen Termination and Surface Morphology," *Appl. Phys. Lett.* **53**, 998 (1988).
20. P.O. Hahn, M. Henzler, "The Si-SiO₂ Interface: Correlation of Atomic Structure and Electrical Properties," *J. Vac. Sci. Technol.* **A2**, 574 (1984).
21. J. Monkowski, J. Stach, R.E. Tressler, "Ellipsometric Investigation of HCl Oxides," in Semiconductor Silicon 1977 (Electrochemical Society, Princeton, 1977), p. 324.
22. P.N.J. Dennis, Photodetectors (Plenum, New York, 1986).
23. E.L. Dereniak, D.G. Crowe, Optical Radiation Detectors (Wiley, New York, 1984).
24. J.M. Mooney, Ph. D. thesis, University of Arizona, 1986.

25. J.M. Mooney, "Infrared Optical Absorption of Thin PtSi Films Between 1 and 6 μm ," J. Appl. Phys. 64, 4664 (1988).

Chapter 5

Kinetics of the Ir/SiO₂ and Pt-Ir/SiO₂ Systems and Implications for the Patterning of IrSi/*p*-Si Diode Arrays

As mentioned in Chapter 1, there has been significant interest in the extension of the wavelength response of Schottky detector arrays through the replacement of PtSi by IrSi.^{1,2,3} Iridium based arrays have the potential to provide imaging in the 8–14 μ m atmospheric transmission window, where factors such as smoke are less problematic and the blackbody curve for objects near ambient temperature is maximized.⁴ Two major obstacles have limited the proliferation of IrSi arrays: the degree of cooling required in order to obtain acceptable dark current levels and the difficulties encountered in iridium processing. The cooling problem stems directly from the low Schottky barrier height and may be regarded as fundamental to the device operation. Relief from this predicament must be derived from advancements in refrigerator technology rather than optimization of the detector technology. On the other hand, the fabrication challenges do not appear to similarly preclude the possibility for improvement. In this chapter, a spectroscopic analysis of the problems encountered in the patterning of IrSi/*p*-Si arrays will be discussed. One major source of these difficulties appears to be an unexpected reaction between the thin iridium films employed and SiO₂, an occurrence of which there is little or no evidence in the related platinum-SiO₂ system. The results of this study motivate an examination of the interaction between Pt-Ir alloys and SiO₂, the observations from which suggest a simple method for facilitating iridium patterning.

5.1. Characterization of the Ir/SiO₂ System

In Chapter 1, the failure of the standard platinum patterning technique when applied to iridium was briefly described. To delineate PtSi arrays, a SiO₂ masking layer is grown prior to the introduction of platinum and holes are etched where diode formation is intended. Platinum deposition and *in situ* annealing follow immediately. PtSi is formed in the holes cut through the masking oxide, but no reaction occurs between the platinum lying outside the holes and the underlying SiO₂. After their removal from the vacuum system, wafers are soaked in hot aqua regia which, fortuitously enough, dissolves away the unreacted platinum but leaves the silicide intact. The situation becomes more complicated when iridium is substituted for platinum. First of all, bulk iridium, unlike platinum, is not etched by aqua regia. In fact, iridium is one of the most corrosion resistant metals known, and it can be etched only quite slowly by certain electrochemical methods which would remove more than just the iridium.⁵ Despite the chemical impenetrability of the material, however, dry etching methods would be expected to allow reasonably easy displacement of the excess iridium, at the expense of an additional lithography step. While dry techniques have enjoyed some success, their application has proven to be less straightforward than anticipated.⁶ In order to ascertain the cause of these difficulties, an ASP study of the kinetics of thin iridium films on SiO₂ layers has been performed, the results from which provide strong evidence of non-equilibrium behavior that defies the predictions of bulk thermodynamics.

The samples employed in this set of experiments were fabricated on boron doped (100) silicon wafers of 5–10 Ω-cm resistivity. Oxide layers 370–380Å thick were thermally grown on these wafers using a standard MOS gate oxidation procedure. While typical masking layers are generally much thicker than these, the thinner oxides are more amenable to the Auger technique, since substantial charging of the sample can occur during analysis when the thickness of an insulating film exceeds 500Å. In any specimen,

the excitation of the constituent atoms by the primary electron beam and their subsequent relaxation via the emission of Auger electrons leaves a sizable population of multiply ionized atoms in the neighborhood of the surface. If the conductivity of the sample is high enough, the missing electrons are quickly replaced. However, insulating samples or those having thick insulating layers are restored to neutrality at a much slower rate, so that the surface develops a significant charge which builds until relieved by an electrostatic discharge. The oscillating surface potential modulates the observed kinetic energy of the detected Auger electrons, which causes the characteristic peaks to shift and broaden erratically. Few such problems appear for oxide layers of less than 500Å. The gate oxide layers are sufficiently thick that the SiO₂ phase is well established and no interaction between the substrates and the metal overlayers can take place, so the actual magnitude of the thickness should have no effect on the results. Iridium layers were deposited and annealed *in situ* using the e-beam evaporation system described in the last chapter. Prior to deposition, the oxidized wafers were chemically cleaned using the standard RCA cleaning procedure, which differs from the RCA' method of Chapter 4 only in the omission of the 50:1 H₂O:HF dip step sandwiched between the basic and acidic peroxide treatments. The oxide layers were thin enough to start with that no additional etching was wanted.

Since the etching behavior of the platinum-SiO₂ system is considered to be ideal, a reference sample was first made using platinum instead of iridium. A 60Å (nominal) layer of platinum was evaporated onto an oxidized substrate at 350°C and annealed for one hour, the standard conditions under which PtSi arrays are fabricated in practice. The sputter profile for this sample is displayed in Fig. 5.1. The platinum-SiO₂ interface appears to be reasonably abrupt when the presence of a very thin platinum layer, the use of a low sputtering flux, and the standard "instrumental broadening" are taken into account. A more quantitative analysis of the elemental profiles suggests an interface width of approximately 40Å, most of which can be attributed to the various experimental

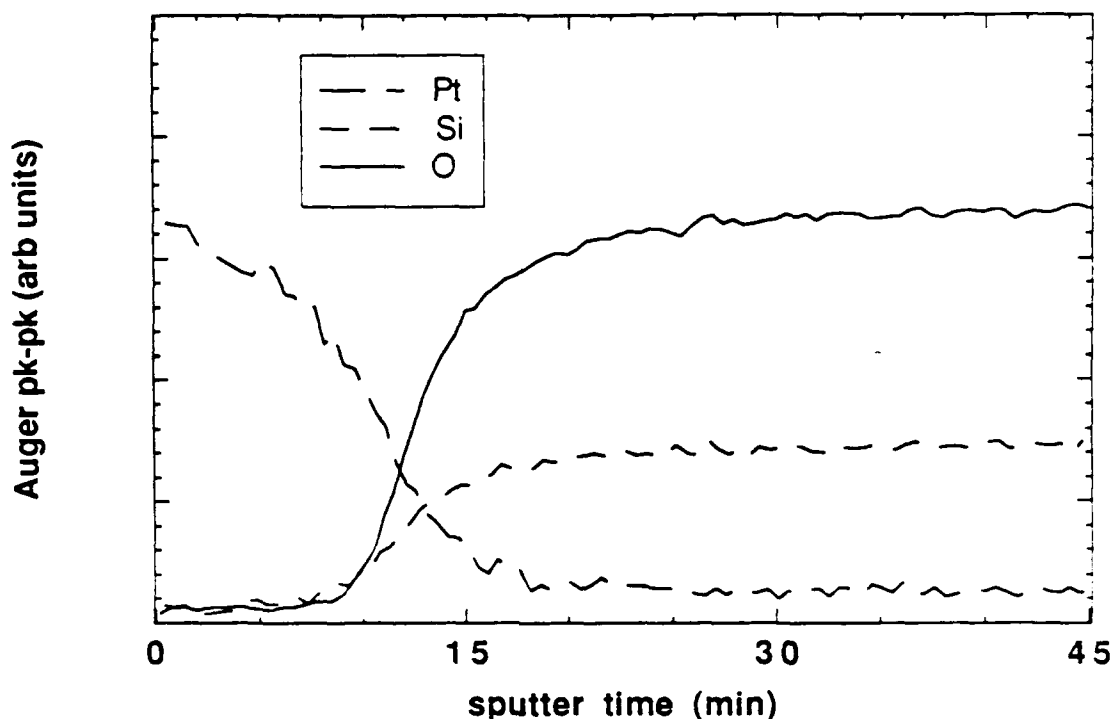


Fig. 5.1. Auger sputter profile of a 60Å platinum film deposited onto a gate oxide layer at 350°C and annealed for one hour.

artifacts just mentioned. The silicon and oxygen profiles indicate that neither is incorporated into the platinum film to any appreciable extent. In short, the Auger data shows simply a well-defined platinum layer on top of an oxide, with no anomalies of any sort. When a piece of this sample was immersed in hot aqua regia (1:1 HCl:HNO₃), the platinum layer was almost instantaneously removed. Most of the film appeared to float off before having the chance to dissolve. The platinum does not appear to adhere to the oxide particularly well, let alone react with it. Platinum films have also been observed to flake off even slightly oxidized substrates during the preparation of samples for TEM analysis.⁷ In light of this observation, the comparative difficulty involved in the stripping of iridium seems odd despite its relative insolubility.

With the establishment of the platinum reference data, a set of three iridium samples was prepared. Iridium layers nominally 60Å thick were evaporated onto the oxidized substrates: one at room temperature, one at 500°C, and one at 750°C. The sample formed

at room temperature was not annealed, while the other two were annealed for one hour at their respective deposition temperatures. Actual IrSi arrays are typically processed at 400–500°C, temperatures significantly higher than those employed in the fabrication of PtSi arrays. Although crystalline PtSi can form at temperatures as low as 200°C, the growth of IrSi has not been documented below 350°C.⁸ Nucleation may proceed at lower temperatures, but not at any practical rate. The Auger profiles for the set are given in Fig. 5.2. A definite microstructural trend is evident with increasing annealing temperature. The data derived from the room temperature sample in Fig. 5.2(a) are not unlike that generated by the platinum reference. The iridium–SiO₂ interface is ostensibly broader than the platinum–SiO₂ transition region; however, some of the added width can be ascribed to the fact that iridium sputters at a somewhat slower rate than platinum. The iridium film also seems to possess a higher oxygen concentration relative to the corresponding platinum layer. These structural differences, while noticeable, are certainly

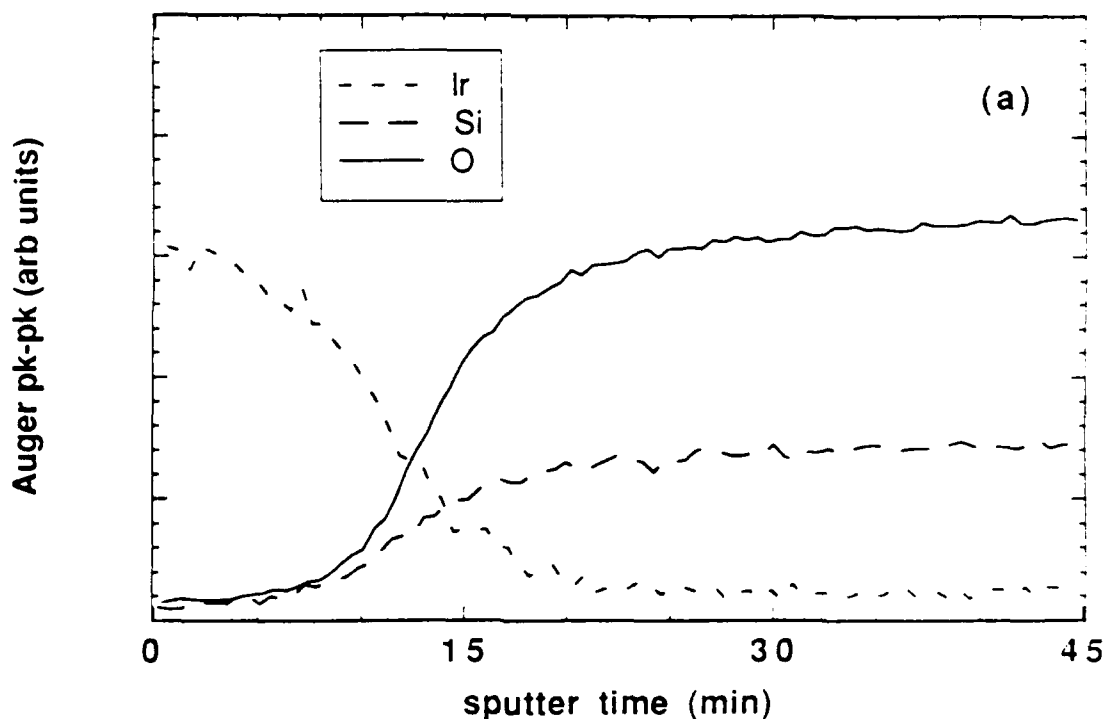


Fig. 5.2(a). Auger sputter profile of a 60Å iridium film deposited onto a gate oxide layer at room temperature with no subsequent anneal.

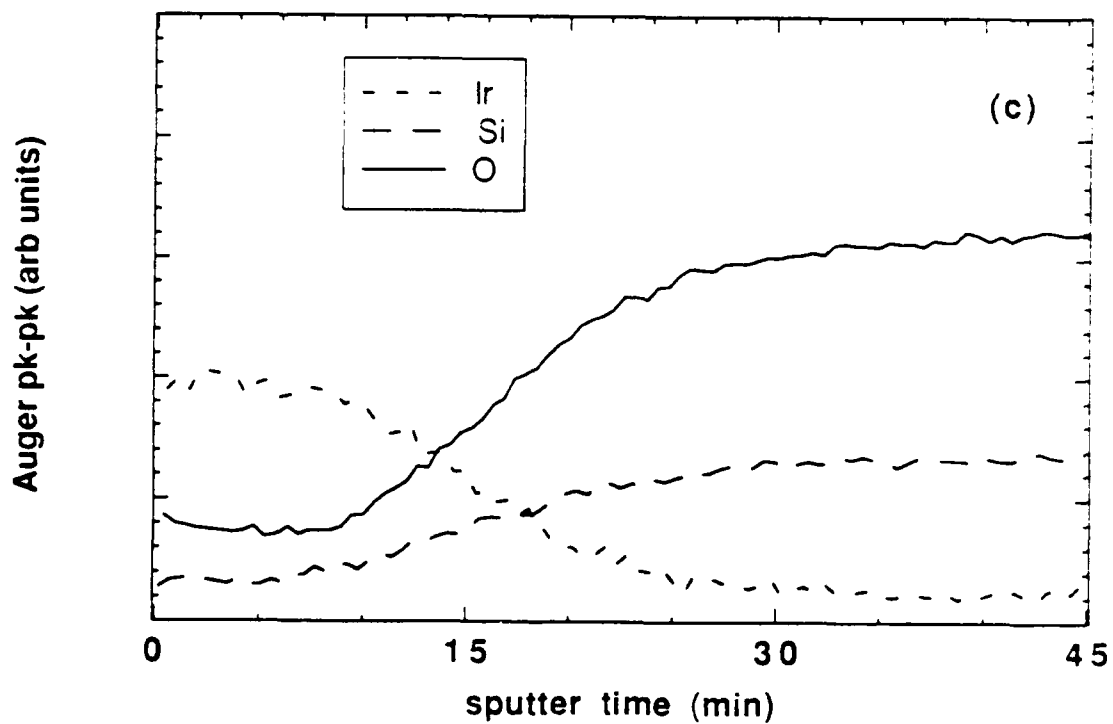
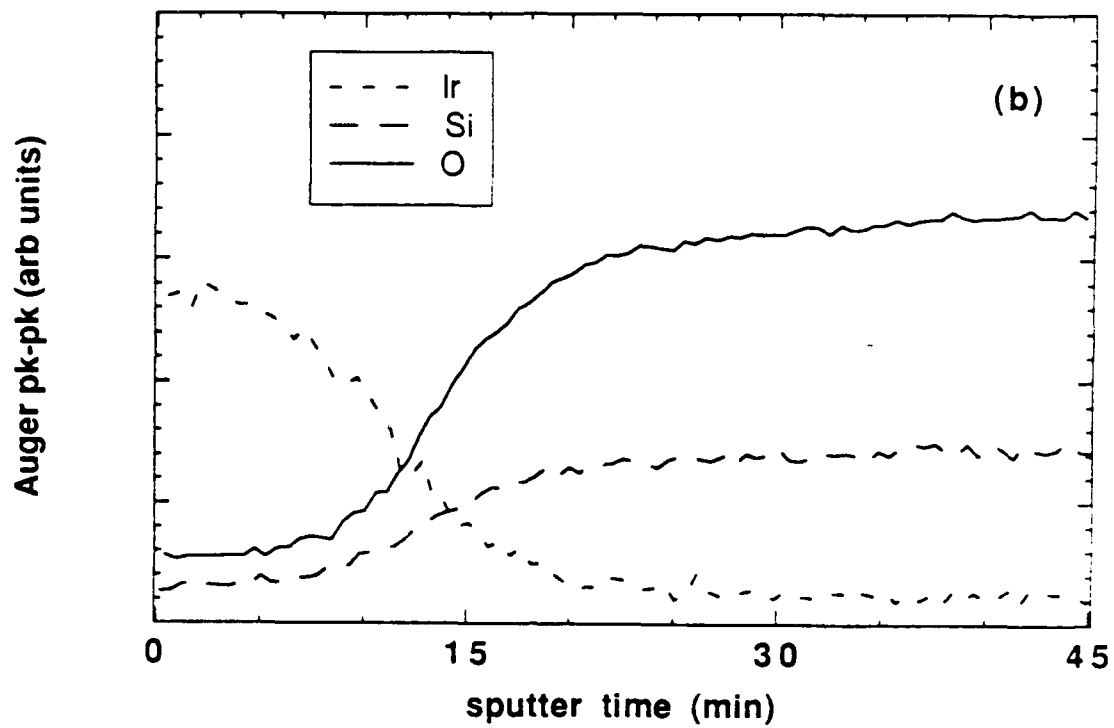


Fig. 5.2(b-c). Auger sputter profiles of 60Å iridium films similar to (a); however, the substrates were maintained at (b) 500°C and (c) 750C during the iridium evaporations and annealed for one hour.

not substantial. This situation changes as the processing temperature rises. The sputter profile of the sample annealed at 500°C, shown in Fig. 5.2(b), differs significantly from that of the room temperature specimen. The metal-oxide interface is further widened in this case, but the most obvious change is the considerable incorporation of both oxygen and silicon into the iridium layer. The penetration of the two elemental profiles to the surface of the sample could result from islanding or a high degree of film roughening; however, the well-defined plateau in the oxygen profile and the moderate increase in the interface width relative to that of the room temperature sample argue against these interpretations. The data instead seems to reflect the occurrence of an interaction between the oxide layer and the iridium film. Such a reaction is clearly undesirable, since 500°C, of course, represents a standard fabrication temperature for IrSi arrays. Examination of the data displayed in Fig 5.2(c) for the sample annealed at 750°C provides further evidence of a reaction. The iridium-SiO₂ interfacial region is extremely broad at this point, with the iridium signal level at the surface of the film noticeably depressed as the presence of the metal spreads. Both silicon and oxygen are even more visible in the metal layer than at 500°C, the enhancement of the oxygen level being particularly evident. The oxygen signal is actually even stronger than Fig. 5.2(c) implies. Some movement in the Auger peaks in energy space occurred during the analysis of this sample, apparently as a result of surface charging. The spectrometer had difficulty tracking the various peaks as they shifted, the oxygen peak creating the most problems. The charging phenomenon is entirely consistent with the notion of film oxidation. Based on the truncation of the Auger line by the observation window, the true oxygen signal level in the iridium film should be 30-40% higher than the elemental profile in Fig 5.2(c) reflects. Given this fact, it would seem that the ratio of oxygen to silicon in the metal layer is much greater in comparison to its value in the oxide. However, the 10⁻⁷ Torr vacuum environment provides little in the way of free oxygen, and no accumulation of silicon can be discerned near the interface.

This curious excess of oxygen will become important in the discussion of platinum-iridium alloy films which follows later in this chapter.

The Auger data furnishes strong evidence of a chemical interaction between the evaporated iridium layers and the underlying thermal oxide at elevated temperatures even under a vacuum of 10^{-7} Torr. Such a reaction would seemingly violate the predictions of bulk thermodynamics. Bulk SiO_2 has a heat of formation of -217.6 ± 0.8 kcal/mole, which should be much more stable than IrO_2 , the most favored iridium oxide, whose heat of formation is only -57.7 ± 3.0 kcal/mole.⁹ However, the profiles suggest that the compound which appears to be formed is actually some sort of oxygen-rich silicate rather than just a simple oxide. A reaction such as $\text{Ir} + \text{O}_2 + \text{SiO}_2 \rightarrow \text{IrSiO}_4$ might be quite favorable. Unfortunately, no thermochemical data on iridium silicates is available. While the possibility of the leeching of oxygen from the vacuum seems unlikely, it would explain both the Auger results and the thermodynamic conflict. In any event, the metal-oxide interaction would certainly wreak havoc on any attempt to pattern IrSi arrays either chemically or with dry etching techniques, and could, indeed, be the source of the difficulties that have been experienced.

5.2. The Effect of the Presence of Platinum on the Ir/SiO₂ Reaction

Given the observed interaction between iridium and SiO_2 at array processing temperatures and the apparent stability of platinum under the same conditions, it would seem logical to consider the introduction of platinum into the iridium structures as a means for improving the patterning characteristics. The concept of platinum-iridium multilayer silicide Schottky detectors has already received some attention, but for reasons different from those contemplated here.¹⁰ One of the nicer features of the PtSi/*p*-Si system is the extremely clean interface which is formed between the silicide and the silicon during growth. As mentioned in Chapter 4, the diffusion of platinum in the initial phase of silicide growth causes an effective snowplowing of impurities away from the original

metal–semiconductor junction toward the free surface, which leaves an extremely clean silicide–silicon interface. Unfortunately, the phase growth sequence is quite different in the case of IrSi.⁸ No Ir₂Si phase has ever been isolated. IrSi appears to form directly, with silicon as the dominant diffusing species. Any initial contamination of the silicon surface will, therefore, remain in the vicinity of the IrSi–silicon interface both during and after growth and detract from the performance and reproducibility of the finished devices. It has been demonstrated that this shortcoming can be circumvented in a multilayer detector by inserting a thin platinum film between the iridium and the silicon substrate. When this structure is annealed, the silicidation of the platinum, with its relatively low activation energy, proceeds first. The clean silicide–silicon interface associated with PtSi growth is formed as impurities are rejected into the interior of the multilayer. A limited amount of intermixing between the various layers occurs as the development of the IrSi phase follows, to the extent that the measured electrical barrier height (0.16–0.19eV) falls between those measured for PtSi and IrSi alone. While this device does offer improved reproducibility, it requires some sacrifice in the barrier height achievable through the use of IrSi by itself. Despite this drawback, the examination of platinum–iridium multilayers from a patterning perspective seems appropriate.

As an initial attempt, 60Å films of platinum and iridium were deposited in turn onto gate oxide layers identical to those employed in the previous section. The electron-beam evaporation unit in the deposition system has a three pocket hearth, which allows the sequential deposition of up to three different metals without breaking vacuum. Two different samples were fabricated, one featuring iridium on top of platinum and the other with the metal order reversed. The substrates were heated to 500°C prior to deposition in both cases and annealed for one hour afterward under continuous vacuum. An Auger analysis of the resulting multilayers suggests that they possess a unique combination of the microstructural attributes of iridium and platinum films annealed by themselves, as the sputter profile data given in Fig. 5.3 indicate. The apparent metal-oxide interfacial regions

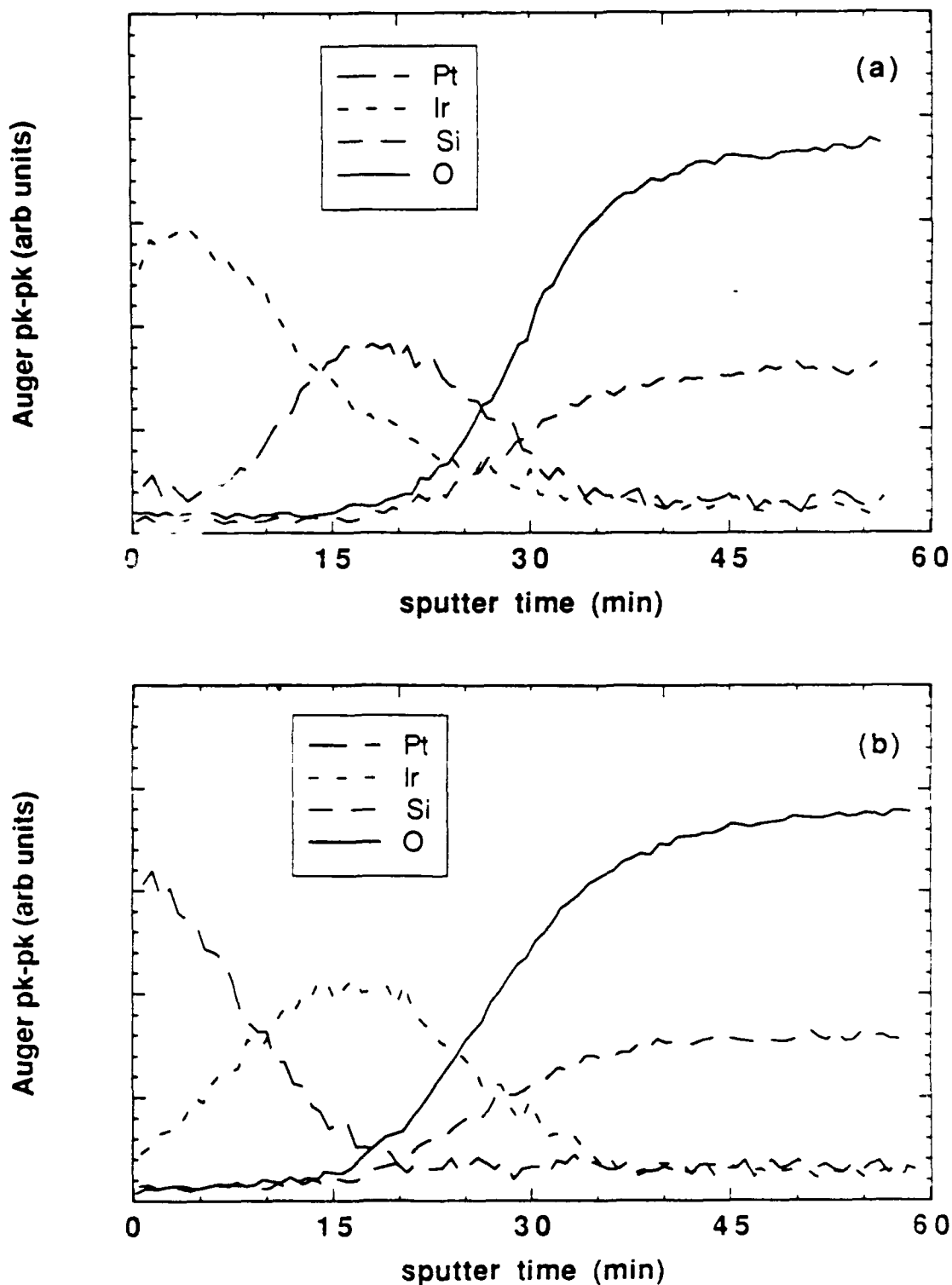


Fig. 5.3. Auger sputter profiles of (a) 60Å Ir / 60Å Pt / SiO₂ and (b) 60Å Pt / 60Å Ir / SiO₂ structures annealed one hour at 500°C. The magnitudes of the platinum profiles have been adjusted in accordance with the elemental sensitivity of platinum relative to iridium.

in Fig. 5.3 are nearly as broad as that found in Fig. 5.2(b) when iridium alone was annealed at 500°C. Some of the increased smearing may be caused by the greater interfacial depth relative to the sample surface in these specimens compared to those analyzed in Figs. 5.1 and 5.2; however, neither interface displays the sharpness of the platinum-oxide transition in Fig. 5.1. As might be expected, a noticeably wider interface is observed when iridium is deposited first. Despite the obvious broadening, however, neither multilayer film seems to possess significant levels of either oxygen or silicon, which were both present when platinum was absent. The signals indicative of a chemical interaction are, therefore, mixed. However, both multilayers could be completely removed by a five minute immersion in boiling aqua regia irrespective of the metal ordering. Whatever mechanism is responsible for the interfacial blurring discerned in Fig. 5.3 does not seem to inhibit film removal to any appreciable extent. The presence of an amount of platinum equal to that of iridium either at the surface or at the oxide interface apparently allows the etching of the mixed film using only the conventional platinum technique.

The comparative ease of etching of the metal even when iridium is deposited first is quite remarkable. While the data in Fig. 5.3 cannot unambiguously determine the source of the improvement over the case of an iridium film alone, they do suggest several possibilities. Although the respective platinum and iridium layers appear to remain essentially stratified during the annealing cycle, a certain amount of interdiffusion does seem to take place. The migration of platinum to the extent that a significant concentration is present everywhere in the multilayer cannot be ruled out based on these profiles. The leeching of the platinum from a partially alloyed structure during the immersion in aqua regia could undermine the integrity of the entire film and lead to its disintegration. An examination of the residual etching solution reveals the presence of a fine grit that is not found when platinum films alone are removed. Although this grit has not been subjected to any chemical analysis, it is reasonable to assume that it represents the final state of the

iridium, which would not be expected to dissolve whether platinum is present or not. Structural breakdown of the multilayer film through selective platinum dissolution could produce the residual slurry. Another explanation of the etching behavior centers on the lack of silicon or oxygen in the multilayer. Despite the ostensible broadening of the metal-oxide interface, the absence of any evidence of metal silicate phase formation implies that the chemical reaction which was shown to occur in the case of an iridium film alone may be prevented by the presence of platinum. With no reaction to bind the metal to the oxide, the etching solution may simply float off the layer. This hypothesis gains support from the earlier observation that thin films of platinum appear to float off similar oxides before dissolving in an aqua regia etch. The chemical explanation is no less plausible than the structural, but, unfortunately, the pervasion of platinum in the samples precludes the elimination of either.

In an effort to reduce the number of possible arguments and to determine the extent to which the platinum aided etching could be exploited, a second pair of samples was prepared using less platinum. This set employed platinum and iridium layers 30Å and 90Å thick, respectively, so that the relative presence of platinum was reduced from one half to one quarter while the overall multilayer thickness remained the same. Aside from this shift, all fabrication parameters were identical to those used in the creation of the 60Å / 60Å samples. The Auger sputter profiles of this pair are shown in Fig. 5.4. It is clear from the data that platinum is definitely not present in quantity throughout the multilayer in either sample, so that platinum does not appear to be the integral structural component that it appeared to be in the previous set. Once again, however, both silicon and oxygen are conspicuously absent from the metallic regions, an observation which suggests that the elevated temperature interaction between the iridium component and the oxide has again been prevented. Strangely enough, the metal-oxide interfaces seem to be more abrupt in these samples than in the earlier ones, an unexpected result in light of the reduction in the platinum level. Each of these factors would tend to support the suppressed reaction

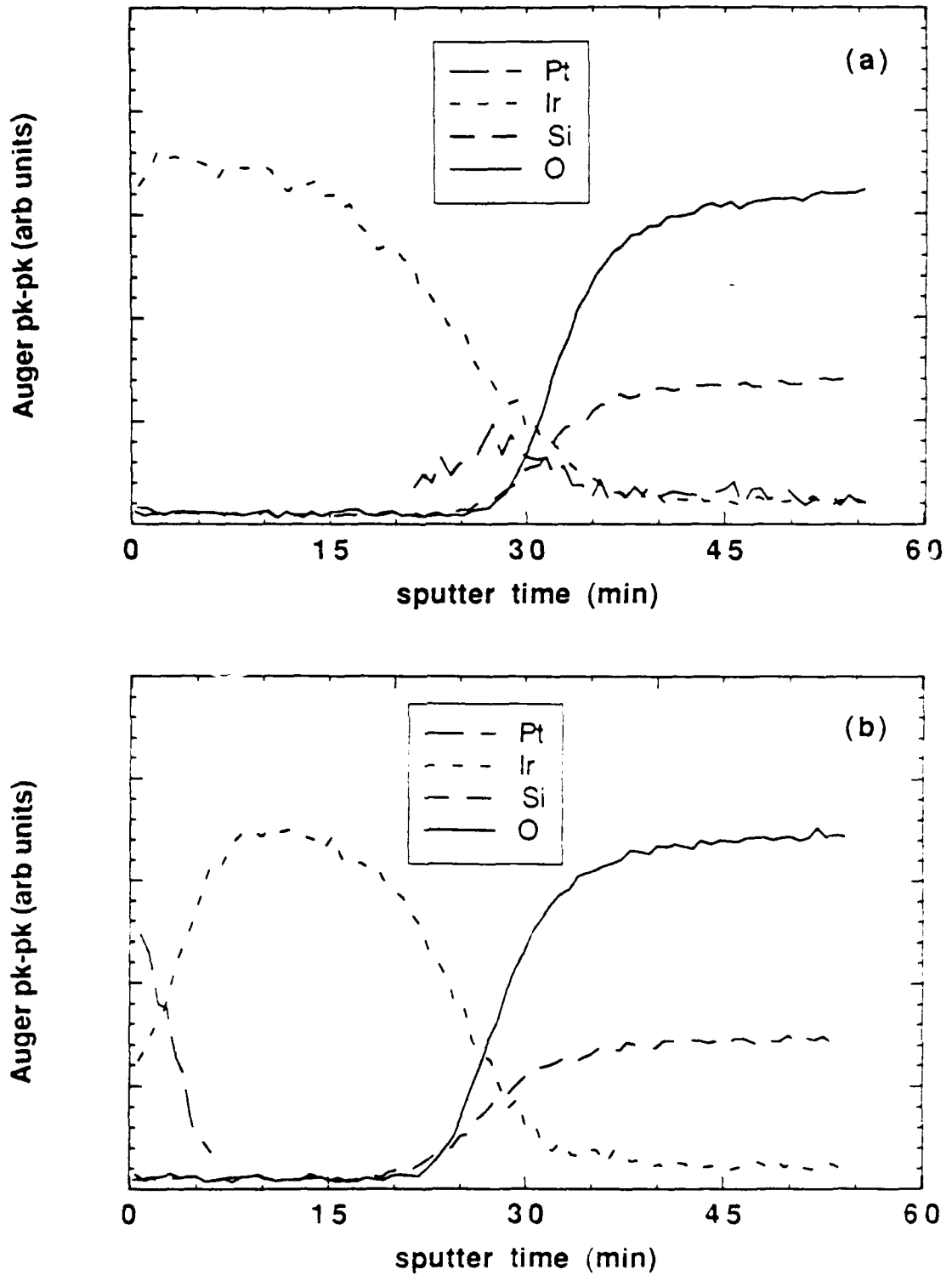


Fig. 5.4. Auger sputter profiles of (a) 90Å Ir / 30Å Pt / SiO₂ and (b) 30Å Pt / 90Å Ir / SiO₂ structures annealed one hour at 500°C. The platinum profiles have been adjusted in magnitude in accordance with the elemental sensitivity of platinum relative to iridium and also truncated due to the imposition of the iridium background onto the platinum spectrum at strong iridium signal levels.

argument over the structural disruption one if the multilayers could be chemically etched. As it turns out, the aqua regia treatment did, in fact, almost completely remove the films on both samples. A few flecks remained on each sample after etching, with a somewhat higher number on the sample employing platinum on top of iridium. Aside from these remnants, however, the multilayers were virtually eliminated from the oxides regardless of whether the platinum was inserted at the oxide interface or at the top surface, just as before. It does seem that the chemical interaction that takes place between iridium films and SiO_2 at high temperatures ceases when platinum is in evidence.

The ability of the platinum to block the iridium- SiO_2 reaction even when present only in small quantity atop a much thicker iridium layer is intriguing. Although it is possible that platinum may dissolve into the iridium layer at a partial concentration level below the fairly modest detection limit of the Auger technique (a few percent), another likely explanation exists. In the analysis of the Auger data plotted in Fig. 5.2, it was noticed that the ratio of oxygen to silicon found in the apparent iridium silicate which forms when platinum is not included exceeds that found in the oxide; yet no pileup of silicon resulting from SiO_2 segregation can be seen anywhere near the interface. This implies that oxygen must be added to the structure from an external source in order for the reaction to complete. The only source available, however, seems to be the vacuum environment, which certainly contains no tremendous wealth of free oxygen. On the other hand, the time frame over which the reaction appears to occur admits the possibility of a vacuum assist, a point which arises from a detailed consideration of the processing of the multilayer samples. The three pocket electron beam evaporation gun used to produce the various multilayers can only evaporate from one of the metal charges at a time. In order to change metals, the input power must be ramped down, the proper crucible translated into position, and the power gradually raised again until the evaporation rate of the new material stabilizes at the desired level. The entire exchange normally takes 5-10 minutes, a significant amount of time in terms of thin film reactions. Nevertheless, the multilayers

in which iridium was deposited first demonstrated little or no evidence of the chemical reaction which characterizes bare iridium films despite the fact that they were annealed for several minutes before platinum was introduced. This implies that the time scale for iridium silicate growth at IrSi array processing temperatures is fairly long and probably requires the better part of the one hour annealing cycle to register appreciable progress. Any reaction which depends on components obtained from a 10^{-7} Torr vacuum would be expected to display lethargy of this sort. Moreover, while the partial pressure of free oxygen is fairly insignificant in the system, oxygen containing water vapor and carbon oxides do constitute the majority of the residual gases. Adsorption and dissociation of these compounds could generate the excess oxygen that seems to be necessary. Platinum, even if present in just a thin layer, would be expected to form a barrier to the diffusion of oxygen from the free surface. The dependence of the iridium-SiO₂ reaction on the introduction of oxygen from the vacuum environment would explain the ability of a thin platinum layer to prevent its occurrence when located either at the metal-oxide interface or on top of the iridium layer.

This apparent capacity of platinum to inhibit iridium-oxide interactions even at a distance from the metal-oxide interface could have a substantial impact on the patterning of IrSi focal plane arrays. If the preclusion of silicate formation depended on the insertion of platinum between the iridium and the SiO₂, then the inferior spectral cutoff of the actual detector elements relative to those employing iridium alone would again limit the utility as reported in the earlier studies. The removal of the platinum to either the top surface or, perhaps, the interior of the iridium layer, however, might limit the detrimental effect on the Schottky barrier height. The Auger data in Fig. 5.3 suggest that platinum has a lower tendency to diffuse than iridium in a multilayer metal film, a favorable trait with regard to the maintenance of a low barrier. While the kinetics of platinum during silicide growth differ from those involved in alloying, the multilayer silicide diode sputter profile shown in Fig. 5.5 indicates that platinum deposited at the top surface forms a fairly localized

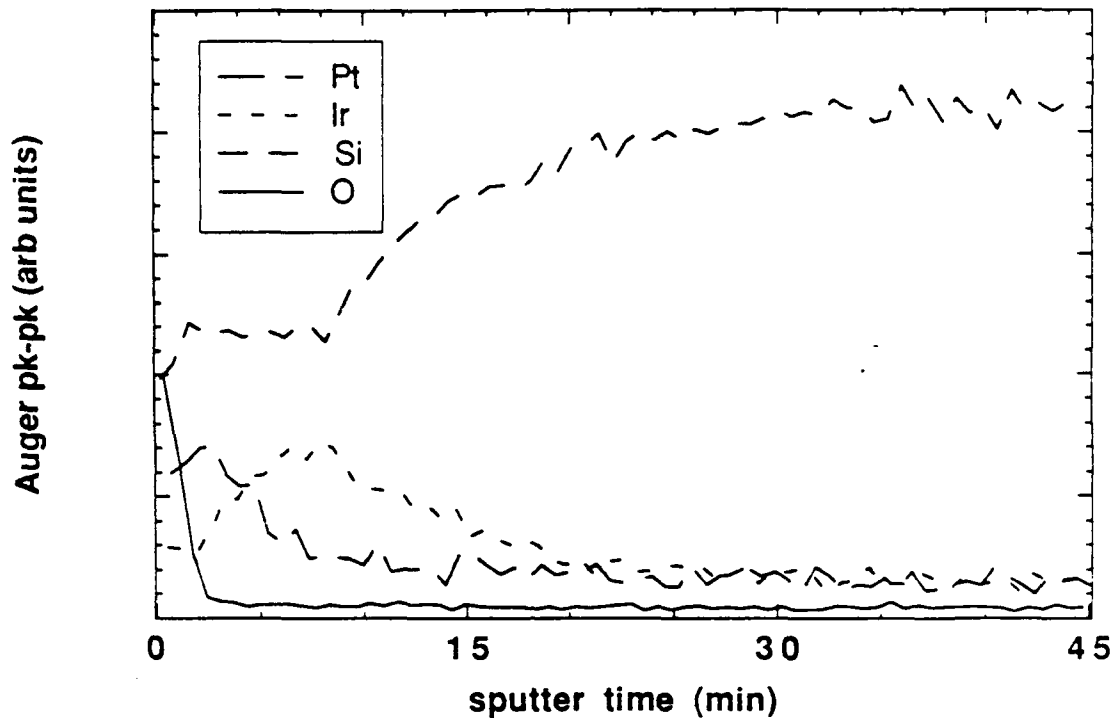


Fig. 5.5. Auger sputter profile of a multilayer silicide Schottky diode. A 30Å (nominal) layer of iridium and a slightly smaller amount of platinum were evaporated onto an HF cleaned *p*-Si substrate heated to 500°C and then annealed for one hour. The magnitude of the platinum profile has been adjusted to account for the elemental sensitivity of platinum relative to iridium.

silicide layer in this instance as well. The absence of PtSi at the substrate interface would be expected to preserve the IrSi/*p*-Si optical barrier height, although this could not be confirmed given the limited cooling capability of the internal photoresponse measurement system constructed for the PtSi/*p*-Si diode analysis.

Several discoveries reported in this chapter warrant a final mention here. It was revealed that a chemical interaction appears to occur between thin films of iridium and underlying SiO₂ layers at IrSi array processing temperatures even in a vacuum environment, a phenomenon which does not seem to take place in the related platinum-SiO₂ system. This observation might explain many of the difficulties that have been experienced in the patterning of IrSi focal plane arrays. Furthermore, it was demonstrated that the incorporation of relatively small amounts of platinum at either the iridium-oxide or

the iridium-vacuum interface could greatly inhibit this interaction, possibly by blocking the diffusion of oxygen from the imperfect vacuum to the metal-oxide interface. The presence of platinum at the top surface of the iridium layer should have a minimal impact on the barrier heights of Schottky photodiodes formed in holes etched through the oxide, a fact which could make the multilayer technique useful in IrSi array technology.

References for Chapter 5

1. P.W. Pellegrini, A. Golubovic, C.E. Ludington, M.M. Weeks, "IrSi Schottky Barrier Diodes for Infrared Detection," IEDM Tech. Dig., 1982, p.157.
2. N. Yutani, M. Kimata, M. Denda, S. Iwade, N. Tsubouchi, "IrSi Schottky-Barrier Infrared Image Sensor," IEDM Tech. Dig., 1987, p. 124.
3. B.-Y. Tsaur, M.M. Weeks, R. Trubiano, P.W. Pellegrini, T.-R. Yew, "IrSi Schottky-Barrier Infrared Detectors with 10- μ m Cutoff Wavelength," IEEE Electron Device Lett. **9**, 650 (1988).
4. P.N.J. Dennis, Photodetectors (Plenum, New York, 1986).
5. G. Petzow, Metallographic Etching (American Society for Metals, Metals Park, 1978).
6. J.M. Mooney, private communication.
7. K.B. Kim, private communication.
8. S. Petersson, J. Baglin, W. Hammer, F. D'Heurle, T.S. Kuan, I. Ohdomari, J. de Sousa Pires, P. Tove, "Formation of Iridium Silicides from Ir Thin Films on Si Substrates," J. Appl. Phys. **50**, 3357 (1979).
9. O. Kubaschewski, C.B. Alcock, Metallurgical Thermochemistry, 5th ed. (Pergamon, Oxford, 1979).
10. B.-Y. Tsaur, M.M. Weeks, P.W. Pellegrini, "Pt-Ir Silicide Schottky-Barrier IR Detectors," IEEE Electron Device Lett. **9**, 100 (1988).

Chapter 6

Conclusions and Suggestions for Further Work

Silicide-silicon Schottky barrier infrared focal plane arrays have and will continue to provide a reliable, cost effective high-resolution infrared imaging technology for some time to come. In the preceding chapters, a number of contributions to this field have been presented and discussed in some detail. It is instructive at this point to review those advances and mention some of the more promising directions indicated for future research efforts in this area. Despite the gains which have already been achieved, several remaining questions provide numerous opportunities for future study.

6.1. Conclusions of the Present Study

It has been demonstrated that the photoresponse of extremely thin film PtSi/*p*-Si Schottky photodiodes can be described very accurately by assuming that the motion of photogenerated hot carriers is primarily diffusive in nature. A mathematical model resembling that used to describe thermal diffusion in one dimension has been developed which allows the derivation of a relatively simple analytical solution for the internal photoyield per absorbed photon. The uncomplicated result elucidates the main physical mechanisms that determine the photoresponse in thin film detectors and identifies the device parameters which must be optimized in order to maximize the overall detector performance. A low Schottky barrier height proves desirable not only for extended wavelength response but for minimum subthreshold excitation inefficiency and maximum barrier transmission at a given incident photon energy. In addition, the mean hot carrier

lifetime with regard to both collisions with cold carriers and phonon emission should be as long as possible. The diffusion formulation was able to incorporate several mechanisms that had not or could not be studied in previous models, including hot carrier multiplication and energy losses due to the emission of optical phonons. The inclusion of multiplication explained some details of the curvature in the photoyield data generated by diodes with the thinnest silicide films, while phonon losses were shown to increase the effective Schottky barrier height. This seemingly detrimental influence of phonon emission in thin films devices differs from the positive impact observed in Schottky diodes with thick metal layers. Furthermore, along with its ability to reproduce the experimental data and illuminate the basic physics, the model can predict the optimum silicide film thickness with regard to the overall quantum efficiency when coupled with a suitable calculation of the radiation absorption of the silicide film. For operation at a wavelength of $4\mu\text{m}$, the estimated efficiency as function of PtSi thickness displays a fairly broad maximum which peaks between 10 and 15\AA , an unexpectedly thin film considering the anticipated drop in the absorption as the thickness approaches zero. No substantial reduction in efficiency is predicted as the layer falls from its optimum value down to about 5\AA , which could explain a number of "anomalous" response measurements reported in the literature; although the appropriateness of a diffusion model for "films" of this magnitude might be questionable. All things considered, the modelling work has contributed significantly to the understanding of the photoresponse properties of thin film Schottky diodes and should serve as an aid in their design.

Several issues still remain which could be addressed within the diffusion formulation. Further consideration of the form of the barrier transmission function is still in order. It was mentioned in the analysis of the transmission in Section 3.1 that the calculation of each of the various functions examined was based in part on the assumption of specular reflection at the silicide-silicon interface, while a comparison of the experimental data with Monte Carlo results suggested that the boundary scattering is more

diffuse in character. Partial or complete relaxation of the requirement that parallel momentum be conserved in the derivation of the transmission function is non-trivial; however, this exercise would be expected to produce the most realistic estimates of the actual transmission characteristics of the Schottky barrier. The anticipated rise in the predicted transmission would tend to lower the estimated hot hole-cold hole scattering length determined in the present study. In addition, the effect of the roughening of both the air (cavity)-silicide and silicide-silicon interfaces on the hot carrier dynamics could be modelled through the extension of the formulation to two dimensions. Since the degree of roughening often rises above what could reasonably be described as a perturbation, an analytical solution might not be achievable in this case. However, the differential form readily admits the utilization of numerical techniques which might be useful when dealing with large undulations. The greatest impact of the roughening, however, could actually be on the barrier transmission function, which brings the discussion back to the topic of more advanced modelling of the latter parameter. In any event, opportunities for additional work in this area certainly exist.

The probable connection between the device parameters and the microstructural characteristics of PtSi/*p*-Si Schottky diodes both stimulated and guided later efforts to improve the performance through modifications in the processing methods used in device manufacture. The effects of variations in the silicon substrate cleaning procedure employed prior to platinum deposition, the temperature of the wafer during deposition, and the total amount of metal evaporated on the resulting diode microstructure and the infrared photoresponse of thin film devices were studied in detail. Morphological analysis utilizing the techniques of transmission electron microscopy and Auger sputter profiling established a correlation between the use of low deposition temperatures and/or cleaning procedures leaving a native oxide layer and the subsequent roughening and contamination of the air-silicide interface in thin film diodes. Such irregularities would be expected to affect the transport of hot carriers by changing the reflection properties of that boundary.

Although little variation in the structure of the silicide-silicon interface was observed in thin silicide layers, photoresponse measurements showed significant changes in the apparent Schottky barrier height corresponding to the different sets of processing conditions. The lowest barrier height was achieved via deposition onto a wafer held at the annealing temperature that had been stripped of any native oxide using a dilute hydrofluoric acid solution. On the other hand, the procedures leading to the less "ideal" silicide surfaces seemed to heighten the increase in photoresponse for a given increase in the incident photon energy, suggesting a possible benefit from film roughening. In films thick enough for use as contacts, the smoothest layers were produced when platinum was evaporated onto a substrate at room temperature possessing little or no residual oxide. The correlation with deposition temperature seemed to reverse with increasing silicide layer thickness. All in all, it was clearly demonstrated that a broad range of changes could be induced in the microstructure and photoresponse of PtSi/*p*-Si diodes through variations in the diode fabrication techniques.

The potential for additional studies of the influence of processing on detector morphology and performance certainly exists. While barrier lowering below the level achieved by current technology was not accomplished, the results of the investigation suggest a means to this end. The smallest barriers were fabricated on wafers cleaned using the chemical procedure which left the least amount of residual oxide which were heated prior to deposition. Further improvement in the degree of silicon surface cleanliness beyond that achievable through wet chemical methods alone could lead to smaller barriers. Since the evaporation and annealing steps take place under vacuum anyway, vacuum cleaning techniques similar to those employed in molecular beam epitaxy might be utilized. In addition, the correlation of silicide surface roughening with an improved response level invites further attempts to intentionally roughen films through various means. Limited sputtering and/or low energy ion implantation might prove to be useful in this regard. Furthermore, only PtSi diodes were studied in this work due to the

lack of suitable equipment for analyzing the photoresponse performance of the extremely low barriers associated with IrSi/*p*-Si devices. A similar investigation of IrSi diodes would be highly appropriate. In particular, since impurities initially present at the silicon surface are not swept away during the growth of IrSi as they are when PtSi forms, the wafer cleaning procedure used before metal deposition should prove to be critical. Significant advances in IrSi/*p*-Si diode performance through modifications in cleaning methods are a distinct possibility.

Finally, the tendency of thin films of iridium to react with SiO₂ masking layers was revealed in an investigation to determine the source of the patterning difficulties that have plagued IrSi focal plane array fabrication. An analysis of samples fabricated at various temperatures suggested that the deposited iridium is converted into an iridium silicate phase, the extent of the reaction increasing with the annealing temperature. Auger data indicated that the ratio of oxygen to silicon in the silicate exceeds that which characterizes the underlying oxide, an observation which implies that additional oxygen is supplied to the reaction by the absorption of residual gases present in the 10⁻⁷ Torr vacuum environment. Since platinum is known not to react with either oxygen or SiO₂ at the relatively low temperatures employed in array manufacture, an examination of the stability of iridium-platinum multilayer films on SiO₂ was performed, which demonstrated that the introduction of platinum could prevent the growth of a silicate phase. Little or no evidence of reaction was discerned even when relatively small amounts of platinum were inserted either between the iridium and the oxide or on top of the iridium, which lends credence to the idea that platinum functions as a blocking layer for the diffusion of oxygen through the iridium layer. The multilayer films could be almost completely removed in every case simply via immersion in boiling aqua regia, the method commonly used for etching films of platinum alone. These findings have significant implications for the delineation of IrSi diode arrays. Since platinum does not appear to migrate very far during the silicidation of the multilayer films, the encapsulation of iridium with a thin platinum layer should greatly

ease the patterning of IrSi/*p*-Si arrays without adversely affecting the low Schottky barrier height.

A few additional questions linger in connection with the iridium studies. Blanket evaporations were employed in all of the multilayer samples studied, and it remains to be seen how the presence of pixel-sized features on the order of 10 μm might affect these results. A determination of the minimum amount of platinum which is necessary either at the top surface or, perhaps, in the interior of an iridium layer to prevent silicate formation has not yet been carried out either. Both of these studies are needed in order to take full advantage of the results of the current work.

6.2. Specific Contributions of This Work

Although the previous section provided a comprehensive summary of the research program documented by this dissertation, it did not explicitly specify the ways in which the results have advanced the field of Schottky infrared imaging. A succinct enumeration of these contributions would, therefore, be beneficial. Both the fundamental understanding of Schottky photodiode operation and practical array design and fabrication technology have been furthered as a consequence of this work; and together these gains have enhanced the state of the art.

The first important contribution was the development of a simple yet accurate analytical model that predicts PtSi/*p*-Si Schottky diode photoresponse as a function of either photon energy or silicide thickness. The essential feature of this calculation was the apparent ability to describe the essential physics of the photoresponse process in a very simple manner without resorting to the complicated multi-parameter numerical methods which characterize previous analyses of the problem. By eliminating unnecessary complexity and correcting some of the errors in earlier studies, the model was able to explain some of the unusual experimental findings reported in the literature. In addition, this formulation of the problem permitted the incorporation of several mechanisms which

had received little or no study in previous attempts to model the response yet were found to be quite important, such as the detailed energy dependence of the hot carrier transport parameters, hot carrier multiplication at higher energies, and energy losses due to optical phonon emission. The simple description of the response and the discovery of the importance of these neglected phenomena have improved the general understanding of Schottky detector performance, which should aid attempts to improve it.

In addition, a consistent, systematic evaluation of the impact of certain processing conditions, specifically wafer cleaning procedure, metal deposition temperature, and silicide layer thickness, on subsequent PtSi/*p*-Si diode microstructure and infrared photoresponse was performed for the first time. The ability to substantially change both the structure and performance through variations in the process flow was clearly demonstrated. While no improvement over current performance standards was obtained, the trends observed from the thorough analysis provide a strong indication that such advances could be achieved through vacuum wafer cleaning and intentional film roughening. Any enhancement would directly benefit current middle infrared imaging needs.

Furthermore, the studies of the Ir/SiO₂ and Pt-Ir/SiO₂ systems have identified a means by which the manufacturability of IrSi/*p*-Si focal plane arrays could be significantly improved. The discovery of an unexpected and previously unknown chemical reaction between iridium and SiO₂ masking layers at array processing temperatures even under high vacuum explained much of the trouble that has been experienced in iridium lithography, and the further revelation that platinum encapsulation can prevent this reaction provides an extremely promising method for eliminating these problems. This finding should find immediate application in array production.

6.3. Novel Device Concepts

6.3.1. The Active Optical Cavity

While a number of future projects follow very directly from this research effort, a few more creative ideas have arisen as well. One such concept involves the use of an active rather than a passive optical cavity, in which the SiO_2 dielectric layer is replaced by either lightly doped polysilicon or a mixture of polysilicon and oxide as indicated in Fig. 6.1. The presence of two emitting boundaries could substantially improve the collection efficiency of hot carriers in the silicide layer. The application of the basic diffusion formulation to a situation in which the escape velocity into the polysilicon layer is the same

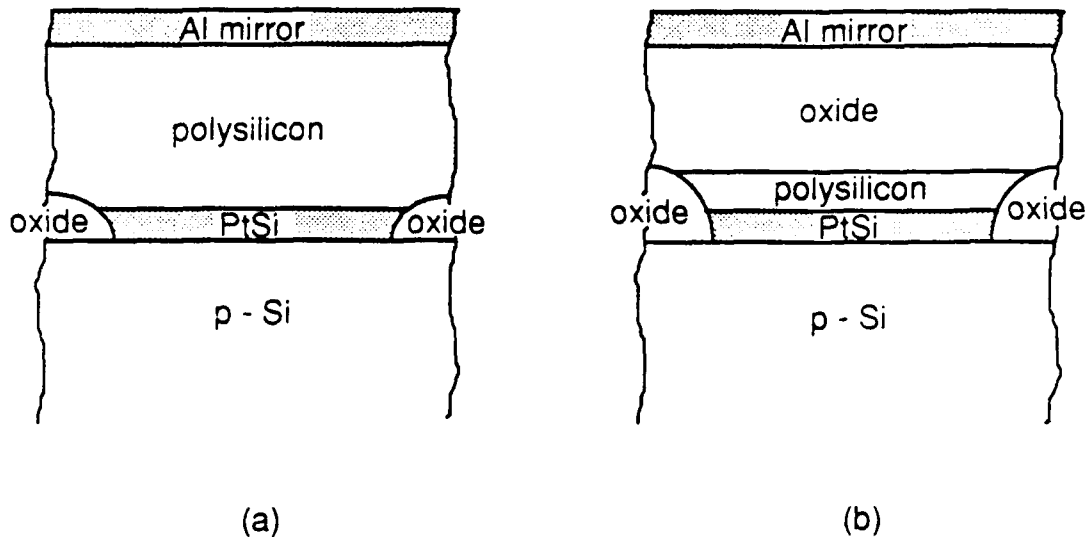


Fig. 6.1. Two alternative designs for a Schottky photodetector utilizing an active optical cavity. The hybrid cavity on the left may prove the more practical.

as that into the substrate indicates that the yield per absorbed photon would be given by the expression

$$Y = \left(\frac{h\nu - \phi}{h\nu} \right) \frac{1}{1 + d/(2C\tau)} , \quad (6.1)$$

which differs from the solution for the standard detector given in Eq. (2.16) by the factor of two in the denominator. This intuitive result shows that the addition of the second boundary has the same effect as doubling either the transmission of a single barrier or the hot hole lifetime. Moreover, the improvement in the transport efficiency of hot carriers in this structure implies that the silicide layer thickness can increase to accommodate a higher level of absorption. With these considerations in mind, the maximum quantum efficiency achievable with this device is found to be almost twice (about a 75% improvement) that of a standard detector at a wavelength of $4\mu\text{m}$, with an increase in the optimum silicide thickness of approximately one half. The higher index of refraction of silicon relative to SiO_2 improves the overall absorption induced by the cavity as well. However, the problems associated with the necessary patterning required of an active cavity for good image resolution, the transfer of the emitted holes into the CCD readout circuitry, and the presence of an electrically active mirror-cavity interface suggest that the hybrid cavity design might prove to be a more practical design. In either case, the performance of the Schottky detector could be improved without a tremendous increase in process complexity.

6.3.2. The Heterostructure Schottky Diode

Another idea which grew out of the conclusions of the modelling effort is a Schottky-like heterostructure diode, a project which is currently under investigation. It was pointed out earlier that two of the main factors which limit the performance of silicide-silicon Schottky photodiodes are the exceptionally short hot hole lifetime and the subthreshold excitation inefficiency. Both of these problems stem from the presence of a high density of filled electron states close to the Fermi level in the silicide layer. If it were possible to eliminate these states, it is conceivable that impact of these complications could

be lessened. This goal might be accomplished by the replacement of the silicide with a suitable low bandgap semiconductor. The intended energy band diagram for such a structure is shown in Fig. 6.2. Unlike conventional heterojunction detectors, in which the band offset between the two materials determines the response properties, this device operates in a manner similar to a standard Schottky detector. Holes are excited across the low bandgap and over any band discontinuity into the silicon substrate. The ideal band alignment would feature little or no valence band offset, so that the "barrier height" associated with such a structure would be determined primarily by the bandgap in the overlayer. The gap, which reduces the concentration of scattering centers and the level of unproductive absorption, is the essential feature of the overlayer material. Since the band alignment is not terribly critical, a high degree of epitaxy should not be required. As in the case of the silicide detectors, a polycrystalline overlayer film should suffice, which would

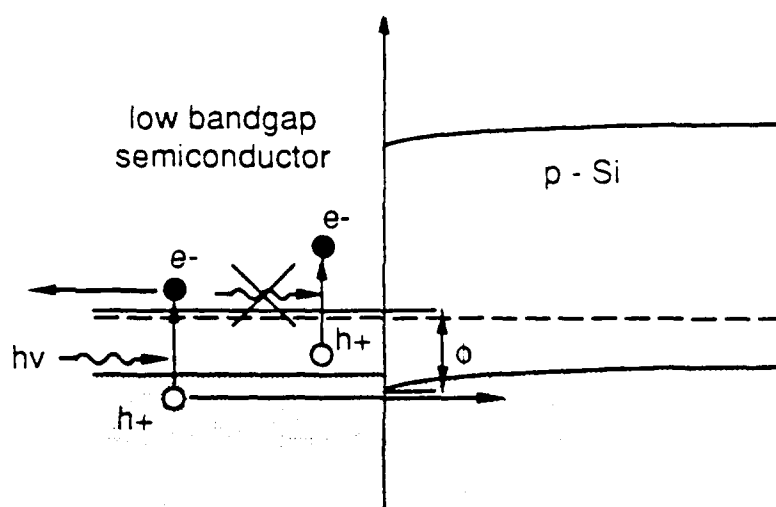


Fig. 6.2. The energy band diagram of the heterostructure Schottky detector.

ease the fabrication requirements substantially with respect to standard heterojunction devices.

The heterostructure concept does have some potential problems. Since the detector threshold is associated with absorption near the band edge, the radiation absorption will be much lower for a given overlayer thickness compared to the case of the silicide detector, even when the wasted excitations are taken into account. Although the anticipated increase in the hot hole lifetime derived from the reduction in hot hole-cold hole scattering should allow the utilization of much thicker films than is possible with silicides, it remains to be seen whether or not a net gain will occur relative to the silicide devices. Moreover, the need for a low valence band offset suggests that a high work function low bandgap semiconductor must be chosen, a requirement that leads to difficult-to-process ternary compounds such as $\text{Pb}_{1-x}\text{Sn}_x\text{Te}$ (LTT) and $\text{Hg}_{1-x}\text{Cd}_x\text{Te}$ (MCT). Theoretically, a material with low conduction band offset to *n*-type silicon would be at least as good a choice; however, none are available. LTT appears to be the current overlayer of choice. Despite the possible shortcomings of the heterostructure photodiode, the potential for a high efficiency silicon-based detector centered around this idea remains high. Between this concept, the active optical cavity, and the suggestions mentioned earlier, it is clear that much room remains for future research efforts in the area of infrared Schottky barrier focal plane array technology.

Appendix A

Radiation Absorption in Schottky Photodiodes

In Chapter 1, the internal photoemission process in Schottky photodiodes is divided into three distinct phases: radiation absorption, hot carrier transport, and barrier transmission. The diffusion analysis in Chapters 2 and 3 focuses on the latter two steps, since the absorption problem has already been examined in detail in the literature.^{1,2,3} However, an accurate determination of the absorption is certainly essential to any attempt to predict the photoresponse and deserves some elaboration. This appendix provides a description of the absorption calculation and demonstrates the impact of such design enhancements as anti-reflection coatings and resonant optical cavities. The influence of the short hot carrier lifetime on the optimum cavity architecture and the diode absorption efficiency will be discussed as well. While cavities and coatings cannot eliminate all of the inherent shortcomings in Schottky devices, they certainly provide a substantial improvement over the absorption levels achieved by the bare diodes alone.

Fig. A.1 again shows the ideal one-dimensional Schottky diode both with and without its various absorption-amplifying options. There are two vastly different physical scales present which divide the absorption calculation into two separate parts. On one hand, the films on top of the silicon wafer are all relatively thin. For example, the cavity, which is usually the thickest of these, is on the order of $1\mu\text{m}$ in width. In contrast, the substrate is several hundred microns thick, a distance which suggests a possible loss of phase coherence in a wavetrain passing through it.² The coherence length provides a rough estimate of the layer thickness beyond which the coherence between internally

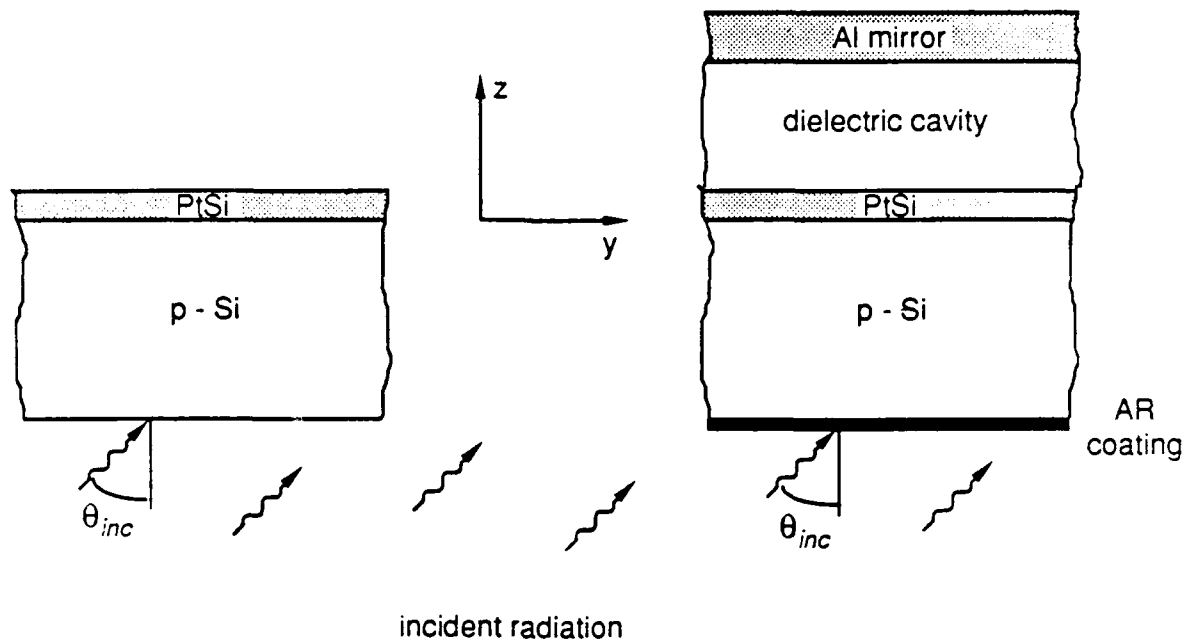


Fig. A.1. The ideal one-dimensional PtSi/*p*-Si Schottky photodiode both with and without an anti-reflection coating and a resonant optical cavity. The structures are not drawn to scale—the silicon wafer is two orders of magnitude thicker than the cavity.

reflected wave fronts will be lost, and can be calculated from the expression

$$l_{coh} \sim \frac{(\lambda_{ave})^2}{\Delta\lambda}, \quad (\text{A.1})$$

where λ_{ave} is the average wavelength of the radiation and $\Delta\lambda$ is the spread in wavelengths encompassed by the wavetrain.^{4,5} For light spanning the 3 to 5 μm wavelength window, l_{coh} will be about 8 μm in free space, or 2–3 μm in silicon where the wavelength of the radiation is shorter. This implies that multiple reflections of light in a layer much thicker than a few microns will not be coherent and their intensities will add, while reflections in a film much thinner than 2–3 μm will maintain a definite phase relationship and their field vectors will add. Since the substrate is far thicker than this, the back surface of the wafer is effectively decoupled from the front. It should be noted that very narrow filtering of the incident radiation either in the laboratory or in certain applications may reduce $\Delta\lambda$ by over

an order of magnitude and increase the coherence length to a value that is not insignificant in relation to the substrate thickness. However, even in this case the light will only be partially coherent, and the assumption of incoherence should cause few problems. After the decoupling across the wafer is taken into account, the calculation presented here will employ linearly polarized, monochromatic plane waves for simplicity, even though dephasing would not occur in a fully consistent plane wave analysis.

The calculation starts with the determination of the net radiation intensity incident on the silicide film as a function of the total intensity impinging on the back, i.e. silicon, side of the detector. Since a light ray is dephased in any pass across the substrate, it can be treated as a billiard ball with its intensity established by a wave travelling in only one direction, as opposed to a sum of two net waves travelling in opposite directions. The total intensity which reaches the coherent part of the device is then deduced by adding up the intensities of each of the individual reflections of the wave as it bounces back and forth inside the substrate. The summation of the resulting geometric series leads to the result

$$I_{inc,PtSi} = \frac{(1 - |R[air/Si]|^2)\gamma}{1 - (\gamma |R[PtSi/Si]| |R[air/Si]|)^2} I_{inc,diode} \quad , \quad (A.2)$$

where γ is the factor by which the intensity is attenuated in one pass across the substrate due to absorption by the silicon, i.e.

$$\gamma = e^{2ik_0 d_{substrate}(n_{Si} + ik_{Si}) \sec \theta_{Si}} \leq 1 \quad , \quad (A.3)$$

and $R[x/y]$ indicates the electric field reflection coefficient for a single reflection at the interface between medium x and medium y. In Eq. (A.3), k_0 represents the magnitude of the wave vector of the incident plane wave in free space, n_{Si} and k_{Si} are the real and imaginary parts of the refractive index in the silicon wafer, $d_{substrate}$ is the width of the wafer, and θ_{Si} is the angle the wave vector makes with the z axis normal to the wafer surface. In the absence of any anti-reflection coating, $R[air/Si]$ can be determined from the standard Fresnel equations for reflection at a boundary between two semi-infinite

media.^{4,5} A coating, if used, would reduce the value of $R[\text{air/Si}]$ to some degree, and a perfect coating would imply that $R[\text{air/Si}] = 0$. $R[\text{PtSi/Si}]$, on the other hand, depends on the details of whatever structure exists on the front side of the wafer and cannot be calculated in isolation. However, the "impedance method" commonly discussed in texts on electromagnetic theory slanted toward engineering applications provides a straightforward method for calculating the reflection from stratified media.⁶ Although the fairly large number of layers present in a cavity leads to an analytically lengthy result, the calculation readily lends itself to a recursive computer solution. The mathematical details of this procedure will not be related here.

To describe the analysis of the coherent part of the problem, a closer look at the fields involved is helpful. The standard electromagnetic wave equation, derived from the classic Maxwell equations, governs the allowed electric and magnetic field configurations in an arbitrary medium. The general solution of the wave equation for a harmonic wave linearly polarized in the x direction is given by

$$\begin{aligned}
 E_x(y,z) &= E_{x+} e^{ik_0(n+ik)[(z-z_0)\cos\theta - (y-y_0)\sin\theta]} \\
 &\quad + E_{x-} e^{-ik_0(n+ik)[(z-z_0)\cos\theta + (y-y_0)\sin\theta]} \\
 H_y(y,z) &= (n+ik)\cos\theta \left[E_{x+} e^{ik_0(n+ik)[(z-z_0)\cos\theta - (y-y_0)\sin\theta]} \right. \\
 &\quad \left. - E_{x-} e^{-ik_0(n+ik)[(z-z_0)\cos\theta + (y-y_0)\sin\theta]} \right] \\
 H_z(y,z) &= (n+ik)\sin\theta \left[E_{x+} e^{ik_0(n+ik)[(z-z_0)\cos\theta - (y-y_0)\sin\theta]} \right. \\
 &\quad \left. + E_{x-} e^{-ik_0(n+ik)[(z-z_0)\cos\theta + (y-y_0)\sin\theta]} \right], \quad (\text{A.4})
 \end{aligned}$$

where once again k_0 is the magnitude of the wave vector in free space, n and k are the real and imaginary parts of the refractive index in the particular medium, y_0 and z_0 are the y and z coordinates of some randomly chosen reference point, and θ is the angle the wave vector makes with the z axis.⁶ In a bounded region such as a thin film, E_{x+} and E_{x-} represent the net phasor amplitudes of waves travelling in the positive and negative z

directions. From these expressions, the net power density flowing in the positive z direction can be determined using the phasor form of the Poynting vector, i.e.

$$I(y, z) = \text{Re} \left\{ \frac{1}{2} E_x H_y^* \right\}. \quad (\text{A.5})$$

The substitution of the expressions given for E_x and H_y in Eq. (A.4) into Eq. (A.5) leads to the result

$$I(y, z) = \frac{1}{2} |E_{x+}|^2 \text{Re} \{ 1/Z_z^* \} \left[e^\varphi - |E_{x-}/E_{x+}|^2 e^{-\varphi} + \frac{\text{Re} \left\{ 1/Z_z^* \left[(E_{x-}/E_{x+}) e^{-i\xi} - (E_{x-}^*/E_{x+}^*) e^{i\xi} \right] \right\}}{\text{Re} \{ 1/Z_z^* \}} \right], \quad (\text{A.6})$$

where

$$Z_z = \frac{E_{x+}}{H_{y+}} = -\frac{E_{x-}}{H_{y-}} = \frac{\sec \theta}{n + ik}$$

and $\varphi(z-z_0, y-y_0, n, k, k_0, \theta)$ and $\xi(z-z_0, y-y_0, n, k, k_0, \theta)$ represent phase and attenuation terms that drop out later in the analysis. In the case of non-absorbing media, the last of the three bracketed terms in Eq. (A.6) vanishes; however, all terms must be retained in the present case.

If a plane interface free of trapped charge is now inserted normal to the z axis through z_0 , Eq. (A.6) will describe the power flow across the boundary. For $z = z_0$ and uniform illumination over the diode in the y direction, φ and ξ will both disappear and the power density flow becomes

$$I(z_0) = \frac{1}{2} |E_{x+}|^2 \text{Re} \{ 1/Z_z^* \} \left[1 - |R|^2 + \frac{\text{Re} \{ (R - R^*)/Z_z^* \}}{\text{Re} \{ 1/Z_z^* \}} \right], \quad (\text{A.7})$$

where

$$R = \frac{E_{x-}}{E_{x+}}$$

In the absence of any loss at the interface, E_{x+} , E_{x-} , and Z_z will be continuous and can all be referenced to the incident medium ($z < z_0$). The absorption of a planar layer as a function of the total incident intensity, i.e.

$$I_{inc,PtSi} = \frac{1}{2} |E_{x+,Si}|^2 \text{Re}\{1/Z_{z,Si}^*\} \quad (\text{A.8})$$

from Eq. (A.2) can now be determined by subtracting the net power density flowing out of the layer at a second boundary at some $z_1 > z_0$ from the net power density flowing in at z_0 . In order to evaluate this quantity, it is necessary to find the values of Z_z in both the layer and in the incident medium, the values of R at the two interfaces, and the ratio of the E_{x+} term in the layer to that in the incident medium. Regardless of how many other layers are placed on top of the film in question, i.e. at larger values of z , these quantities may be obtained in an algebraically messy but straightforward manner by recursive application of Snell's law, the impedance method, and the boundary conditions on E_x and H_y .⁶ Once again, the details of the complete solution will be suppressed, since, although numerical approximation techniques are not required, the calculation lends itself to computer evaluation rather than an explicit derivation.

Given an algorithm for the determination of the absorption of the PtSi layer in all of the various design configurations possible, it is instructive to examine graphically the impact of the different enhancements on the optical performance. The necessary optical constants can be found in the work of Mooney^{2,3} and Palik.⁷ Fig. A.2 shows the influence of both a perfect anti-reflection coating and a properly tuned optical cavity on the optimum silicide absorption at $4\mu\text{m}$ as a function of thickness. Each curve exhibits an almost linear rise with PtSi thickness for the thinnest films, a peak between 175 and 200Å, and a subsequent decay to some constant value for thicker films. Table A.1 lists the maximum value of each curve displayed. The table demonstrates that the addition of either a coating or a cavity to the bare diode will clearly increase the maximum absorption level by more than a third. Together, however, the two features can guarantee almost

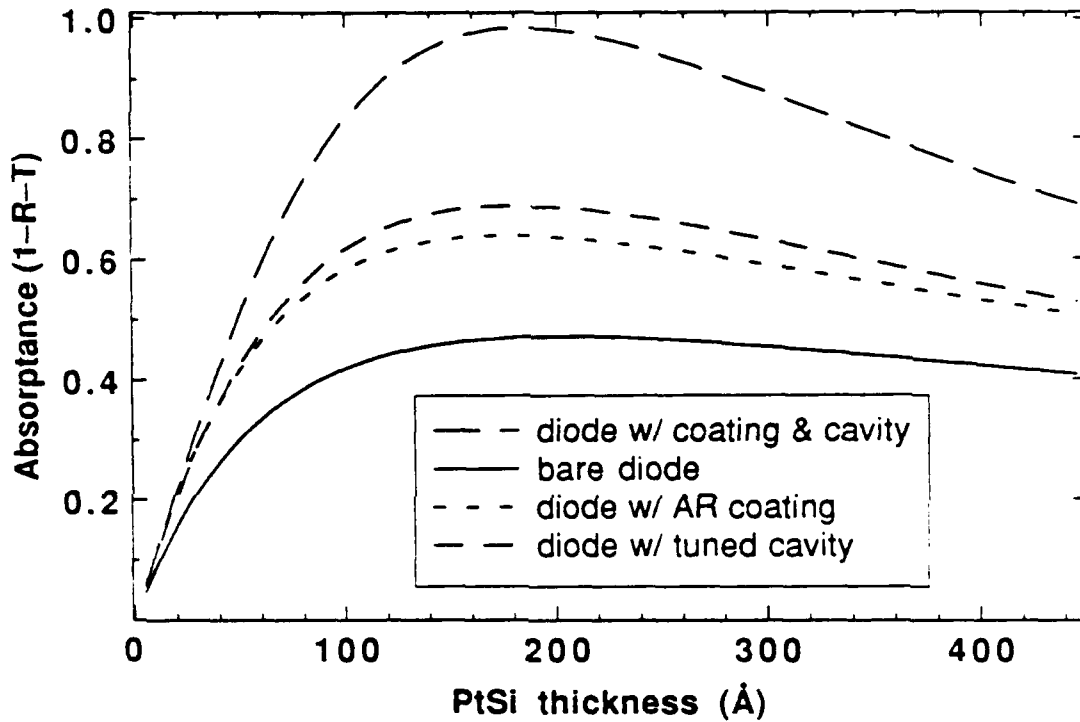


Fig. A.2. A comparison of the predicted optical absorption of back-illuminated PtSi/p-Si diodes with various combinations of absorption enhancing design features, plotted as a function of silicide thickness for radiation incident at a wavelength of $4\mu\text{m}$. All cavity structures are tuned for maximum absorption rather than maximum diode quantum efficiency.

Table A.1. The maximum absorption and corresponding PtSi thickness for each of the curves plotted in Fig. A.2.

Configuration	Maximum Absorption	Optimum PtSi Thickness
bare diode	47%	200Å
diode with AR coating	64%	175Å
diode with $1.24\mu\text{m}$ SiO_2 dielectric cavity	69%	180Å
diode with $1.25\mu\text{m}$ SiO_2 dielectric cavity and an AR coating	98%	185Å

complete absorption if a silicide approximately 185\AA thick is employed. Unfortunately, as Chapter 2 shows, the photoexcited carrier transport efficiency in films of this magnitude is extremely low; a deficiency which curbs the photoresponse performance below its optimum level even with the nearly perfect optical behavior. A significant improvement in transport efficiency can be realized only with very thin silicide films, which implies that high performance diodes will always operate well down on the linearly increasing section of the absorption curves rather than near the maxima. Given this fact, a cursory inspection of Fig. A.2 would indicate that, with the exception of the bare diode case, the particular design configuration matters little in the relevant thickness range. However, it should be noted that the two cavity structures featured in Fig. A.2 were tuned in order to obtain the maximum absorption possible at any PtSi thickness instead of the maximum overall quantum efficiency. These two objectives are incompatible with respect to cavity design. It is quite possible to select cavity widths that will increase the absorption for very thin films at the expense of lower overall peak values relative to those obtained from Fig. A.2. Fig. A.3 shows the change in the absorption curve of the fully configured device when the design emphasis shifts from absorption to photoresponse. A dramatic increase in absorption is apparent for film thicknesses below 80\AA as the focus changes. The peak falls from 98% to 84%, but the reduction is irrelevant as long as the hot carrier lifetime in the silicide layer cannot be increased by any substantial amount. Even with a properly designed cavity, however, the absorption at the optimal device design point will be less than 25% at $4\mu\text{m}$.

In addition to the design parameters that impact the absorption strongly, the variables which have little effect should also be mentioned. All of the absorption curves plotted above were generated under the assumption of normally incident radiation. Increasing the angle of incidence θ_{inc} on the back side of the detector through 30° produces only a slight increase in the predicted maximum quantum efficiency. In light of the difficulties oblique incidence presents when focal plane and imaging system constraints are considered, it

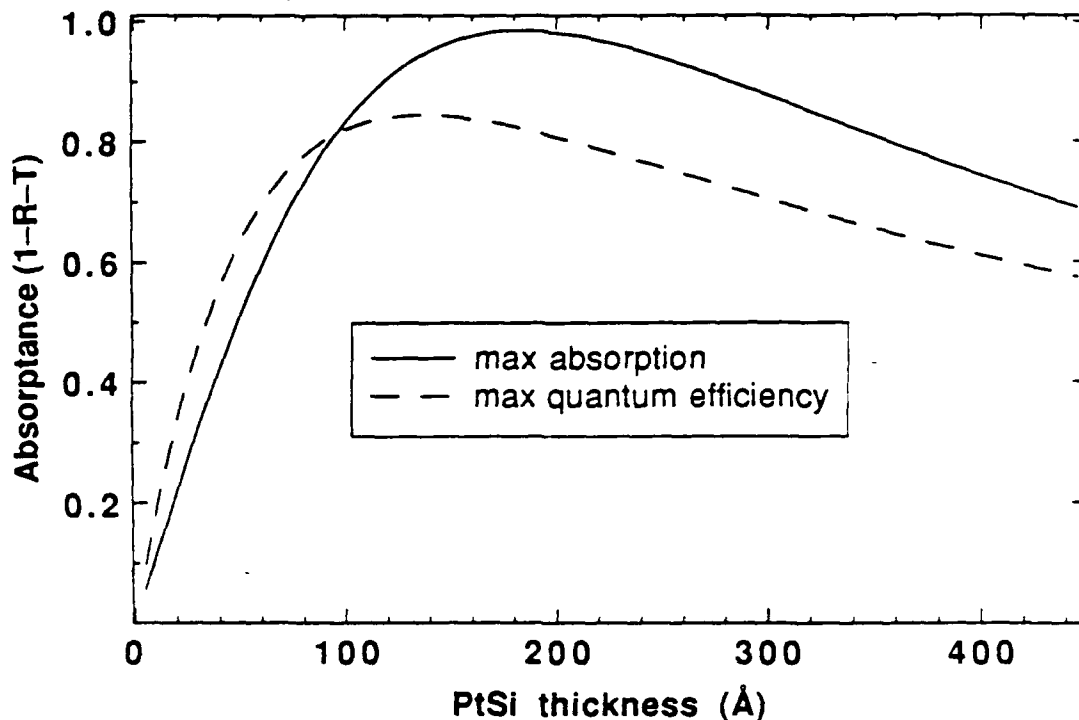


Fig. A.3. A comparison of the predicted absorption curves for two PtSi/*p*-Si photodiodes optimized for maximum optical absorption and maximum quantum efficiency, respectively, at 4 μ m. Both devices are assumed to possess anti-reflection coatings and resonant optical cavity structures. For maximum absorption, a cavity width of 12500 \AA is employed, while maximum photoresponse requires a width of 7900 \AA .

appears that no significant advantage would be gained by off normal illumination. The thickness of the aluminum mirror which caps the optical cavity is another fairly benign parameter. Unlike the PtSi and cavity dielectric layers, the mirror shows no resonance phenomena as its width increases from zero. Growth of the mirror layer up to about 500 \AA is accompanied by a gradual rise in cavity performance, but little or no variation is observed for mirror widths larger than this. All plots shown here were generated based on the assumption of a 1000 \AA aluminum layer. In addition, changes in the optical constants of the dielectric material indicate that the maximum yield is obtained when the index of refraction of the dielectric is minimized, although again the effect is minor for

common materials. The common choice of SiO₂ with $n \approx 1.4$ in the middle infrared wavelength region seems reasonable.

The outline of the radiation absorption calculation for common Schottky detector structures presented here represents the final link of the photoresponse modelling efforts discussed in Chapters 2 and 3. Absorption curves determined using this method indicate that anti-reflection coatings and properly constructed resonant cavities can produce considerable increases in the radiation coupling to PtSi/*p*-Si photodiodes. Unfortunately, full advantage cannot be taken of the improvements afforded by these design enhancements because of the limitations imposed by hot carrier transport deficiencies, and the maximum absorption level possible for a detector receiving radiation at a wavelength of 4 μm is only 20–25%. However, these features remain an important part of Schottky photodiode technology, and Chapter 6 suggests some ways in which the cavity concept might be further exploited.

References for Appendix A

1. H. Elabd, W.F. Kosonocky, "Theory and Measurements of Photoresponse for Thin film Pd₂Si and PtSi Infrared Schottky-Barrier Detectors with Optical Cavity," RCA Rev. 43, 569 (1982).
2. J.M. Mooney, Ph. D. thesis, University of Arizona, 1986.
3. J.M. Mooney, "Infrared Optical Absorption of Thin PtSi Films Between 1 and 6 μm ," J. Appl. Phys. 64, 4664 (1988).
4. E. Hecht, Optics, 2nd ed. (Addison-Wesley, Reading, Mass, 1987).
5. M. Born and E. Wolf, Principles of Optics (Pergamon, Oxford, 1970).
6. S. Ramo, J. R. Whinnery and T. Van Duzer, Fields and Waves in Communication Electronics, 2nd ed. (Wiley, New York, 1984).
7. E.D. Palik, Handbook of Optical Constants of Solids (Academic Press, Orlando, 1985).

DISTRIBUTION LIST

	COPIES
RL/ERED ATTN: P. Pellegrini Hanscom AFB MA 01731-5000	10
Stanford Electronics Laboratories Dept. of Electrical Engineering Stanford University Stamford, CA 94305-4055 Attn: D. E. Mercer	5
RL/DOVL Technical Library Griffiss AFB NY 13441-5700	1
Administrator Defense Technical Info Center DTIC-FDAC Cameron Station Building 5 Alexandria VA 22304-6145	2
Defense Advanced Research Projects Agency 1400 Wilson Blvd Arlington VA 22209-2308	2
Naval Warfare Assessment Center GIDEP Operations Center/Code 30G ATTN: E Richards Corona CA 91720	1
HQ AFSC/XTH Andrews AFB MD 20334-5000	1
ASD/ENEMS Wright-Patterson AFB OH 45433-6503	1

SM-ALC/MACEA
ATTN: Danny McClure
Bldg 237, MASOF
McClellan AFB CA 95652

1

AFIT/LDEE
Building 642, Area B
Wright-Patterson AFB OH 45433-6583

1

WRDC/MLPO
ATTN: D.L. Denison
WPAFB OH 45433-6533

1

WRDC/MTEL
Wright-Patterson AFB OH 45433

1

AUL/LSE
Bldg 1405
Maxwell AFB AL 36112-5564

1

HQ ATC/TT01
ATTN: Lt Col Killian
Randolph AFB TX 78150-5001

1

Commanding Officer
Naval Avionics Center
Library D/765
Indianapolis IN 46219-2189

1

Commanding Officer
Naval Ocean Systems Center
Technical Library
Code 96423
San Diego CA 92152-5000

1

Cmdr 1
Naval Weapons Center
Technical Library/C3431
China Lake CA 93555-6001

Superintendent 1
Code 524
Naval Postgraduate School
Monterey CA 93943-5000

CDR, U.S. Army Missile Command 2
Redstone Scientific Info Center
AMSMI-RD-CS-9/ILL Documents
Redstone Arsenal AL 35898-5241

Advisory Group on Electron Devices 2
201 Varick Street, Rm 1140
New York NY 10014

Los Alamos National Laboratory 1
Report Library
MS 5000
Los Alamos NM 87544

Commander, USAG 1
ASQH-PCA-CRL/Tech Lib
BLdg 01301
Ft Huachuca AZ 85613-5000

ESD/XRR 1
Hanscom AFB MA 01731-5000

ESD/SZME 1
Hanscom AFB MA 01731-5000

SEE JPC
ATTN: Major Charles J. Ryan
Carnegie Mellon University
Pittsburgh PA 15213-3390

Director NSA/CSS
TS122/TdL
ATTN: D W Marjarum
Fort Meade MD 20755-6000

1

NSA
ATTN: D. Alley
Div X911
9800 Savage Road
Ft Meade MD 20755-6000

1

Director
NSA/CSS R12
ATTN: Mr. Dennis Heinbuch
9300 Savage Road
Fort George G. Meade MD 20755-6000

1

DoD
R31
9800 Savage Road
Ft. Meade MD 20755-6000

1

DIRNSA
R509
9300 Savage Road
Ft Meade MD 20775

1

Director
NSA/CSS R1
ATTN: Mr. John C. Davis
9300 Savage Road
Fort George G. Meade MD 20755-6000

1

**MISSION
OF
ROME LABORATORY**

Rome Laboratory plans and executes an interdisciplinary program in research, development, test, and technology transition in support of Air Force Command, Control, Communications and Intelligence (C³I) activities for all Air Force platforms. It also executes selected acquisition programs in several areas of expertise. Technical and engineering support within areas of competence is provided to ESD Program Offices (POs) and other ESD elements to perform effective acquisition of C³I systems. In addition, Rome Laboratory's technology supports other AFSC Product Divisions, the Air Force user community, and other DOD and non-DOD agencies. Rome Laboratory maintains technical competence and research programs in areas including, but not limited to, communications, command and control, battle management, intelligence information processing, computational sciences and software producibility, wide area surveillance/sensors, signal processing, solid state sciences, photonics, electromagnetic technology, superconductivity, and electronic reliability/maintainability and testability.